Max-Planck-Institut für Metallforschung
Stuttgart

Investigation of intergranular glassy films in polycrystalline ceramics using Transmission Electron Microscopy

Somnath Bhattacharyya

Dissertation
an der
Universität Stuttgart

Bericht Nr. 186
März 2006

Investigation of intergranular glassy films in polycrystalline ceramics using Transmission Electron Microscopy

Von der Fakultät Chemie der Universität Stuttgart
Zur Erlangung der Würde eines Doktors der Naturwissenschaften
(Dr. rer. nat.) genehmigte Abhandung

vogelegt von

Somnath Bhattacharyya

aus Serampore in Indien

Hauptberichter:	Prof. Dr. Dr. Ing. h.c. M. Rühle
Mitberichter:	Prof. Dr. F. Aldinger
Tag der Einreichung:	02.01. 2006
Tag der mündlichen Prüfung:	09.03.2006

Max-Planck-Institüt für Metallforschung

Stuttgart 2006

dedicated to my beloved mother

Table of Contents

CHAPTER 1

Introduction

1.1 Remarks on intergranular glassy films

Understanding the structure and composition of interfaces is crucial for the design of ceramic materials. In ceramics like Si_3N_4, SiC, $SrTiO_3$, Al_2O_3 etc. amorphous films are often present at grain boundaries where the thickness depends on the composition of the amorphous phase. These films are characterized by a nearly constant thickness of about 1-2 nm. Being resistant to crystallization, these films are thought to represent equilibrium configurations. This special class of films (in equilibrium) is called “intergranular glassy films” (IGFs). As an example, a high-resolution image of an IGF in a Si_3N_4 ceramic recorded with a JEOL-4000FX 400kV transmission electron microscope (TEM) is shown in Fig. 1.1. Recently Subramaniam et al. [1] presented an overview on the occurance and stability of IGF. This paper may be an interesting introduction to this important field of research.

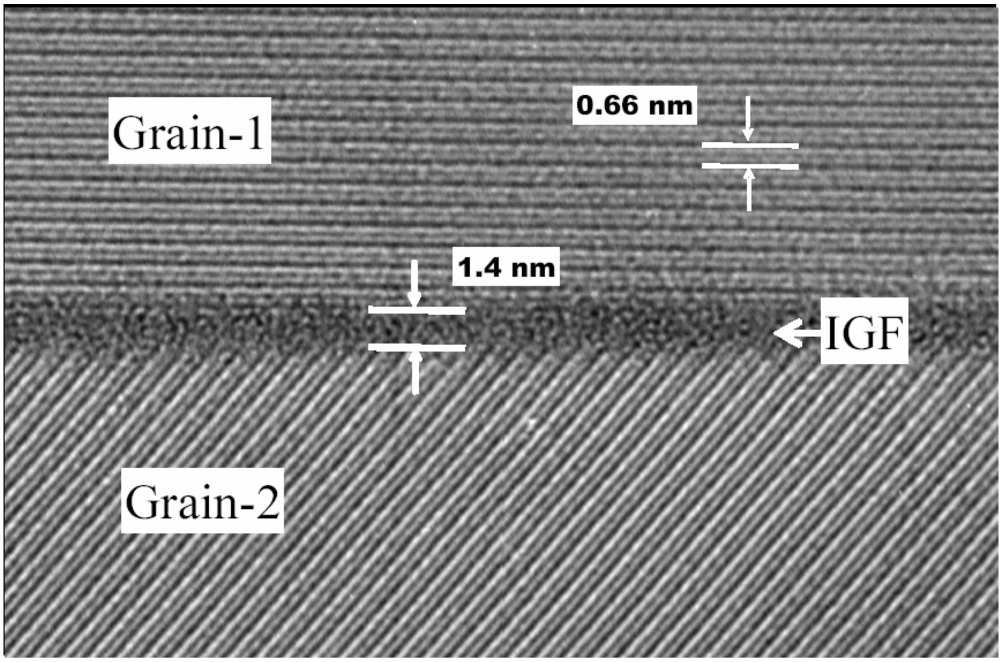

Fig. 1.1 An amorphous film, marked as IGF, lies between two crystalline grains Grain-1 and Grain-2.

Although most literatures focuses on IGFs in Si_3N_4 [2], ZnO [3,4] and SiC [5], they have also been observed at grain boundaries in other ceramics (e.g. $SrTiO_3$ [6], Al_2O_3 [7], , Mullite [8]), at metal – ceramic interfaces (e.g. Si_3N_4- Al [9], Al_2O_3-Ni [10]), at ceramic ceramic heterointerfaces in composite ceramics (e.g. ruthanate-silicate glass composites [11], Si_3N_4-SiC [12]) etc. The presence of IGF plays an important role in determining properties such as creep, fracture, oxidation, electrical behaviour etc. of the ceramic.

1.1.1 Formation of IGF

Conventionally IGFs are formed in system such as Si_3N_4 by liquid phase sintering which includes steps like cold pressing followed by sintering and finally hot isostatic pressing. Here the SiO_2 that forms during oxidation on Si surfaces prior to nitriding is mainly responsible for the formation of IGFs. IGFs can therefore be thought as the remaining liquid at the grain boundaries after the system is kinamatically frozen. This description is rather restrictive in understanding the formation of IGFs because they can also form by other processes such as solid state sintering like in (~ 0.6 mol %) Bi_2O_3 doped ZnO [13]. IGFs are also found between Si_3N_4 particles of flocculated clusters dispersed in a lanthanide–doped silicate glass matrix where they have thicknesses similar to those in densified polycrystalline ceramics [14]. IGFs of about 1.5 nm thickness were also observed between the crystallized amorphous SiO_2 layer and the single crystal TiO_2 substrate after depositing a thin SiO_2 film on a single crystal TiO_2 substrate and annealing it to form a eutectic liquid in equilibrium with the substrate and finally quenching [15].

1.1.2 Effect of various process parameters on IGF

1.1.2.1 Chemistry

The thickness of IGFs is strongly influenced by the dopant type used during sintering as well as the concentration of the dopant. Tanaka et al. [16] studied the thickness of an IGF in high purity Si_3N_4 ceramics systematically doped with Ca (from 0-450 at. ppm). The equilibrium thickness of the IGF possesses a specific value for undoped material. With increasing of Ca content, the film thickness decreases in the dilute region ($\leq$ 80 ppm Ca), followed an increase with further addition of CaO which was explained as a competition between the structural and electrical double layer repulsive forces and the attractive van der Walls dispersion force, as suggested by Clarke et al. [17]. In lanthanide doped Si_3N_4 ceramics, the ionic radius of the dopants influences IGF thickness [14]. The film thicknesses increase with increasing ionic radius of the Lanthenide.

1.1.2.2 Temperature

The formation and evolution of IGFs at high temperatures (at and below the sintering temperature), is of considerable importance towards an understanding of fundamental questions regarding IGFs; especially from the point of view of their applications. From in-situ transmission electron microscopy experiments, Clarke [18] concluded that changes of the IGF thickness do not occur below 1000º C which was supported by the results obtained by Cinibulk and Kleebe [19]. They performed a series of experiments in which disc shaped specimens of MgO doped Si_3N_4 specimens were heated between 1350º C to 1650º C for different durations of time followed by quenching in water. The steady increase of IGF thickness with temperature was explained as a change in equilibrium thickness of the film with temperature. However, further work is needed for complete understanding of the high temperature behaviour of IGF.

1.1.2.3 Oxidation

The oxidation experiment on two different Si_3N_4 samples (at 1400º C for 168 hour) by Cinibulk and Kleebe [20] showed that IGF thicknesses was reduced by about 20% from an initial value of about 1-1.2 nm. This was explained in terms of an inward diffusion of oxygen and an outward diffusion of cations.

1.1.2.4 Pressure

For Bi_2O_3-doped ZnO, Wang et al. [13] observed that the application of 1GPa pressure for 2 hours at 700º C desegregated the film material but annealing at ambient pressure (650º C, 24 hour) again restored the IGFs of 1-1.5 nm thickness.

1.1.2.5 Crystallization of glass in glassy pockets

The high temperature properties of Si_3N_4 can be improved by crystallization of glass in the glassy pockets [21]. However, crystallization of IGF is not expected because of its equilibrium configuration [22].

1.1.2.6 Creep

A bimodal width distribution was observed in IGFs of hot isostatically pressed Si_3N_4 (4 wt % Y_2O_3) after subjecting to tensile creep (1430º C, 40 MPa, 690 hour with a total strain of 0.65%) [23], This observation was explained as the effect of viscous flow of the IGF during creep. Similar results were also observed by Wang et al. [24] when Si_3N_4 (5 wt % Y_2O_3, 2 wt % MgO) was deformed superplastically.

1.1.3 Effect of IGF on various material parameters

1.1.3.1 Fracture toughness

To increase the fracture toughness of ceramic materials the fracture mode must be altered from transgranular to intergranular. So by controlling the composition and processing of the ceramic, IGFs of low intergranular strength can be produced to increase the fracture toughness of the material. Since too week IGFs can lead to overall decrease of the material strength, optimization is essential.

1.1.3.2 Creep

The creep behavior of the ceramic is most adversely affected by the presence of IGF since the glassy phase softens at high temperatures, leading to enhanced creep rates.

1.1.3.3 Oxidation resistance

IGFs have a pronounced effect on the oxidation resistance and high temperature mechanical strength of ceramics. For Si_3N_4 ceramics, these properties are strongly dependent on the type and amount of secondary phase solidifying at grain boundary and in pockets.Y_2O_3 as a sintering additive produces high oxidation resistance to Si_3N_4 [25].

1.1.4 Theoretical models for understanding IGF

Various theoretical models have been proposed so far to understand IGFs in a better way. Three of them are briefly described in the following.

1.1.4.1 Force balance model

An understanding of the equilibrium thickness configuration of IGFs was suggested by Clarke [26]. The model is based on the theory of colloids. According to this model, the stability of a continuous intergranular phase is considered in terms of the balance between the attractive capillarity and disjoining pressures. Amongst different components, a large structural component to the disjoining pressure, produced by distortion of the $Si\text{-}O_4$ tetrahedra, is responsible for the observed constancy of the thickness of IGF in polyphase Si_3N_4. The formation of IGFs was then explained using interfacial energy criteria. According to this explanation, low angle grain boundaries up to a certain threshold misorientation angle and special high angle boundaries of low interfacial energy (cusps in the gamma-plot) are free of intergranular films. The energy criterion needed for the formation of the IGFs may be written as $2\gamma_l \leq \gamma_b$ where γ_l is the glass-crystal interfacial energy and γ_b is the grain boundary energy. Further modification of this model including the contribution of the electrical double layer was proposed by the same author in 1987 [17].

1.1.4.2 Diffuse interface model

Cahn and Hillard [27] introduced a diffuse interface formulation to a multilayer system of liquid and solid phases. Later on, this formulation was used by Bobeth et al. [28] to develop a thermodynamic equilibrium model for a system of thin liquid phase and adjoining grains of solid phase where the liquid phase represents the IGF in polycrystalline ceramics. In this model, the crystal-IGF interface is, instead of being sharp, treated as being diffuse. According to this model, when the thickness of the liquid phase approaches the characteristic length (i.e. interface width), its composition can deviate markedly from the bulk liquid phase composition. In absence of any stabilizing interactions, such as repulsive structural and electrostatic forces, there exists a driving force for thinning of the film as well as for dissolving it in the presence of a reservoir. Therefore, to keep an equilibrium thickness of IGF, additional stabilizing forces must exist between the bounding grains.

1.1.4.3 Adsorption / Segregation / wetting approach

The wisdom gained from the research of segregation and wetting has also been used to understand IGF in a different way [29,30, 31, 32]. Segregation at interface can increase from a sub-monolayer to multilayer coverage which ends up with complete wetting of the grain boundary. Therefore, IGF can be classified as graded multilayer absorbates where ‘graded’ indicates the diffuseness of the crystal-IGF interface. An important goal of this model is to predict the structure of grain boundary as a function of the temperature and activity of the absobtate species. From a wetting point of view, an IGF can also be identified as a partially wetting or prewetting film.

1.2 Use of transmission electron microscopy techniques in IGF study

Various transmission electron microscopic techniques have been used to study the structure and chemistry of IGF for almost three decades. Fig. 1.2 shows the basic configuration of a transmission electron microscope (TEM) including the ray diagrams for imaging and diffraction mode [33]. The electrons are being produced by either a tungsten, a LaB_6, a Shottky field emission gun or a cold field emission gun. An important point to keep in mind is that the tip of the electron source should be as sharp as possible, ideally a single atom, to achieve maximum special coherence. The condenser lens system controls the beam divergence angle α, which is ideally zero for the imaging mode, but in practice some beam divergence is needed to keep the beam current reasonably high i.e. maintain a reasonable brightness of the image.

The image or diffraction pattern is recorded on either film, imaging plates (IP) or a CCD camera. Film has low dynamic range (about 8 bit) and is comparatively difficult to process. IPs are digital films with the highest dynamic range among these three mediums, since they record information on a logarithmic scale. They are directly quantifiable and reusable but similarly inconvenient for processing as films. They are ideal for diffraction work. CCD cameras, with a dynamic range of normally 12-16 bit, record image on a linear scale. As the images recorded by CCD can be transferred directly to the computer, they can be processed or stored immediately [33].

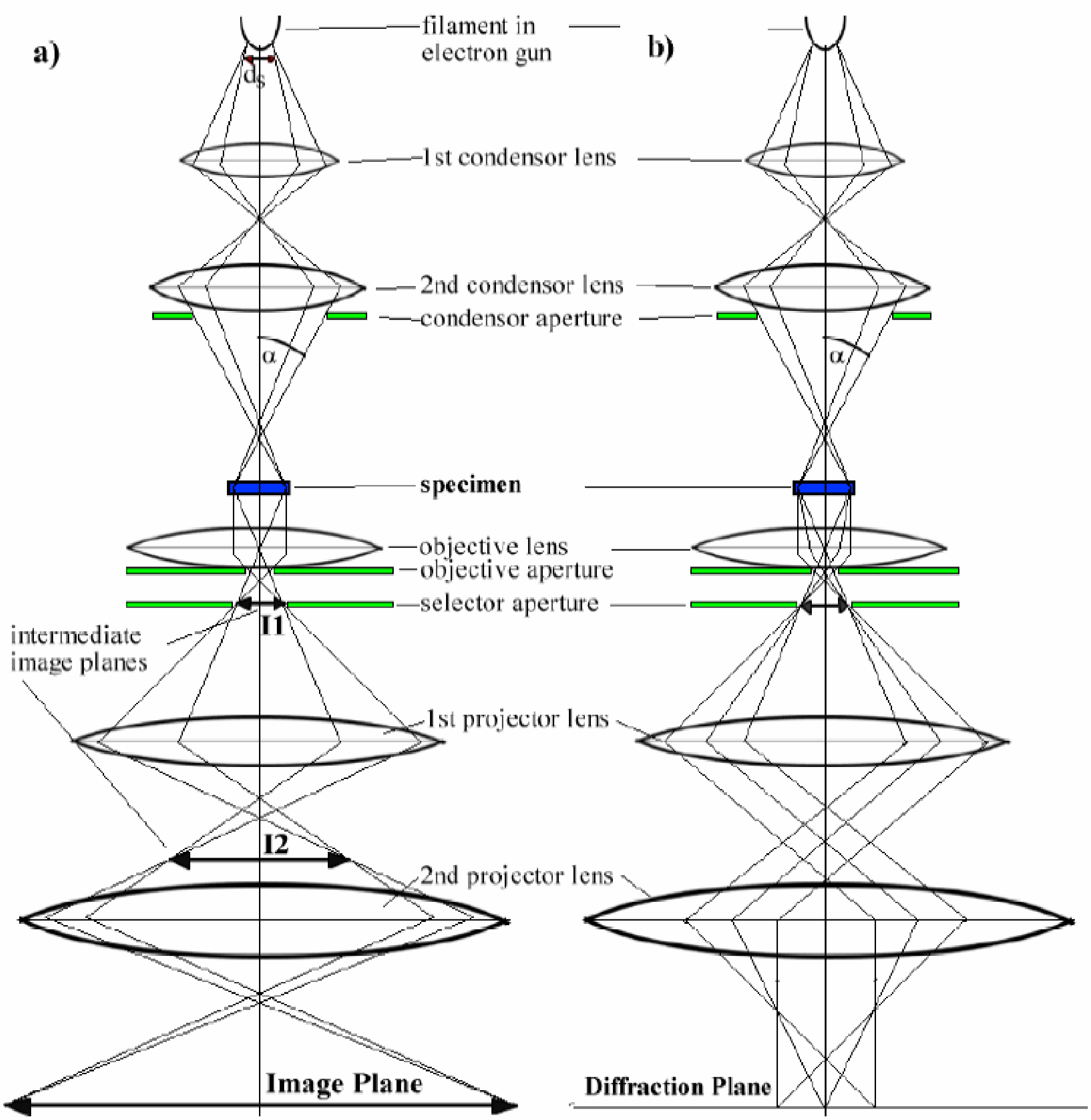

Fig 1.2 Ray diagram of a basic electron microscope (a) Ray diagram for microscope operating in imaging mode and (b) operating in diffraction mode. α is the convergent semiangle of the incident electron beam and d_s is the source size (Figure taken from [33])

Images are either formed using the central spot , or some or all of the scattered electrons. The way the electrons are chosen to form the images is to insert an objective aperture into the back focal plane of the objective lens, thus blocking out most of the diffraction pattern except that which is visible through the aperture. If the direct beam is selected, as shown in Fig. 1.3 (a), the resultant image is called a bright-field (BF) image. If any other form of scattered electrons is chosen. the resultant image is called as dark-field (DF) image as shown in Fig. 1.3 (b).

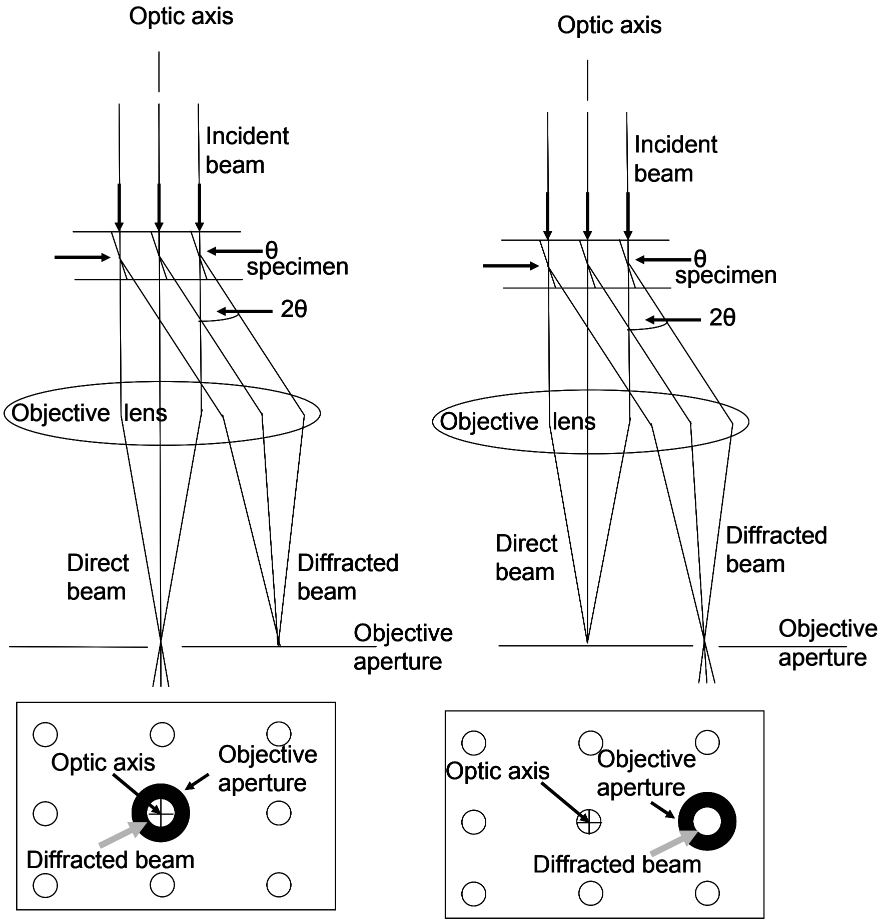

Fig. 1.3 Ray diagrams showing how the objective lens aperture are used in combination to produce (a) a BF image formed from the direct beam, (b) a displaced aperture DF image formed with a specific off-axis scattered beam

Using high-resolution lattice fringe imaging (will be described in section 1.2.1.3), the presence of IGFs (in hot pressed MgO fluxed Si_3N_4 ceramics) was first reported by Clarke and Thomas [34]. With the advancement of the technology of microscopes, IGFs have been studied from different perspectives to reveal more information about their structure and chemistry. In the following subsections, the various transmission electron microscopic techniques which have been used so far to study IGF will be briefly outlined.

1.2.1 Techniques to determine the thickness of IGF

Apart from the recent work by Maclaren [35] (deccribed in section 1.2.1.4), the three main imaging techniques, proposed by Clarke [36] and compared quantitatively by Cinibulk et al. [37], have been used so far by different researchers to determine the thickness of IGFs. The techniques are as follows:

1.2.1.1 Diffuse dark field (DDF) imaging

Due to its experimental ease, DDF imaging is perhaps the most widely used method for detecting the amorphous phase in polycrystalline specimen. How this technique works is illustrated schematically in Fig. 1.4.

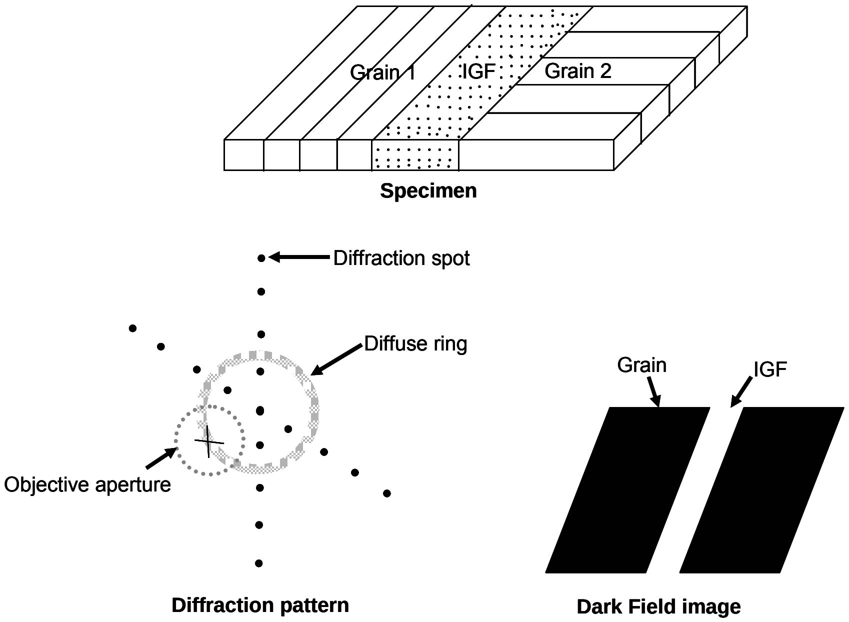

Fig 1.4 Schematic illustrates diffused dark field imaging technique for IGF

Electrons scattered diffusely by the intergranular amorphous phase produce a weak diffuse ring around the central spot in the diffraction pattern. A portion of this ring is selected by the smallest objective aperture and centered to the optical axis of the microscope while eliminating the contribution of Bragg – diffracted electrons. The IGF is then imaged directly in bright contrast relative to the adjacent grains. According to Krivanak et al. [38] microdensometry can be used to measure the thickness of IGFs by comparing the relative intensity of diffusely scattered electrons from the interface and from the triple pocket. Alternatively, by digitizing the DDF and evaluating the intensity of a line scan across the interface [37], the thickness can also be measured. The IGF thickness measured using DDF technique shows 50-100 % larger values than obtained by high-resolution lattice fringe imaging [37]. Though this is the simplest method to detect the amorphous phase but quantitative measurement of IGF thickness is not possible.

1.2.1.2 Fresnel fringe imaging

Presence of an intergranular glassy phase at the grain boundary produces a discontinuity of the mean inner potential across the interface which, in turn produces shift in the phase of the exit face wave. This phase shift produces fringes when imaging out of focus due to interference of scattered electrons coming from different parts of the specimen, as illustrated schematically in Fig. 1.5.

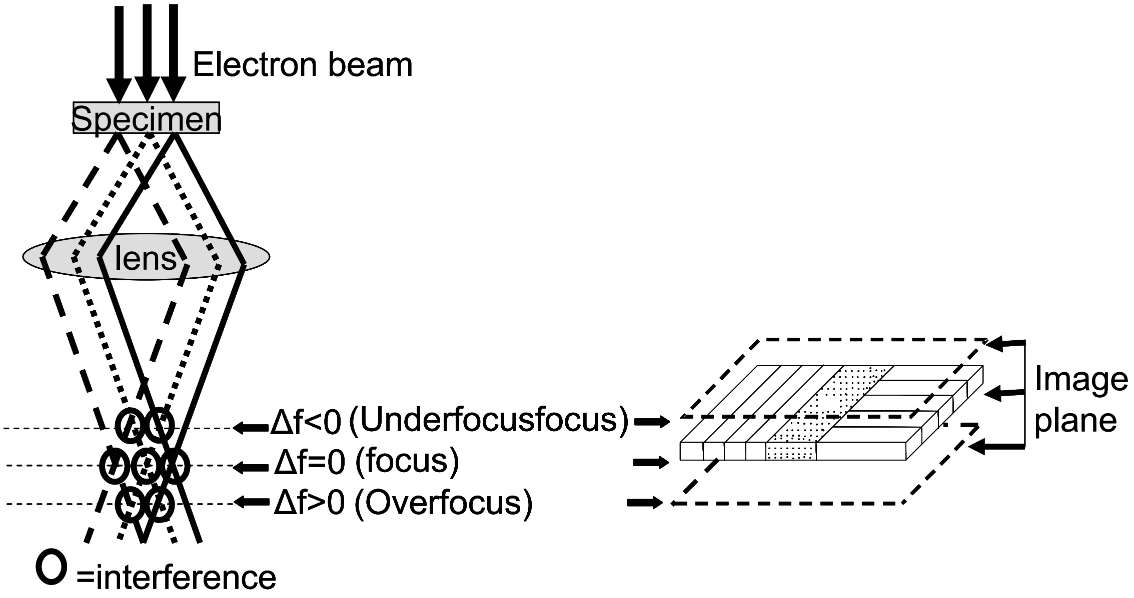

Fig. 1.5 Schematic to show the interference caused by moving out of focus

For this technique, the specimen within the microscope should be tilted in a way to orient the boundary of interest parallel to the electron beam (called ‘edge on’ condition). Further tilt is necessary, keeping the grain boundary ‘edge on’ to orient both the bounding grains in weak diffracting condition [39]. The objective aperture should be placed around the central spot in the diffraction pattern. To increase contrast it would be better to place an objective aperture which excludes all other diffraction spots. A fringe at an overfocus is basically the contrast reversal of the fringe at exactly the same underfocus value [40]. The thickness of the IGF has been measured by extrapolating the Fresnel fringe spacings of out of focus images to Gaussian focus [36] though the thickness measured using this technique shows 20-35 % larger values than obtained by high-resolution lattice fringe imaging [37].

1.2.1.3 High-resolution lattice fringe imaging

In their pioneer work, Clarke and Thomas [34] used high-resolution lattice fringe imaging to detect IGFs. To perform it, the grain boundary should be edge on while the bounding grains should be in good diffracting conditions to visualize the lattice fringes clearly on either side of the IGF [37]. For this purpose an objective aperture can be used that allows diffracted beams to contribute to the imaging process [41]. The width of the measured discontinuity in the fringes across the interface is the thickness of the IGF as shown in Fig. 1. When the crystal structure is known, the spacing of the lattice fringes can be used as an internal reference to determine the IGF thickness quantitatively. To avoid delocalization of fringes, images should be taken close to Gauss defocus [37]. The stringent geometrical and electron optical requirements for this technique limit its application to only the very thin region of the specimen. The main source of error in measuring the film thickness directly from high resolution electron micrographs (HREM) is the uncertainty involved in defining the edge on condition. This is specially difficult for the grains where the lattice fringes are not parallel to the interface and/or where a slight change in contrast at the grain edges is seen due to thickness variation along the electron beam or chemical segregation [42].

1.2.1.4 Fourier filtering of high-resolution micrographs (FF-HREM*)*

Recently, MacLaren [35] proposed a different technique to measure the thickness of IGF from HREM. The principle of this method is to use Fourier filtering technique to remove the periodic information of the adjacent grains i.e. it significantly enhances the visibility of all non-periodic information, particularly that from amorphous intergranular phase. For this technique, first the high-resolution lattice fringe imaging technique must be performed. Now the HREM are Fourier transformed. After blanking out the spots belonging to crystalline reflections using circular masks, an inverse Fourier transformation is necessary to produce an image that contains contrast only from the amorphous phases. The apparent film thickness shows a discrepancy between measurement from the original HREM and from the filtered image. The author's explanation is that the fringe delocalization and diffuseness of the IGF / grain interfaces lead to a significant underestimate of the thickness in unprocessed HREM. According to the author, if the film width is measured to the mid point of the decay of the amorphous contrast at either edge of the IGF and not to the outer edges, it should give a more accurate value of the average film width, even if the width displays some local variations.

1.2.2 Determination of composition of IGF

1.2.2.1 EDXS and EELS

Energy Dispersive X-ray Spectroscopy (EDXS) and Electron Energy Loss Spectroscopy (EELS) are the two most important tools for the study of composition of the IGF [43]. Distribution of the elements across IGF and triple pocket has been determined using EELS [44] as well as by EDXS [45]. EELS using Energy Loss Near Edge Structure (ELNES) has been used to quantify grain boundaries on a sub-nanometer scale. Gu et al. [46] introduced a method called "spatial difference". This method represents a systematic procedure to subtract completely the signal of the bulk from the grain boundary using the knowledge of the ELNES for the reference system i.e. the grains. According to the observation made by Gu et al.[47], the structural width of an IGF (measured using high-resolution lattice fringe imaging) of Si_3N_4 has a good agreement with its chemical width (the extent of the distribution of chemical species of IGF into the adjacent crystal) as measured using a method based on ELNES. Recently a new approach, to separate the spatially resolved EELS signal of solely IGF from that of the bounding grains, named 'spectrum separation' has been introduced by Gu [48].

1.2.2.2 Z contrast imaging

This technique is based on the fact that high-angle elastic scattering is predominantly caused by the Rutherford elastic scattering where the cross section is roughly proportional to the square of the atomic number of the scattering element. Therefore, elements with a high atomic number (Z) scatter stronger at equivalent high angles. These scattered electrons can be collected by a high angle annular detector. To avoid Bragg effects, these detectors gather electron scattering of semiangles greater than 50 mrad (~ 3º) [49]. Images formed in this way are called Z contrast images or high angle annular dark field (HAADF) images.

An advantage of these images is that the contrast is generally unaffected by small changes of the objective lens defocus and spectrum thickness [49]. This technique has been used recently by different authors to image the segregation of rare earth elements to the IGF / grain interface of rare earth doped Si_3N_4 ceramics [50,51,52]. An alternative method, for determining the segregation of atoms to specific sites at the IGF with respect to one of the adjacent grains using Fourier transformation of the electron diffraction pattern (from the region containing an IGF), has recently been proposed by Koch [53].

1.2.3 Potential profile across IGF

1.2.3.1 Diffraction

In order to avoid blurring effects due to lens aberrations in the formation of images, a new method for solving the phase problem has been developed by Koch et al. [54]. In this method, the projected potential profile across an IGF is reconstructed from a small angular range tomographic series of one dimensional zero-loss energy filtered diffraction patterns assuming kinemetic scattering conditions. The advantage of using a tilt series is to determine the exact film orientation with respect to the grain lattices, specimen surface as well as the absolute specimen orientation with respect to the laboratory frame reference.

1.2.3.2 Off axis holography

In electron holography [55], interference between the scattered electron waves from the object and a reference wave through vacuum produces fringe patterns which represent the subtle changes in phase and amplitude of the scattered waves. To allow this coherent interaction the microscope should be equipped with a biprism. This method has been used by Elfwing and Olsson [56] to determine the phase information of active interfaces in

ZnO varistor material to reveal several aspects of the double Schottky barrier, including the barrier height and the charge depletion region width.

1.2.4 Determination of local atomic structure of IGF

McBride and Cockayne [57] introduced a method where the reduced density function (RDF) has been derived from diffraction patterns using a convergent probe focused on a nano-volume of material. The RDF provides information about the nearest neighbor distances and coordination.

1.2.5 Goal of the thesis:

The main aim of all the TEM studies referred above is to characterize structure and chemistry of IGFs which will provide complete control over the design of the material containing IGFs. Though the combined effort of all the previous researchers pushed the understanding of IGFs well ahead, still plenty of questions are needed to be solved such as:

- What is the temperature dependency of the equilibrium thickness of an IGF?
- What is the orientation dependency of the equilibrium thickness of an IGF?
- What is the exact structure and chemistry of the glass / crystal interface?
- To characterize IGF 3-dimensionally, how can existing characterization methods be improved?

Depending on all these questions the final goal is to describe IGFs (independent of system) as a function of temperature, activity of the chemical species, crystallography etc. and to predict the formation of IGFs in new systems. The aim of the present PhD work is to apply a variety of conventional as well as newly developed TEM techniques to characterize these films, driving the understanding of IGFs forward. This is a cumulative thesis where four papers are presented subsequently in four chapters.

The theme of **chapter 2** is the use of Fresnel fringes and Fourier filtering for the measurement of the thickness of IGFs. Using image simulations, various kinds of deviation from an ideal square-well potential profile and their effects on the Fresnel image contrast are considered. A method to objectively analyze fringe spacing from IGFs by Fourier filtering the Fresnel contrast images (FCIs) is also presented. Difficulties in using the standard Fresnel extrapolation technique are outlined and an alternative to measure IGF thickness based on zero-defocus (in-focus) FCI is suggested. This work is intended to be a practical toolkit for measuring the width of IGFs by taking experimental difficulties into account and comparing different techniques.

Ceramics like Si_3N_4 are used for high temperature applications, so it is important to examine the effect that temperature has on IGFs in this material. **Chapter 3** deals with in-situ heating experiments of Si_3N_4 ceramics within different microscopes while taking care to separate beam irradiation from temperature effects. Major discrepancies were observed between the results obtained in the present investigation with that reported in the previous literature. Possible mechanisms and sources of artifacts in the observed data are discussed. This work shows that certain material transport processes may be active at rather low temperatures in Si_3N_4.

An iterative method for reconstructing the exit face wave function from a through focal series of TEM image line profiles across an interface is presented in **chapter 4**. Apart from high-resolution images recorded with small changes in defocus this method works also well for a large defocus range as used for Fresnel imaging. Using the phase-object approximation the projected electrostatic as well as the absorptive potential profiles across an interface are determined from this exit face wave function. A new experimental image alignment procedure was developed in order to align images with large relative defocus shift. The performance of this procedure is shown to be superior to other image alignment procedures existing in the literature. The reconstruction method is applied to both the simulated and the experimental images.

The method described in **chapter 4** was finally applied to obtain the projected electrostatic as well as absorptive potential profiles, scaled with respect to vacuum, across intergranular glassy films (IGFs) and interfaces between grains and glassy pockets in silicon nitride ceramics in **chapter 5**. The potential profiles across the grain / glassy pocket interface and the adjacent IGF were observed to be very similar and give very strong evidence for the existence of a space charge layer at the interface.

The following four chapters represent four papers which have been submitted independently as the open literatures are in the following:

Chapter 2:
Title : Aspects regarding measurement of thickness of Intergranular Glassy Films
Authors: S. Bhattacharyya, A. Subramaniam, C. T. Koch and M. Rühle
Journal of Microscopy, accepted

Chapter 3:
Title : The evolution of amorphous grain boundaries during In-situ heating experiments in Lu-Mg doped Si_3N_4
Authors: S. Bhattacharyya, A. Subramaniam, C. T. Koch, R. M. Cannon and M. Rühle
Materials Science and Engineering : A, accepted

Chapter 4:
Title: Projected potential profiles across interfaces obtained by reconstructing the exit face wave function from through focal series
Authors: S. Bhattacharyya, C. T. Koch and M. Rühle
Ultramicroscopy, submitted

Chapter 5:
Title: Projected potential profiles across intergranular glassy films
Authors: S. Bhattacharyya, C. T. Koch and M. Rühle
Journal of the American Ceramic Society, submitted

Therefore, each chapter is an independent unit. The results of these works are summarized in English in **chapter 6** and in Deutsch in **chapter 7**.

1.3 References

[1] A. Subramaniam, C.T. Koch, R.M. Cannon, M. Rühle, Mat. Sc. & Engg. A, accepted.

[2] H.-J. Kleebe, J. Ceram. Soc. Jpn. 105 (1997) 453.

[3] W.G. Morris, J. Am. Ceram. Soc. 56 (1973) 360.

[4] D.R. Clarke, J. Appl. Phys. 49 (1978) 2407.

[5] H.-J. Kleebe, J. Eur. Ceram. Soc. 10 (1992) 151.

[6] X. Pan, H. Gu, S. Stemmer, M. Rühle, Mater. Sci. Forum, 207-209 (1996) 421.

[7] R. Brydson, S.-C. Chen, F. L. Riley, S. J. Milne, X. Pan, M. Rühle, J. Am. Ceram. Soc. 81 (1998) 369.

[8] S. Kanzaki, T. Kumazawa, J. Asaumi, O. Abe, H. Tabata, J. Ceram. Soc. Jpn. 93 (1985) 407.

[9] H.G. Jeong, K. Hiraga, M. Mabuchi, K. Higashi, Philos. Mag. Lett. 74 (1996) 73.

[10] A. Avishai, C. Scheu, W.D. Kaplan, Z. Metallkd. 94 (2003) 272.

[11] Y.M. Chiang, L.A. Silverman, R.H. French, R.M. Cannon, J. Am. Ceram. Soc. 77 (1994) 1143.

[12] K. Daschowdhury, R.W. Carpenter, W. Braue, Ultramicroscopy 40 (1992) 229.

[13] H. Wang, Y.M. Chiang, J. Am. Ceram. Soc. 81 (1998) 89.

---

[14] C.M. Wang, X. Pan, M.J. Hoffmann, R.M. Cannon, M. Rühle, J. Am. Ceram. Soc. 79 (1996) 788.

[15] H.D. Ackler, Y.M. Chiang, J. Am. Ceram. Soc. 80 (1997) 1893.

[16] I. Tanaka, H.-J. Kleebe, M.K. Cinibulk, J. Bruley, D.R. Clarke, M. Rühle, J. Am. Ceram. Soc. 77 (1994) 911.

[17] D. R. Clarke, T. M. Shaw, A. Philipse, R. G. Horn, J. Am. Ceram. Soc. 76 (1994) 1201.

[18] D.R. Clarke, J. Am. Ceram. Soc. 72 (1989) 1604.

[19] M.K. Cinibulk, H.-J. Kleebe, A. P. Tomsia, A. Glaeser (Eds.), Plenum Press, New York, (1998) 123.

[20] M.K. Cinibulk, H.-J. Kleebe, J. Mater. Sci, 28 (1993) 5775.

[21] A. Tsuge, K. Nishida, M. Komatsu, J. Am. Ceram. Soc. 58 (1975) 323.

[22] J.S. Vetrano, H.-J. Kleebe, E. Hampp, M.J. Hoffmann, M. Rühle, R.M. Cannon, J. Mater. Sci. 28 (1993) 3529.

[23] Q. Jin, D.S. Wilkinson, G.C. Weatherly, W.E. Luecke, S.M. Wiederhorn, J. Am. Ceram. Soc. 84 (2001) 1296.

[24] C.M. Wang, M. Mitomo, T. Nishimura, Y. Bando, J. Am. Ceram. Soc. 80 (1997) 1213.

[25] F. Castro, J. Echeberria, M. Fuentes, J. Mat. Sc. Lett. 11 (1992) 101.

[26] D. R. Clarke, J. Am. Ceram. Soc. 70 (1987) 15.

[27] J.W. Cahn, J.E. Hilliard, J. Chem. Phys. 28 (1958) 258.

[28] M. Bobeth, D. R. Clarke, W. Pompe, J. Am. Ceram. Soc. 82 (1999) 1537–46.

[29] I. Tanaka, J. Ceram. Soc. Jpn. 109 (2001) S127.

[30] R. M. Cannon, L. Esposito, Z. Metallkd. 90 (1999) 1002.

[31] R.M. Cannon, Structure-composition-stability relations in ceramic interfaces, talk at Max Planck Institute, Stuttgart (2004).

[32] R.M. Cannon, M. Rühle, M.J. Hoffmann, R.H. French, H. Gu, A.P. Tomsia, E. Saiz, Mat. Sci. & Eng. A, accepted.

[33] C.T. Koch, Determination of Core structure Periodicity and Point Defect Density Along Dislocations, PhD thesis, Arizona State University, (2002).

[34] D. R. Clake, G. Thomas, J. Am. Ceram. Soc. 60 (1977) 491.

[35] I. MacLaren, Ultramicroscopy 99 (2004) 103.

[36] D.R. Clarke, Ultramicroscopy 4 (1979) 33.

[37] M.K. Cinibulk, H.-J. Kleebe, M. Rühle, J. Am. Ceram. Soc. 76 (1993) 426.

[38] O. L. Krivanek, T.M. Shaw, G. Thomas, J. Appl. Phys. 50 [6] (1979) 4223.

[39] W.M. Stobbs, F.M. Ross, Evaluation of advanced semiconductor materials by electron microscopy, NATO ASI Series B, Vol. 203, D. Cherns (Ed.), Plenum press, London (1989) 183.

---

[40] J.N. Ness, W.M. Stobbs, T.F. Page, Phil. Mag. A 54 (1986) 679.

[41] D.R. Clarke, J. Am. Ceram. Soc., 62 (1979) 236.

[42] H.-J Kleebe, J. Am. Ceram.Soc. 105 [6] (1997) 453.

[43] D.B. Williams, A.D. Romig, Ultramicroscopy 30 (1989) 38.

[44] H. Gu, X. Pan, R.M. Cannon, M. Rühle, J. Am. Ceram. Soc. 81 (1998) 3125.

[45] M. Chi, H. Gu, P. Qian, X. Wang, P. Wang, Z. Metallkd. 96 (2005) 486.

[46] H. Gu, Miran, S. Stemmer, H. Müllejans, M. Rühle, Ultramicroscopy 59 (1995) 215.

[47] H. Gu, R.M. Cannon, M. Rühle, J. Mater. Res., 13 [2] (1998) 376.

[48] H. Gu, Mater. Trans. JIM, 45 [7] (2004) 2091.

[49] D.B. Williams, C.B. Carter, Transmission Electron Microscopy, Plenum Press, New York, (1996) 358.

[50] N. Shibata, S.J. Pennycook, T.R. Gosnell, G.S. Painter, W.A. Shelton, P.F. Becher, Nature 428 (2004) 730.

[51] A. Ziegler, J.C. Idrobo, M.K. Cinibulk, C. Kisielowski, N.D. Browning, R.O. Ritchie, Science 306 (2004) 1768.

[52] G.B. Winkelman, C. Dwyer, T.S. Hudson, D. Nguyen-Manh, M. Döblinger, R.L. Satet, M.J. Hoffmann, D.J.H. Cockayne, Philos. Mag. Lett., 84 [12] (2004) 755.

---

[53] C. T. Koch, Imaging grain boundary segregation by electron diffractive imaging, Z. Metallkd., 96 [6] (2005) 443.

[54] C.T. Koch, S. Bhattacharyya, M. Rühle, R.L. Satet, M. Hoffmann, Microsc. microanal., in press.

[55] Y.G. Wang and V.P. Dravid, Philos. Mag. Lett., 82 [8] (2002) 425.

[56] M. Elfwing, E. Olsson, J. App. Phys., 92 (2002) 5272.

[57] W. McBride, D.J.H. Cockayne, J. Non-Cryst. Solids, 318 (2003) 233.

CHAPTER 2

Aspects regarding measurement of thickness of Intergranular Glassy Films

S. Bhattacharyya, A. Subramaniam, C. T. Koch and M. Rühle

Journal of Microscopy, acepted

Abstract

Materials like Si_3N_4, SiC and $SrTiO_3$ can have grain boundaries (GB) characterized by the presence of a thin intergranular amorphous film of nearly constant thickness, in some cases (e.g. Si_3N_4) almost independent of the orientation of the bounding grains, but dependent on the composition of the ceramic. Microscopy techniques such as high-resolution lattice fringe imaging, Fresnel fringe imaging and diffuse dark field imaging have been applied to the study of intergranular glassy films (IGFs). The theme of the current investigation is on the use of Fresnel fringes and Fourier filtering for the measurement of the thickness of IGFs. Fresnel fringes hidden in high-resolution micrographs (HRM) can be used to objectively demarcate the glass-crystal interface and to measure the thickness of IGFs. Image line profiles obtained from Fourier filtering the high-resolution micrographs can yield better estimates of the thickness. Using image simulation, various kinds of deviation from an ideal square-well potential profile and their effects on the Fresnel image contrast are considered. A method is also put forth to objectively retrieve Fresnel fringe spacing data by Fourier filtering Fresnel contrast images (FCIs). Difficulties arising in the use of the standard Fresnel fringe extrapolation technique are outlined and an alternate method for the measurement of thickness of IGFs, based on zero-defocus (in-focus) FCI is suggested. The experimental work is from two ceramic systems: Lu-Mg doped Si_3N_4 and $SrTiO_3$ (stoichiometric and non-stoichiometric). Further, a comparison is made between the standard high resolution lattice fringe technique, the standard Fresnel fringe extrapolation technique and the methods of analyses introduced in the current work, to bring out their utility and merits. Taking experimental difficulties into account, this work is intended to be a practical toolkit for the study of IGFs.

2.1 Introduction

Intensive research in the last few decades have given us considerable insight into the structure of interfaces in materials like Si_3N_4 and SiC, having an equilibrium thickness intergranular glassy film (IGF) [1,2]. Various electron microscopic techniques have been applied to the study of IGFs and these investigations have yielded important information regarding the structure of these films and their interface with the bounding grains. These techniques include, high-resolution electron microscopy [3], Fresnel fringe imaging [4], diffuse dark field imaging [3], energy filtered electron diffraction [5], high-angle annular dark field scanning transmission electron microscopy (HAADF-STEM) [6,7] and holography [8]. A comparative analysis of these techniques has been carried out at various times and the works of Simpson et al [9], Cinibulk et al [3], MacLaren [10] and Kleebe [1] are noteworthy. High resolution lattice fringe imaging has been cited as the most reliable technique for the reproducible measurement of the thickness of IGFs [3].

In the Fresnel fringe imaging technique, the thickness of the IGF can be obtained by extrapolation of the fringe spacing data [11,12]. Ness et al. [13], Rasmussen and Carter [14], Ross and Stobbs [15], Dunin-Borkowski [16] and Loudon et al. [17] have used Fresnel through focal series data to obtain the potential profile across grain boundaries (GBs). Further, holographic methods, such as off-axis- [8,18], or in-line holography [19] retrieve the exit face wave function and yield the projected potential profile across GBs.

Earlier models [20,21] and recent work [6,22] have shown that the interface between the IGF and the bounding crystal is not abrupt but diffuse. This is also reflected in the high-resolution micrographs (HRMs) [23]. This poses important questions as to how a given technique can be optimally used for the measurement of the thickness of an IGF and how meaningful comparisons with results from other techniques can be made.

In the study of IGFs by high-resolution microscopy, often there are constraints imposed either by the material or by the microscope. In some materials (e.g. stoichiometric $SrTiO_3$), the frequency of GBs with an IGF is very small. In samples with large grain-size (~tens of microns), only very few interfaces may be observed within the thin region of the sample, making this problem even more severe and hence maximum use of GBs with an IGF should be made for measurements. In $SrTiO_3$ samples (used for this study) the grain boundaries were usually not planar and only a portion of the GB could be aligned approximately edge-on. This implies that tilt along an axis perpendicular to the GB (i.e., keeping the boundary edge-on) is severely limited. Microscope imposed constraints are mainly related to resolution and available tilt angles. For $SrTiO_3$, only five planes fall into the resolution range of a standard microscope like JEOL 4000EX [(001), (101), (111), (002) and (102)]. In this microscope, with a top entry holder, tilt available is ±10º and sharp lattice fringe contrast sometimes could not be obtained on both sides of the IGF within this tilt regime.

The Fresnel fringe extrapolation technique, in spite of its utility, suffers from its own set of non-idealities imposed by microscope or material. Various sources of noise add up to the uncertainty in the measurements, especially at low defocus values [24]. Lower accelerating voltage microscopes (e.g., Zeiss-912, 120kV) are preferred for certain investigations, wherein electron beam induced knock-on damage needs to be minimized. Due to an in-column energy filter (used to stop the inelastically scattered electrons), the Zeiss-912 has the advantage that it gives excellent Fresnel Contrast Images (FCIs), but the region of defocus values giving interpretable Fresnel contrast is limited (~1-3 μm). As the source of Fresnel contrast is the difference in potential across the interface, a small potential difference can lead to poor contrast. While differences in the projected potential of grain and IGF may be intrinsic local material properties, it needs to keep in mind that the projected potential is also affected by surface grooving due to preferential etching of either material during specimen preparation. In the standard Fresnel imaging technique, a square potential well is assumed across the GB. Under these assumptions, the Fresnel intensity profile for a given value of underfocus, is related to the profile for the corresponding overfocus by a mirror inversion with respect to zero defocus [13]. This perfect symmetry has been found to be absent in real boundaries with an IGF and hence the analyses needs to be modified. Additionally, for diffuse interfaces, the contrast decreases rapidly as the defocus value approaches zero [14]. This implies that best use of the available images is required to avoid large errors possibly being introduced in the usual method of extrapolation of the data.

In the present work, the following tasks are attempted:

(i) Measuring the thickness of an IGF objectively from Fresnel fringes hidden in high-resolution micrographs and also enhancing the utility of HRMs with weak lattice fringe contrast.

(ii) Fourier filtering (FF) Fresnel images for contrast enhancement and for (a) measuring the thickness of IGFs and (b) finding the zero-defocus (in-focus) condition.

(iii) Addressing issues related to calculation of thickness of an IGF using the Fresnel fringe spacing extrapolation technique (simulation & experiments).

(iv) Understanding the different kinds of deviation from an ideal square-well potential in terms of their effect on the Fresnel contrast profiles (by simulation).

(v) Measuring the thickness of IGFs from a zero-defocus FCI (noting that the contrast observed at zero-defocus is not the classical Fresnel contrast).

The methodologies developed will be tested on experimental images of Lu-Mg doped Si_3N_4 (henceforth referred to as the 'Si_3N_4 sample') and $SrTiO_3$ (stoichiometric and non-stoichiometric $SrTiO_3$) samples. Si_3N_4 and $SrTiO_3$ represent vastly different cases, when it comes to processing routes, grain-size, frequency of occurrence of IGFs, faceting of the grains and 'straightness' of the GB.

A comparison of the thickness obtained by the different methods will be made. Emphasis will be on the optimum use of recorded data, which reflect the real experimental conditions.

2.2 Experimental details

Dense silicon nitride samples have been prepared from milled and sieved α-Si_3N_4 (88.07 wt%), SiO_2 (2.16 wt%), MgO (1.07 wt%) and Lu_2O_3 (8.7 wt%) powders, by first cold pressing, then sintering at 1750°C for 15 min at a pressure of 10 bar and finally hot isostatic pressing at 1750°C for 60 min at 100 bar [25]

$SrTiO_3$ samples were prepared by mixing $SrCO_3$ and TiO_2 in two compositions: (i) stoichiometric (TiO_2 / $SrCO_3$ = 1/1) and (ii) non-stoichiometric, TiO_2 rich (TiO_2 / $SrCO_3$ = 1/0.98) and calcined in two stages (Calcination 1:18 hrs, 975°C; Calcination 2:15 hrs, 1050°C). The heating rate during calcination was 20°C / min and the cooling rate was 10°C / min. The powders were sintered in the following steps: (i) heating in air at 1340°C for 6 hrs, (ii) hot isostatically pressed at 1300°C and 2×10^7 Pa in Argon atmosphere, (iii) heated at 1480°C for 3 hrs in air to reach higher density. The stoichiometric composition is designated as STO1 and the non-stoichiometric composition as STO2. The Si_3N_4 and $SrTiO_3$ samples were provided by Dr. Raphaelle Satet and Prof. Michael Hoffmann of the University of Karlsruhe.

Specimens for transmission electron microscopy were prepared by the standard techniques of grinding, dimpling and ion-beam thinning (Precision Ion Polishing System, Gatan Inc.).

The ion-beam thinning was carried out at an angle of inclination of 8° of the ion beam to the sample. The Si_3N_4 specimens were coated with a thin layer of carbon to minimize charging under the electron beam.

Three transmission electron microscopes (TEMs) were used for microscopy. These are: (i) JEOL 4000 FX, (ii) JEOL JEM 4000 EX & (iii) Zeiss-912. The JEOL 4000 FX (point to point resolution 0.2 nm), operated at 400 kV was used for examining the Lu_2O_3-MgO doped Si_3N_4 specimen. Images were taken on Kodak electron image film (SO-163) at a magnification of 500000X. JEOL JEM 4000 EX (operated at 400 kV), dedicated to high resolution performance (point to point resolution 0.18 nm), was used for examining the $SrTiO_3$ samples. In this microscope, the magnification and films (for recording images) are identical to those in the JEOL 4000 FX machine. The Zeiss-912 microscope (LaB_6, Köhler illumination) operated at 120 kV and equipped with an in-column energy filter was also used for examining the Lu_2O_3-MgO doped Si_3N_4 specimen. Experiments at Zeiss-912 were done using an electron beam convergence semi-angle (θ_c) of 1.0 mrad.

In the Zeiss-912 microscope energy-filtered images were obtained using a 15 eV energy window centered on the zero loss peak. The images were captured onto a 1024×1024 pixel CCD array at a sampling density relative to the specimen of 0.19 nm per pixel (images were taken at a magnification of 80000X). A series of images (through focal series) were acquired in the defocus range of 1 μm to 2.2 μm with a step size of 0.2 μm in both over and under focus conditions. Additionally, images at and close to zero-defocus were also obtained.

For these experiments, boundaries of interest were tilted to orient them parallel to the incident electron beam (edge-on condition). For lattice and Fresnel fringe imaging, the specimen was further tilted, keeping the grain boundary parallel to the electron beam, using procedures described by Cinibulk et al. [3] and Stobbs and Ross [26] respectively.

The standard method of Clarke [27] was used to measure the thickness from high-resolution micrographs (using lattice fringe imaging) in addition to the methods developed in the current work. The Fresnel fringe techniques developed in the present investigation were compared with the standard Fresnel fringe extrapolation method [27,3,12]. In the conventional Fresnel extrapolation method for measuring the thickness of IGFs, fringe spacing values (s) have been plotted as a function of defocus (Δf) [12]. Jin et al. [12] had used the following equation relating fringe spacing (s) to IGF thickness (s_0) and defocus (Δf):

$$s = s_0 + c\Delta f^{1/2} \tag{1}$$

Where, 'c' is a microscope dependent constant. This formula implies a linear plot of 's' versus $\sqrt{\Delta f}$ and extrapolation to zero-defocus would give the thickness of the IGF.

Digital micrograph software (Gatan Inc., Pleasanton, CA, USA) was used to obtain line profiles across the interface from each of the digitized images (integrated over suitable widths; usually of 100 pixels) and also for the Fourier filtering the experimental images. MATLAB-R12 software was used to implement the algorithms used in the simulations.

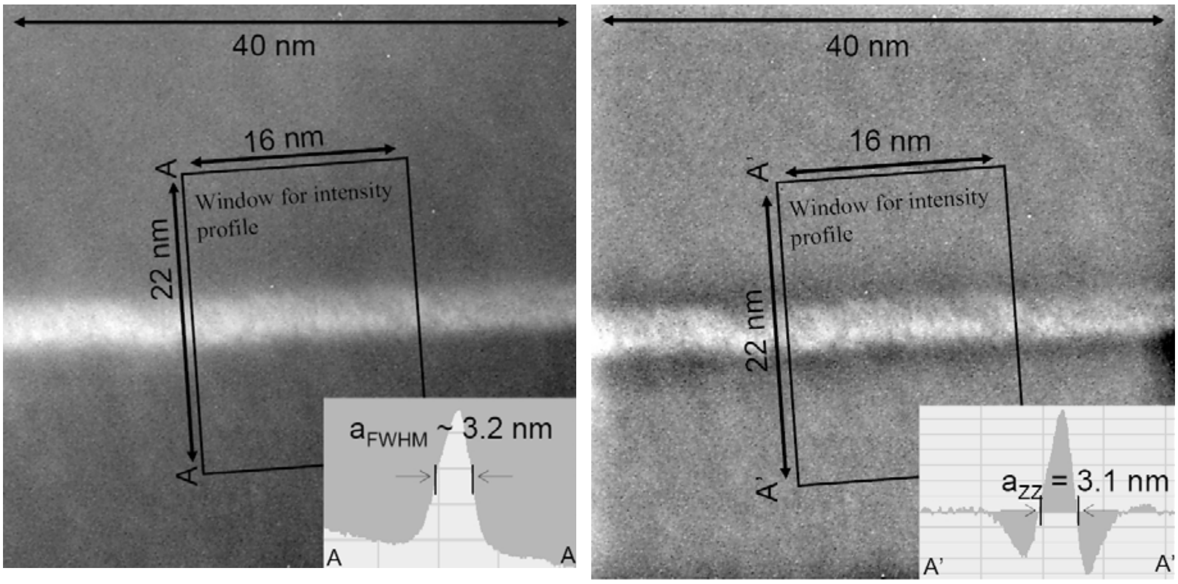

Fig. 2.1 Illustration of the difficulty in measuring widths from images with diffuse interface contrast: (a) diffuse dark field image from a grain boundary in the stoichiometric $SrTiO_3$ sample (STO1), with the plot of the profile across the image (AA) as inset, (b) Fourier filtered image using a mask of 0.073 nm^{-1} diameter with the profile across A'A' as inset.

2.3 Fourier filtering

To illustrate the utility of the Fourier filtering method we consider an image with a diffuse contrast across the grain boundary with an IGF (Fig. 2.1a). The figure shows the diffuse dark field image taken from the stoichiometric $SrTiO_3$ sample and the intensity profile across the interface (inset). Measurement of the thickness from such an image could prove to be quite subjective, which makes comparison with other results difficult. Fig. 2.1b shows the corresponding Fourier filtered image, obtained by masking the central spot in the Fourier transformation (FT), with a mask size of 0.073 nm^{-1} (the unmasked region is used for the inverse Fourier transformation (IFT)). This is equivalent to subtracting a low-resolution (resolution = 13.7 nm) image from the original. The enhancement in contrast and ease of measurement of the thickness is seen from the Figure. The use of this method for the case of the Fresnel Contrast Image (FCI) is described next. In this work, the acronym FCI is also used for simulated Fresnel contrast profiles.

The choice of the size of the Fourier mask is an important parameter in the procedure and how that has been chosen in the current investigation is described in the following. Too small a mask will not be useful as we are keeping only the unmasked region. Too large a mask will lead to mask induced artifacts in the IFT. As a first approximation, the mask should be smaller than the streak produced by the IGF in the FT of the image. To simulate the effect of the mask, the scattering potential across the IGF is chosen as in Fig.2.2a. The various parameters and assumptions used in the simulations performed in the current work are listed in Table 2.1. The profile (P) has two Gaussian functions (replacing the vertical sections of a square potential well) to describe the diffuseness of the crystal-glass interface. The depth of the potential profile is chosen as that between Si_3N_4 (17.4 V) and SiO_2 (10.9 V) [28,29]. Fig. 2.2b shows the FT of the profile in Fig. 2.2a along with the superimposed mask (Fig 2b: the shaded region is excluded in the IFT). Fig. 2.2c shows the IFT after the application of the mask. The size of the mask (of 0.026 $Å^{-1}$) is chosen in a way to produce low contrast in the flat region of the profile (i.e. in the 'a' section in Fig. 2.2a). A good correspondence in the values measured, is seen from the figure. Table 2.2 summarizes the data from Fig. 2.2 along with the measurements obtained for a mask of 0.032 $Å^{-1}$ size. Due to the long tail of the Gaussian function (Fig. 2.2a), the value a_0 is measured at 99% intensity of the profile. Secondary oscillations which can be seen in the zoomed out version of Fig. 2.2c, are due to the sharp nature of the mask interface and the presence of secondary minima in the FT of the profile P (Fig. 2.2b).

The scattering potential profile shown in Fig. 2.2a is a one-dimensional (1D) projected potential profile. It should be understood, that this profile cannot distinguish between the various structural cases illustrated in Fig. 2.3. All the three profiles shown in Fig. 2.3 would be captured in a 1D profile as having a diffuse interface.

Parameter	Designation	Value / Description
Weak Phase Object Approximation	WPOA	$\sigma . t = 0.01\ V^{-1}$ (σ – interaction constant, t – specimen thickness)
Phase Object Approximation	POA	$\sigma . t = 0.1\ V^{-1}$
Potential Profile	P	FWHM = 20.4 Å, Diffuse interface on both sides
	P1	$a = a_0 = a_{FWHM}$ = 20.4 Å, square potential well
	P2	a_{FWHM} = 20.4 Å, left-right (LR) asymmetric profile
	P3	a_{FWHM} (of well) = 20.4 Å, a_{FWHM} (of bump) = 4.5 Å to simulate segregation
Wavelength (λ)	L1	0.0335 Å
Spherical aberration (Cs)	C1	2.7 mm
Accelerating voltage	-	120 kV
Objective aperture Size	A0	Diffuse aperture with d_{FWHM} =0.2496 $Å^{-1}$
Mask Size	M1	0.026 $Å^{-1}$ (diameter)
	M2	0.032 $Å^{-1}$ (diameter)
	M3	Mask with diffuse edges d_{FWHM} = 0.026 $Å^{-1}$
Beam sampling size	-	0.23 Å
Simulation cell size	-	126.73 Å

Table 2.1 Parameters and assumptions used in the current simulations of FCI and FF-FCI.

Mask size ($Å^{-1}$)	From the profile (nm)			From the Fourier Filtered Profile (nm)		
	a_0	a_{FWHM}	a	a_{PP}	a_{ZZ}	a'
0.026 (M1)	3.24	2.08	1.1	3.19	2.09	1.1
0.032 (M2)	”	”	”	3.10	1.97	1.16

Table 2.2 A comparison of the spacings measured from a simulated Fourier filtered profile, using a mask of two sizes, with that from the original profile. The variables are defined in Fig. 2.2.

The effect of Fourier filtering on the plot of a Fresnel contrast profile is shown in Fig. 2.4 (the simulation of Fresnel contrast will be dealt with in the next section). Fig. 2.4a shows the

Fresnel intensity profile calculated from the scattering potential profile considered in Fig. 2.2a, at a defocus value of +2.2 μm. Application of the Fourier mask (as in Fig. 2.2c) leads to the Fourier filtered Fresnel intensity profile as in Fig. 2.4b. A good correspondence is seen in the spacings measured from the Fourier filtered profile with the original profile. The values measured are marked in the figure. However, if we start with a zero-defocus FCI (Fig. 2.4c) and apply the Fourier mask, then the width (FWHM) of the projected potential well can be directly measured from the FF-FCI (Fig. 2.4d,e). Fig. 2.4d shows the Fourier filtered plot obtained from the complex exit face wave function and Fig. 2.4e shows the FF-FCI obtained from the absolute value of the exit face wave function. Fig. 2.4e is expected to correspond to the experimental profile (experimental intensity, $I = |\Psi|^2 = (\text{absolute value})^2$).

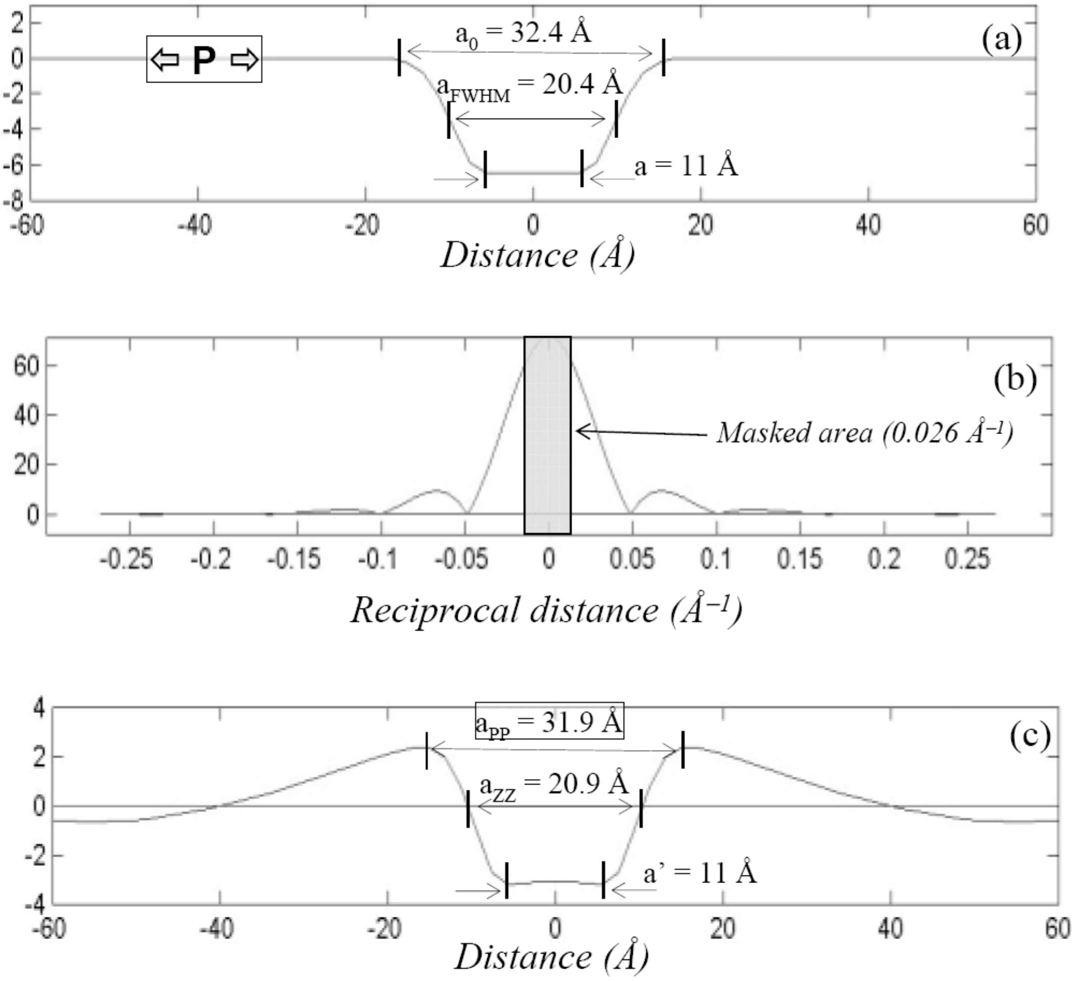

Fig. 2.2 Effect of Fourier filtering on a diffuse scattering potential profile: (a) the scattering potential, (b) FT of the profile with a superimposed mask (the shaded region is excluded in the IFT), (c) the IFT after application of the mask. The various distances (a, a_0, a_{FWHM}, a', a_{ZZ}, a_{PP}) are defined in the figures for further use.

Secondary oscillations seen in Fig. 2.4b are expected to be less prominent in the case of a diffuse mask which would reduce secondary oscillations. For at least somewhat diffuse interfaces this implies a monotonic dependence of the mask size on the spacings measured from the Fourier filtered profile. Hence, the technique is expected to be reasonably robust with respect to mask size, for measurements from real Fresnel contrast images. An additional point regarding the use of Fourier masking will be made in the next section.

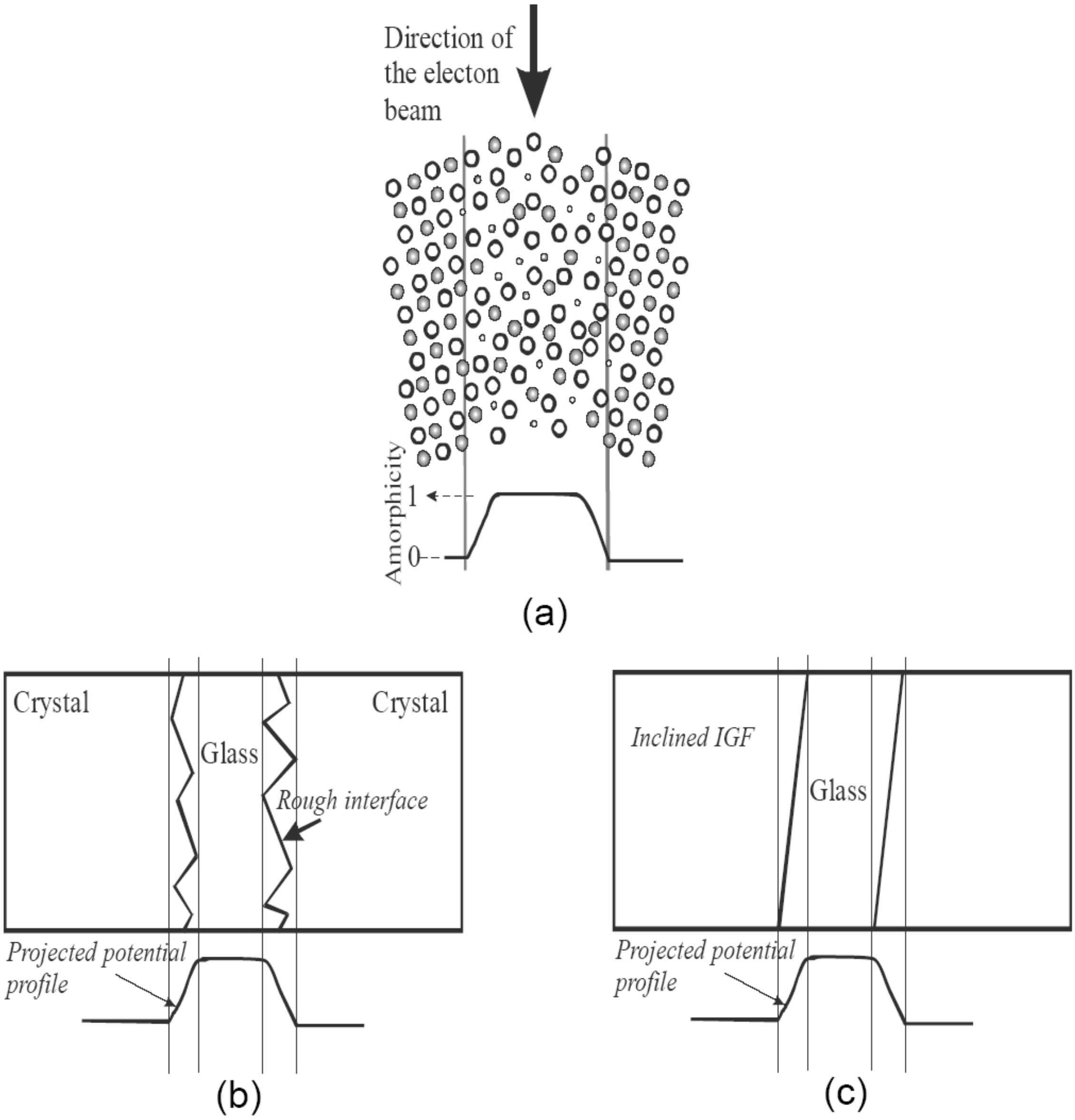

Fig. 2.3 Schematic illustration of the limitations of a one-dimensional projected potential profile, with respect to its ability to distinguish between various structural features in the GB region having an IGF: (a) diffuse interface between glass and crystal, (b) rough interface, (c) inclined interface. All the three structures show a similar potential profile, as shown below each of the figures.

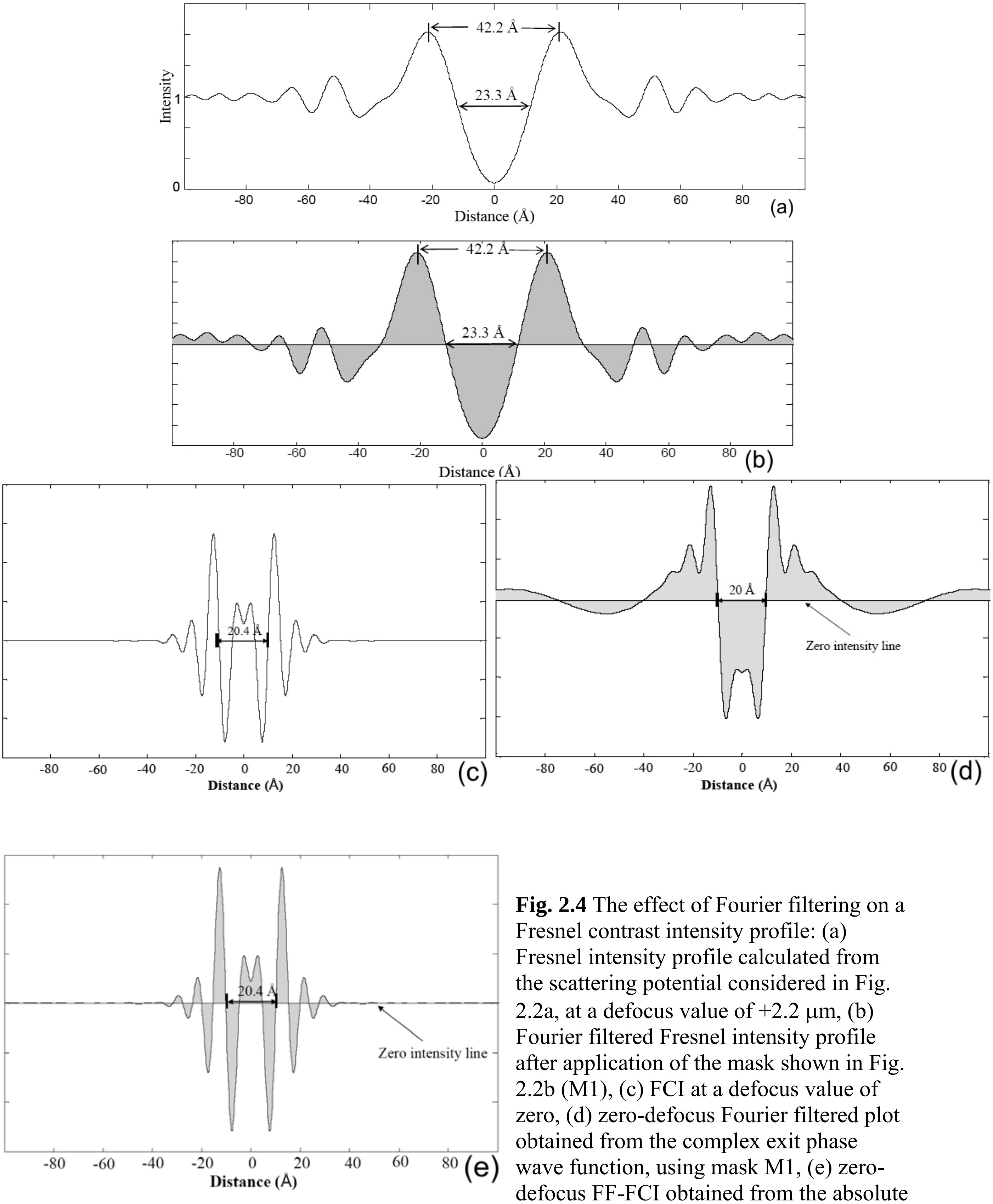

Fig. 2.4 The effect of Fourier filtering on a Fresnel contrast intensity profile: (a) Fresnel intensity profile calculated from the scattering potential considered in Fig. 2.2a, at a defocus value of +2.2 μm, (b) Fourier filtered Fresnel intensity profile after application of the mask shown in Fig. 2.2b (M1), (c) FCI at a defocus value of zero, (d) zero-defocus Fourier filtered plot obtained from the complex exit phase wave function, using mask M1, (e) zero-defocus FF-FCI obtained from the absolute value of the exit phase wave function. The simulation parameters are: WPOA, C1, L1, A0 & M1 (defined in Table 2.1).

2.4 Potential profiles and Fresnel contrast

Using the phase-object approximation (POA), the following equation [30] is used to simulate Fresnel profiles from one-dimensional potential profiles:

$$I_{(r)} = \left| FT^{-1}[FT(e^{-i\sigma V_{(r)} t}) f_{ap}(k) e^{i\chi(k)}] \right|^2 \tag{2}$$

where, $I_{(r)}$ is the image intensity, $i=\sqrt{-1}$, $V_{(r)}$ is the potential profile across the interface, σ is the interaction constant, t is the specimen thickness, $f_{ap}(k)$ is the objective aperture function in reciprocal space, $e^{i\chi(k)}$ is the microscope contrast transfer function (MTF) and FT^{-1} denotes the inverse Fourier transform operation. Neglecting aberrations other than defocus and spherical aberration, $\chi(k)$ is given by $\chi(k) = \pi \Delta f \lambda k^2 + \frac{1}{2} \pi C_s \lambda^3 k^4$, where k is the reciprocal space coordinate. The values of the parameters used in the simulation are listed in Table 2.1.

Fig. 2.5a shows the square well potential profile usually used as the potential profile across the IGF for the calculation of the Fresnel contrast (see also Section 2.2). The simulated Fresnel intensity profiles at various defocus values are shown in Fig. 2.5b-h. The Fresnel profiles corresponding to a defocus of ±2.2 μm, as presented in Fig. 2.5h (a schematic version of this figure is shown as Fig.1 in Ness et al. [13]), show two features: (i) Left-right mirror symmetry (LR symmetry), (ii) inversion symmetry across the x-axis between overfocus and underfocus profiles (OU symmetry).

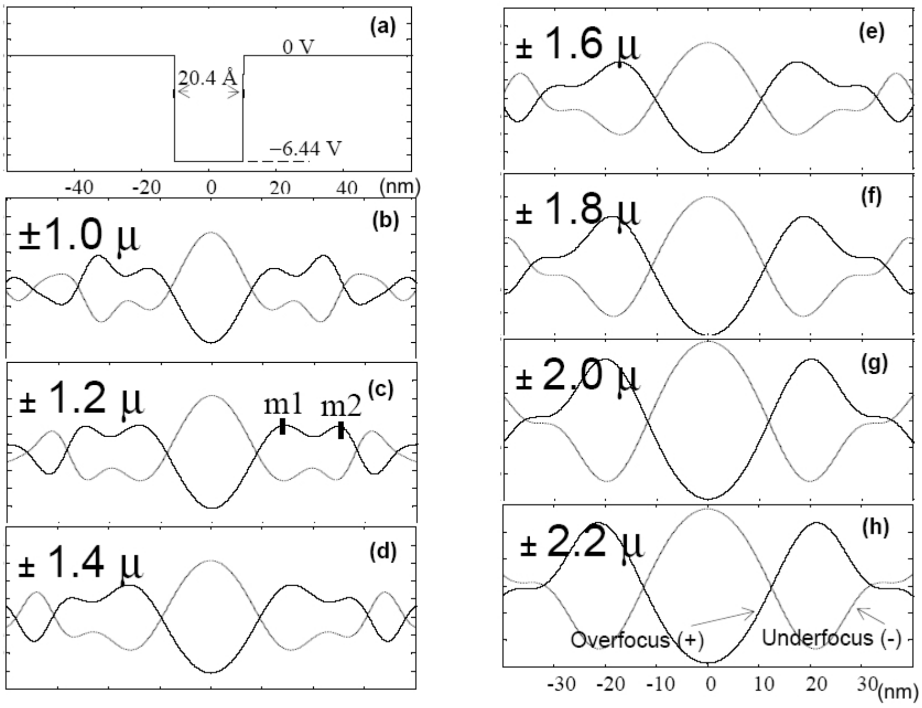

Fig. 2.5 (a) A square potential well, (b-h) simulated Fresnel contrast plots for various over and underfocus conditions. The simulation parameters are: WPOA, C1, L1 & A0.

Fig. 2.6a and Fig. 2.6b show experimental Fresnel contrast images (FCIs) of the Si_3N_4 sample taken by the Zeiss-912 microscope at a defocus of +1.2 μm and -1.2 μm respectively. Fig. 2.6c and Fig. 2.6d show the corresponding intensity profiles across the IGF integrated over a width of 18.8 nm along the interface. Fig. 2.7a and b were obtained by filtering out the central spot from the Fourier transformation of Fig. 2.6a and b respectively using mask M3. Fig. 2.7c,d show the intensity profiles across Fig. 2.7a and b respectively. The various distances measured (PP, FWHM, ZZ & VV) are also defined in Fig. 2.6 and Fig. 2.7. The following points can be observed from the figures:

(i) in overfocus condition (Fig. 2.6c) the background intensity level from the grains on either side of the GB is different but the peak intensities (P) are seen to be equal (Fig. 2.7c),

(ii) in underfocus condition (Fig. 2.6b) the intensity of the valleys are not equal for an identical value of defocus (Fig. 2.6d),

(iii) peak to peak distance (PP) measured from Fig. 2.6c (+1.2 μm, overfocus) is not equal to the valley to valley distance (VV) measured from Fig. 2.6d (-1.2 μm, underfocus).

Hence, it is seen that LR and OU symmetries are broken in the experimental Fresnel contrast images. This symmetry breaking may happen due to the shape of the potential profile across the IGF or due to the effect of specimen thickness along the direction of the electron beam. To understand the effect of various potential profiles and specimen thickness along the electron beam, different cases are considered, as listed in Table 2.3. The profile P3 is chosen to reflect segregation of a dopant with scattering potential higher than the grains adjacent to the IGF. Parameters used in the simulation are listed in Table 2.1. The important points which can be seen from the table are:

(i) Under the weak-phase-object approximation (WPOA) i.e. for very thin specimen, LR symmetry and approximate OU symmetry are present (for profile P1)

(ii) In the Fresnel profiles generated using the phase-object approximation (POA), the OU symmetry is broken (P1)

(iii) LR asymmetry in the potential profile leads to a LR asymmetry in the Fresnel profiles (profile P2 & P3), however, approximate OU symmetry is maintained

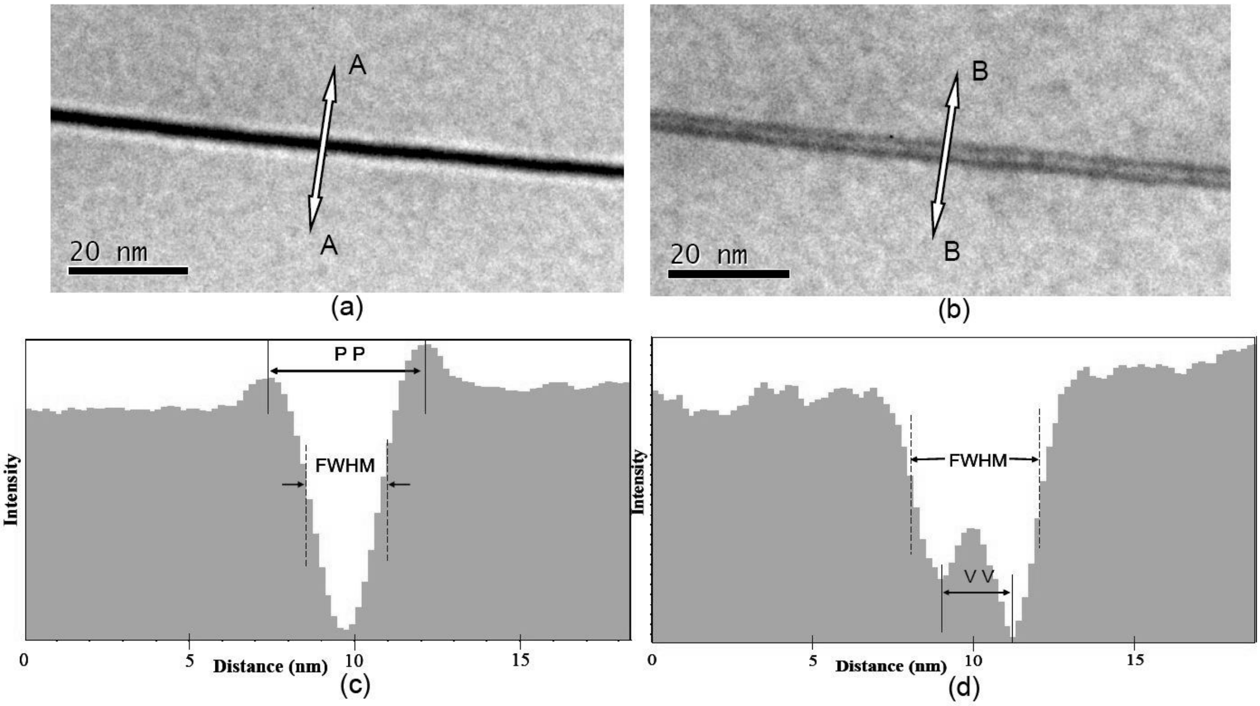

Fig. 2.6 FCIs and profiles across the GB from a Si_3N_4 sample doped with Lu-Mg: (a) FCI at a defocus value of +1.2 µm, (b) FCI at a defocus value of −1.2 µm, (c) plot of profile across the line AA integrated over a width of 18.8 nm, (d) profile across BB integrated over a width of 18.8 nm.

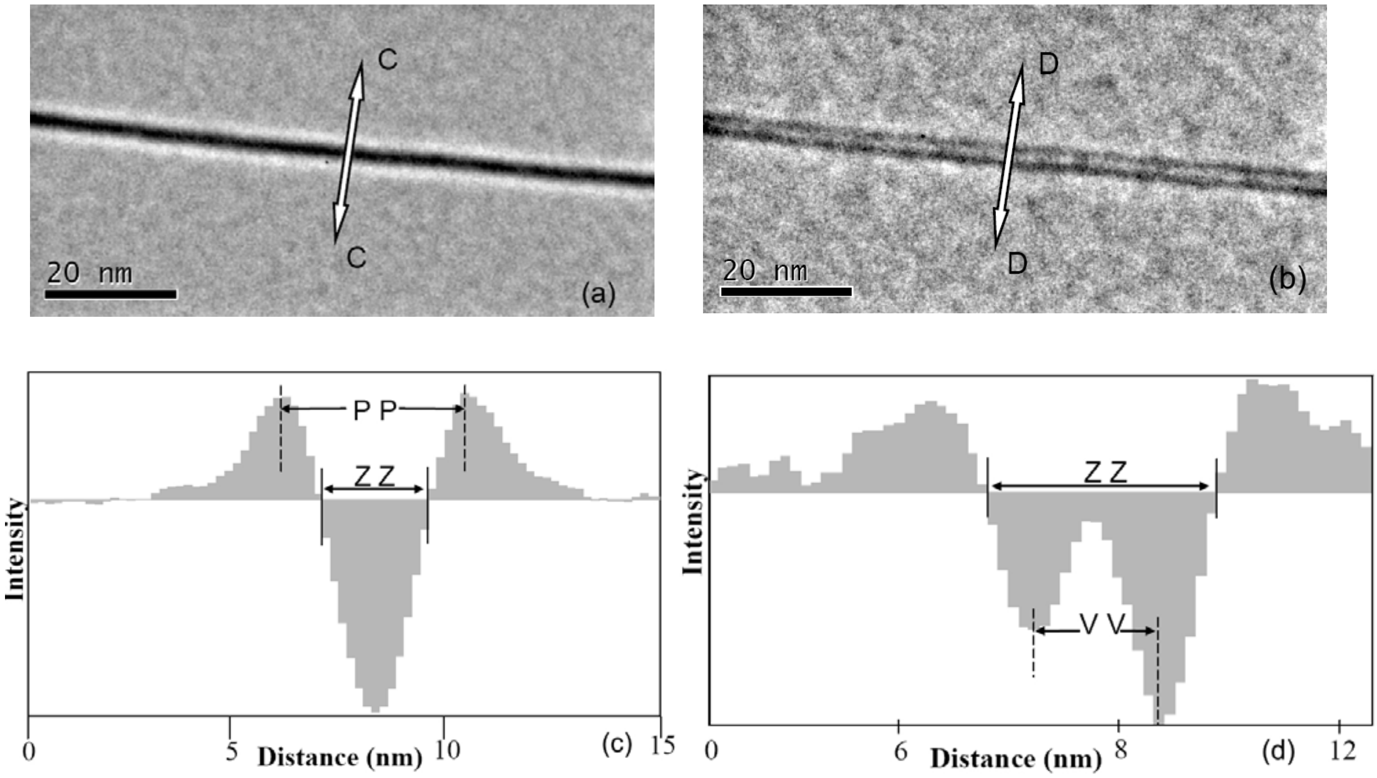

Fig. 2.7 FF-FCIs and profiles across the GB: (a) image obtained from Fig. 2.6a by FF the central spot, (b) image obtained from Fig. 2.6b by FF the central spot, (c) profile across CC integrated over a width of 18.8 nm, (d) profile across DD integrated over a width of 18.8 nm.

Potential Profile (scale for x-axis is in Å) *(comments)*	Fresnel contrast plots *(comments)*
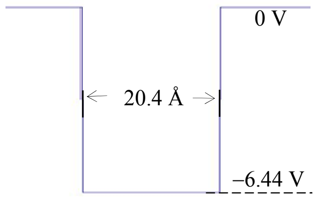 *(Standard square potential well)* P1 *(WPOA)*	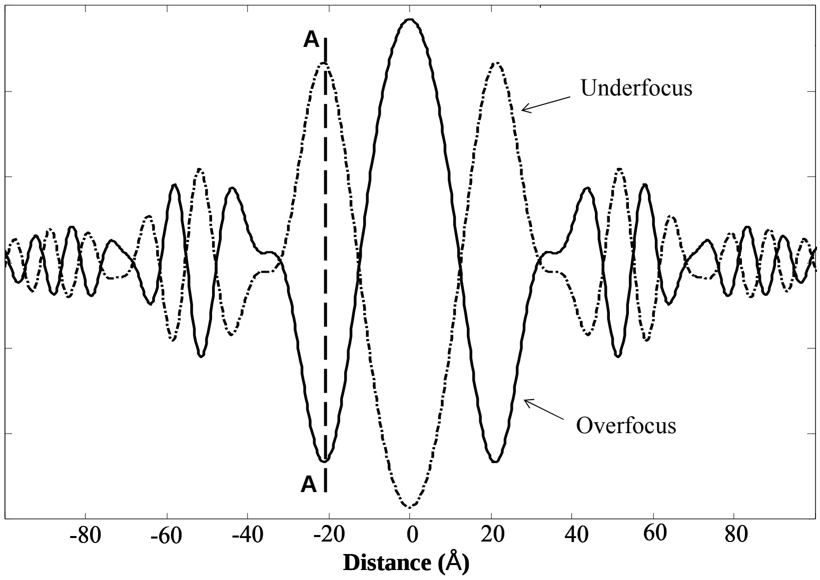 *(LR symmetry present and OU symmetry is approximate)*
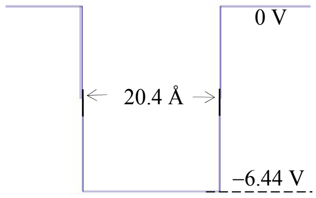 P1 *(POA)*	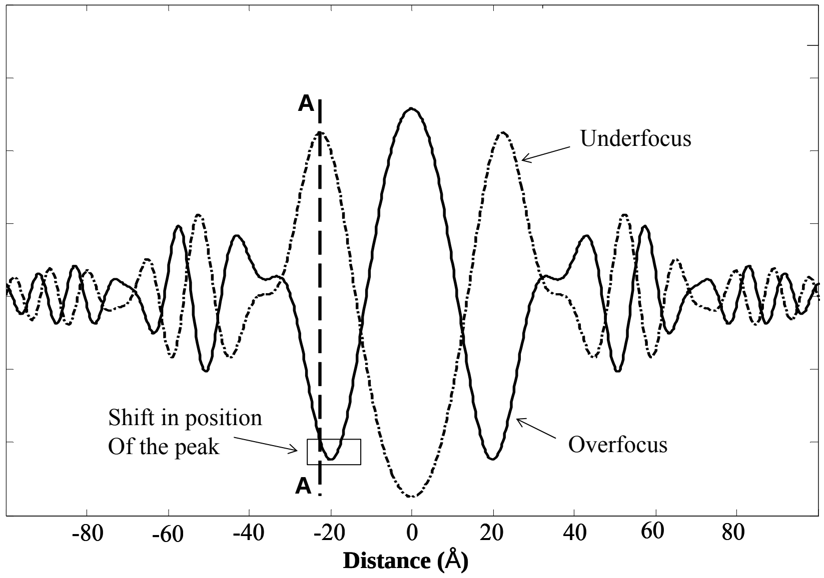 *(OU symmetry broken)*

(continued in next page}

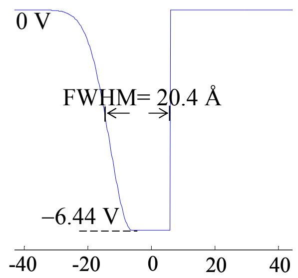 *(Profile with Left-Right asymmetry)* P2 *(WPOA)*	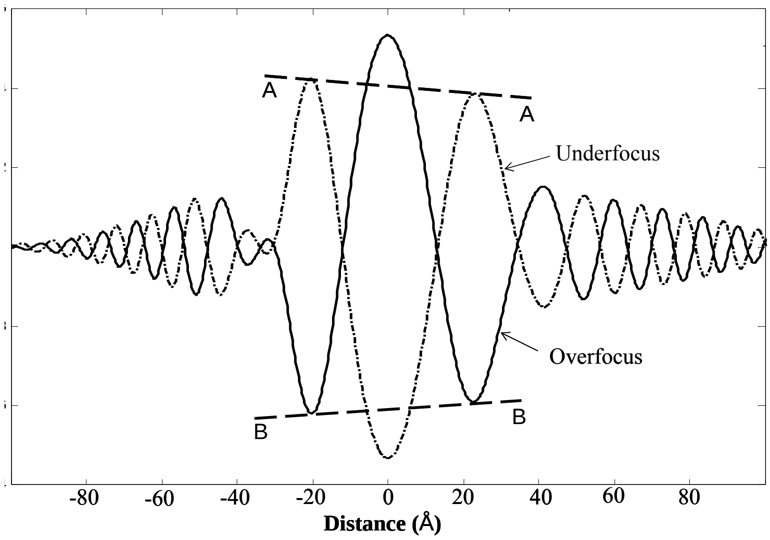 *(LR symmetry broken)*
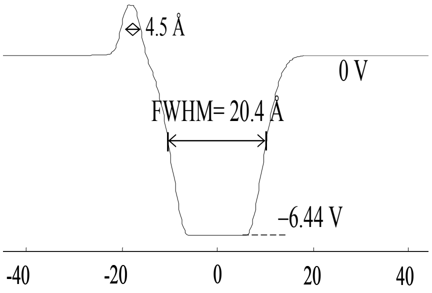 *(Profile reflecting segregation)* *P3* *(WPOA)*	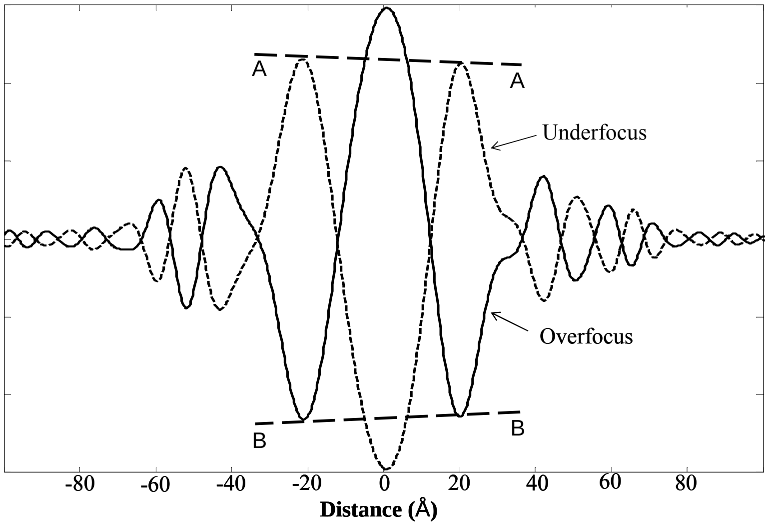 *(LR symmetry broken)*

Table 2.3 Effect of various IGF potential profiles and assumptions on the Fresnel contrast image (FCI) (WPOA= weak-phase-object approximation, Defocus=±2.2 μm, Cs = 2.7 mm)

In the standard Fresnel fringe extrapolation technique, a plot of fringe spacing (s) versus square root of defocus ($(\Delta f)^{1/2}$) is extrapolated to zero-defocus to obtain the thickness of the IGF. Fig. 2.8 shows the plot of s (measured from Fig. 2.5b-h) versus $(\Delta f)^{1/2}$ obtained from simulation using a square potential well (Fig. 2.5a). The following points are noted from the simulation (Fig. 2.5 & Fig. 2.8):

(i) At large defocus values ($|(\Delta f)| > 1.6$ μm) there are prominent primary fringes

(ii) At low defocus values (|(Δf)| < 1.4 μm) the intensity of the primary and secondary fringes are comparable (further it is observed that, the peak of the primary fringe is not distinct below |(Δf)| < 0.8 μm)

(iii) The linear fit in the plot of s vs. $(\Delta f)^{1/2}$ is not good for low defocus values (<1 μm)

(iv) Extrapolation to zero-defocus does not give the correct thickness of the IGF (a negative value of -13.46 Å is obtained). Instead, extrapolation to a defocus value where the 'primary' fringe is first visible (of ~ Δf = 0.8 μm) gives a good estimate of the thickness of the IGF (of ~ 20 Å)

An additional point to be noted is that, in an actual experiment with a microscope like the Zeiss-912, , the two peaks seen at an overfocus of 1.2 μm (labeled m1 and m2 in Fig. 2.5c), would be seen as one peak at an average spacing between m1 and m2. Hence, at low underfocus values, the measurements from an experiment would be an overestimate. This in itself would lead to a non-linear plot of fringe spacing versus $(\Delta f)^{1/2}$, even for a square potential profile.

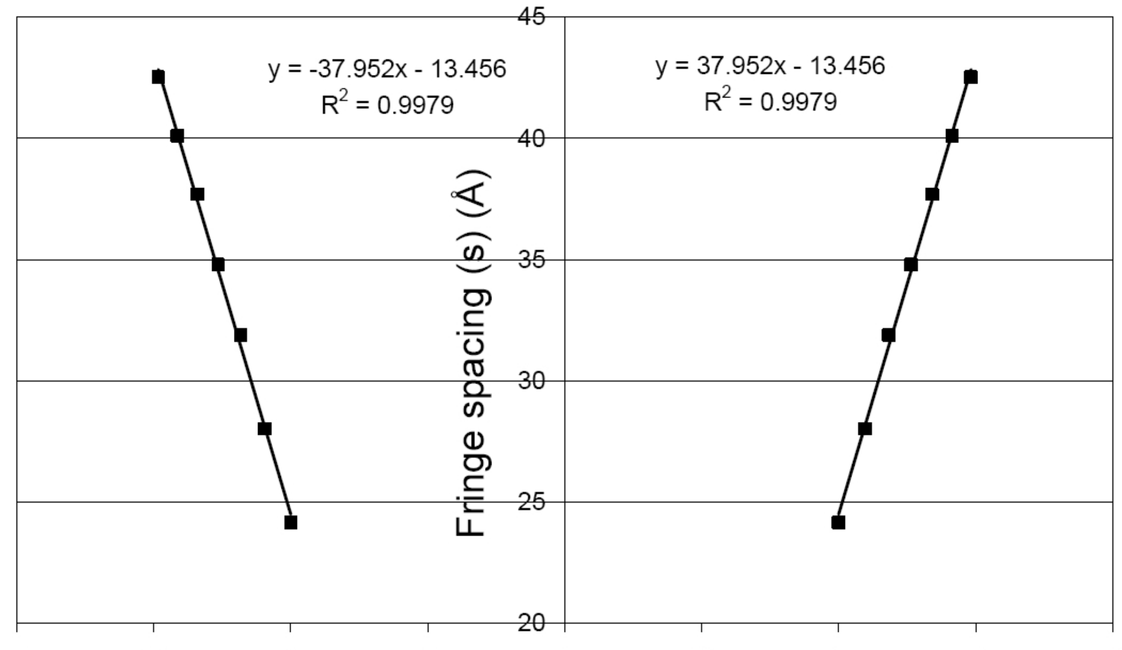

Fig. 2.8 Plot of fringe spacing (s) versus square-root of defocus $(\Delta f)^{1/2}$ for a square potential well (Fig. 2.5a). The fringe spacings are measured from Fig. 2.5b-h. The simulation parameters are: WPOA, C1, L1 & A0.

2.5 Measurement of thickness and comparison

2.5.1 Using Fresnel fringes hidden in high-resolution micrographs

To illustrate the utility of the Fresnel fringes hidden in high-resolution micrographs (HRM), two cases are considered in this section. In the first case (Lu-Mg doped Si_3N_4) the lattice fringes on one side are nearly parallel to the GB and hence a plot of the intensity profile across the IGF shows oscillations due to lattice fringes superimposed on the Fresnel fringe contrast. The stoichiometric $SrTiO_3$ sample is used to demonstrate the use of the method, when lattice fringes are very weak on one side of the IGF.

2.5.1.1 Case-1: Lu-Mg doped Si_3N_4

Fig. 2.9a shows the standard method of measurement of the thickness of an IGF from lattice fringe images in a HRM (HRt), taken at an overfocus of 40 nm. Fig. 2.9b shows the use of Fourier filtered HRM (FF-HRM) for the same (mask size M3). The use of FF-HRM corresponds to the technique of MacLaren [10] and the thickness measured is henceforth also referred to as MacLaren thickness. Fig. 2.9c shows the intensity profile across the IGF (from Fig. 2.9a), integrated over a width of 4.4 nm, showing hidden Fresnel fringe contrast. Fig. 2.9c also shows two distances which can be calculated from the profile: the Full width at half maximum (FWHM) and the valley to valley (VV) distance. Fig. 2.9d shows the intensity profile across the IGF from the Fourier filtered image (Fig. 2.9b). Fig. 2.9d also shows two ways of determining the thickness of the IGF based on the Fourier filtered image: the zero to zero (ZZ) distance and the valley to valley (VV) distance.

2.5.1.2 Case-2: stoichiometric $SrTiO_3$

Fig. 2.10 has an identical format to Fig. 2.9, but is taken from a grain boundary of the $SrTiO_3$ ceramic at an underfocus of 40 nm. It is seen that lattice fringes are very weak on one side of the IGF and hence a clear demarcation of the crystal-glass interface on that side is not possible from the HRM alone. Fig. 2.10c shows that there is no superimposition of high-resolution fringes with Fresnel fringes which leads to a straightforward measurement of the peak to peak spacing.

2.5.1.3 Comparison of the thicknesses measured

The essence of the methodology adopted above is illustrated in Fig. 2.11, which shows the measurement of thickness of an IGF in four different ways. A comparison of the thicknesses measured in Section 2.5.1.1 and 2.5.1.2 is shown in Table 2.4. It is seen that the valley to valley (VV) / peak to peak (PP) distance measured from the profiles (raw and Fourier filtered data) correlates well with the thickness calculated from MacLaren's technique and the FWHM (from profile of raw data) and zero to zero (from profile of Fourier filtered data) distances have a good correspondence with the HRt.

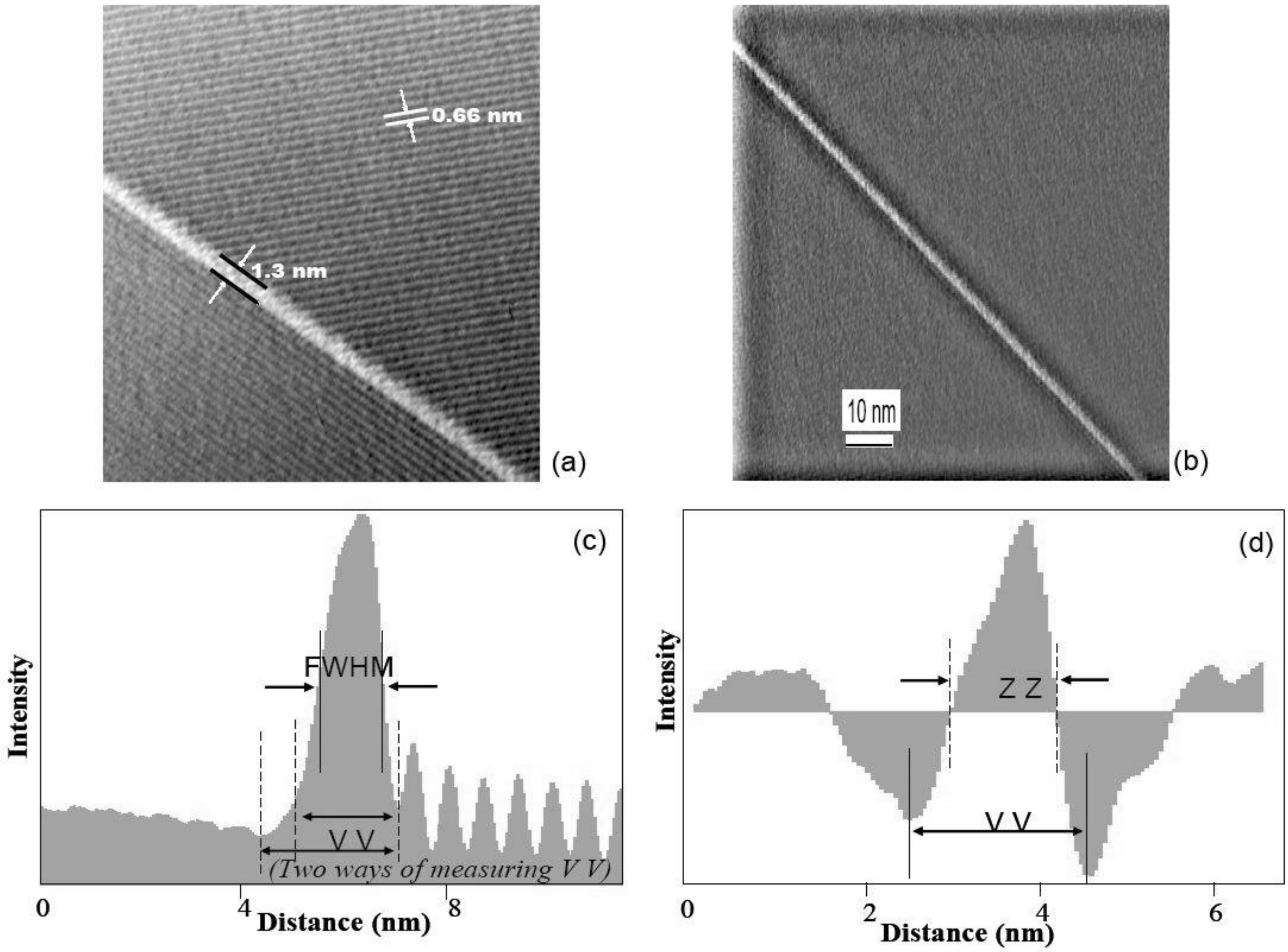

Fig. 2.9 Use of high-resolution micrographs (HRM) for the measurement of the thickness of an IGF in a Lu-Mg doped Si_3N_4 sample: (a) HRM, (b) FF-HRM, (c) profile across the GB in the HRM integrated over a width of 4.4 nm, (d) profile across the GB in the FF-HRM (integrated over a width of 8.8 nm).

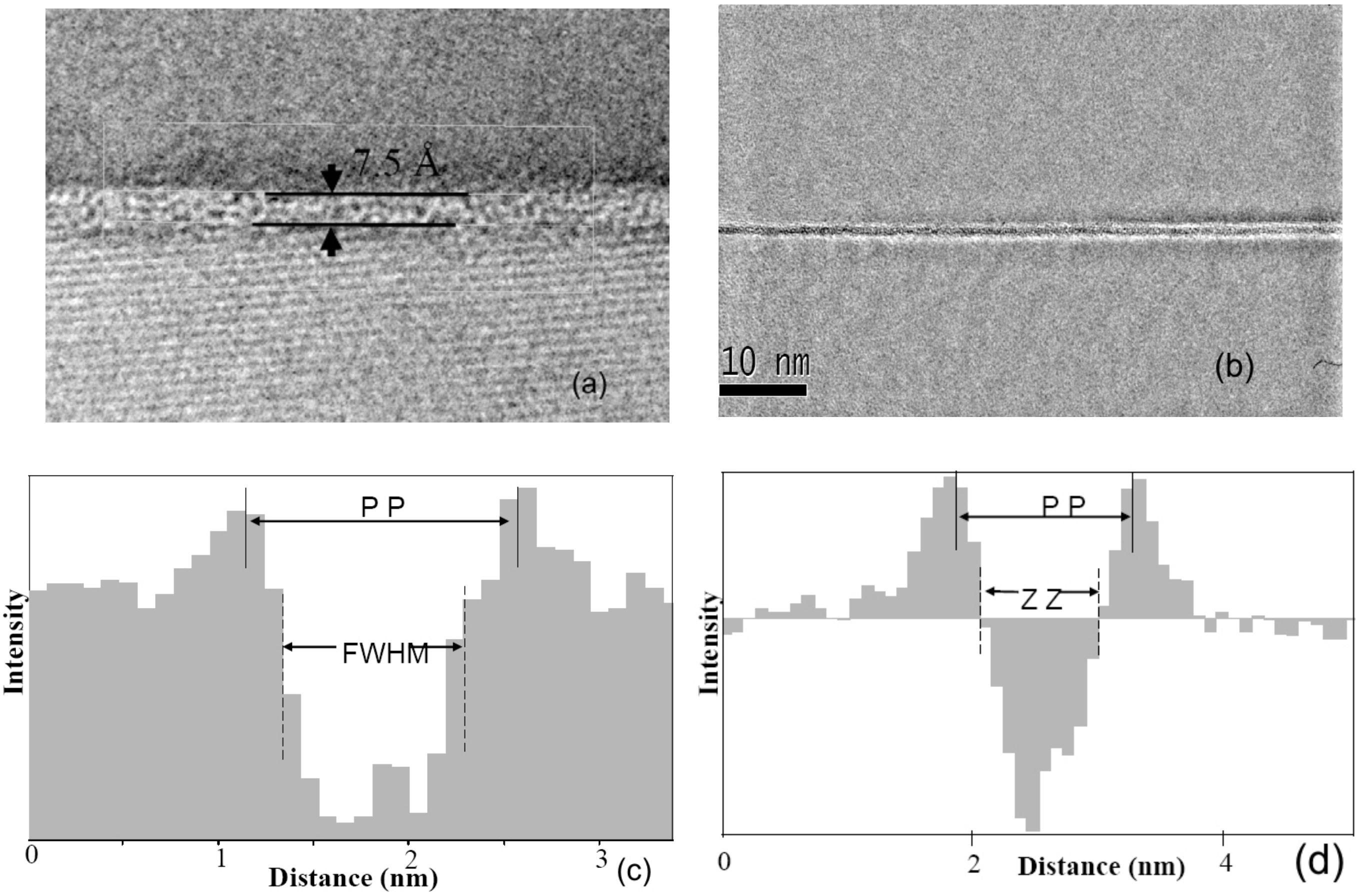

Fig. 2.10 Measurement of the thickness of an IGF in the stoichiometric $SrTiO_3$ (STO1): (a) HRM, (b) FF-HRM, (c) profile across the GB in the HRM, (d) profile across the GB in the FF-HRM. It is to be noted that the lattice fringes are weak on one side of the IGF.

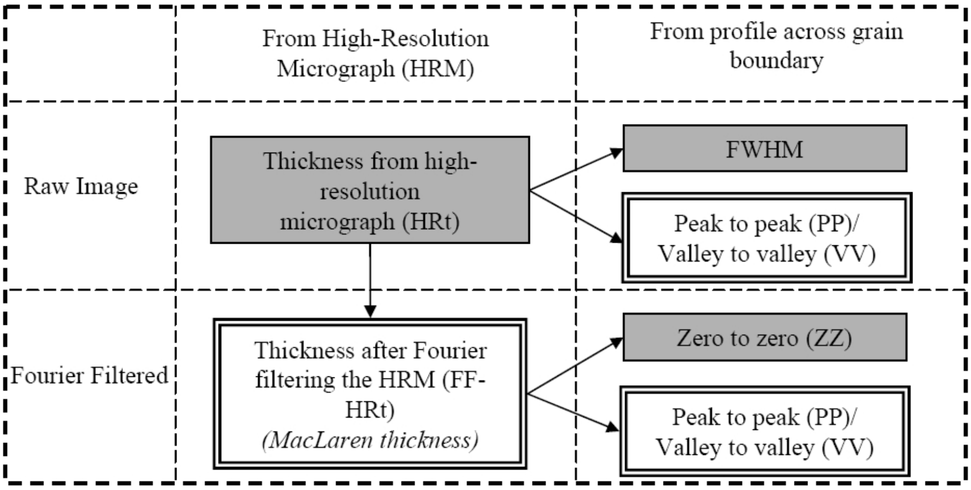

Fig. 2.11 Schematic showing the measurement of thickness from HRM. Thickness can be calculated directly from the HRM (HRt) or by Fourier filtering the lattice fringes from the micrograph (FF-HRt). An easier alternative is to use the plot of profiles across these images. Values which correlate with each other are shown either by same shading or with the same border.

Sample *(Lattice fringe orientation)*	HRt (nm)	FF-HRt (Maclaren thickness) (nm)	From intensity (Fresnel) profiles			
			Ft (nm)		FF-Ft (nm)	
			FWHM	PP/VV	Z-Z	PP/VV
Lu doped Si_3N_4 *(parallel to GB on one side)*	**1.18**	1.95	**1.18**	1.98-2.6*	**1.18**	1.98
Stoichiometric $SrTiO_3$ (STO1) *(not parallel to GB on either side)*	0.95	*1.51*	0.95	*1.53*	0.94	*1.51*

* Depending on the choice of the VV distance

Table 2.4 A comparison of the values of thickness obtained from High-Resolution Micrograph (HRt) and from the plot of intensity profiles across the IGF revealing Fresnel fringes (Ft). Additionally, the high-resolution image is Fourier filtered (FF) to obtain the MacLaren thickness (FF-HRt) and the FF Fresnel thickness (FF-Ft); as measured from the intensity profile across the FF image. Correspondences are shown, either by similar shading, similar border or by similar font.

2.5.2 Use of Conventional Fresnel fringes

2.5.2.1 Extrapolation of Fourier filtered Fresnel fringe spacing data

Table 2.5 shows a compilation of the distances measured from Fig. 2.6 and Fig. 2.7, obtained at defocus values of ±1.2 μm, from the Si_3N_4 sample. The microscopy was performed on the Zeiss-912 machine, using the in-column energy filter. It is seen that the measured FWHM from the FCI correlates well with the ZZ distance from the FF-FCI and PP/VV from the FCI is similar to PP/VV distance from the FF-FCI. These correlations are illustrated schematically in Fig. 2.12.

Condition	Fresnel data (nm)		Fourier filtered Fresnel data (nm)	
	FWHM	PP/VV	ZZ	PP/VV
Overfocus (+)	2.26	4.14	2.45	4.33
Underfocus (–)	3.77	2.07	3.96	2.07

Table 2.5 A comparison of the fringe spacing values obtained from profiles across under and overfocus FCI taken at a defocus value of ± 1.2 μm . The terms FWHM, PP, VV AND ZZ are defined in Fig. 2.6 and Fig. 2.7.

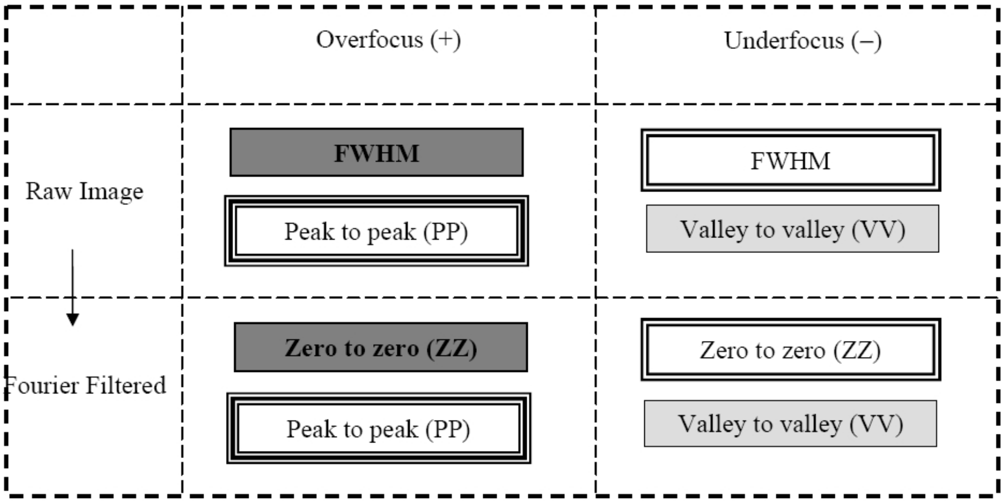

Fig. 2.12 Schematic diagram showing the use of Fresnel fringe spacing data for the calculation of thickness of an IGF. Raw and Fourier filtered images are considered for under and overfocus conditions. Spacing which correspond to each other have been shaded identically or have identical borders. Correlation between underfocus and overfocus fringe spacings are shown by similar but different shading or border.

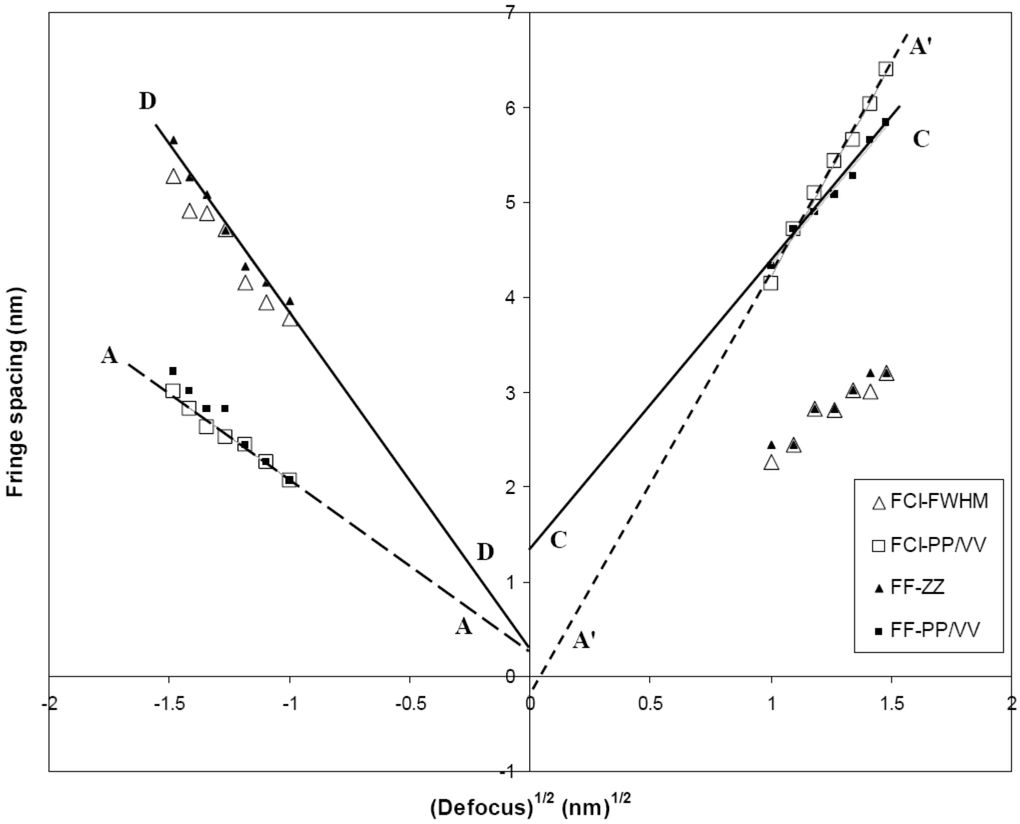

Fig. 2.13 Plot of the fringe spacing data obtained from FCI and FF-FCI (Lu-Mg doped Si_3N_4 sample). The distances plotted are: FCI PP/VV, FCI FWHM, FF-FCI PP/VV and FF-FCI ZZ. Lines AA and A'A' are the extrapolation of the data of FCI PP/VV. Lines CC and DD are the extrapolation of the overfocus data in FF-FCI PP/VV and underfocus data in FF-FCI ZZ. Each data point is associated with an error bar of ±0.2 nm (the error bars are not plotted for clarity). Thickness of the IGF is obtained by extrapolating the lines to zero-defocus.

The difficulties related to the standard Fresnel fringe extrapolation technique and the possible ways to overcome those problems are discussed in the following. The plot of the Fresnel fringe spacing data for the two methods (i.e., from the raw image and from the

Fourier filtered image) of measuring the fringe spacing are shown in Fig. 2.13. The data is extrapolated to zero-defocus value to obtain the thickness of the IGF by: (a) the standard method (dashed line in the figure), (b) the data obtained by FF-FCI (solid line in the figure). The thickness of the IGF (from Fig. 2.13) by the standard method is ~0 nm while the thickness calculated from Fourier filtered images is 0.9 nm. It is clearly seen that the FF method gives an estimate closer to the value obtained by HRM (1.3 nm).

Fig. 2.14a shows the plot of the data from FF-FCI (FF-ZZ) obtained from a GB containing an IGF from the non-stoichiometric $SrTiO_3$ sample (STO2). The microscopy was performed on the JEOL 4000EX machine. The figure shows a plot of FF-ZZ versus the root of defocus ($(\Delta f)^{1/2}$). Due to noisy images close to zero-defocus, the measurement of peak to peak (PP) distance is prone to error and hence ZZ distance is chosen for the plot (e.g. Fig. 2.14b shows the profile across a FF-FCI taken at a defocus of −10nm). Additionally, due to non-straight boundaries (unlike the Si_3N_4 sample) (Fig. 2.14c), integration over long distances along the IGF (to reduce noise), is not possible. It is seen that close to zero-defocus ($\leq\pm40$ nm) the plot of s versus $(\Delta f)^{1/2}$ is not linear. However, at larger defocus values the curve is linear. The regions of linearity are marked in the Fig. 2.14a. One of the reasons for the overestimate of the spacing at low defocus values, as compared to a linear plot, could be the same as the one mentioned in Section 2.4 (i.e. the primary and secondary peaks in the FCI, could be seen as one peak with an average spacing).

2.5.2.2 Zero-defocus images

As in the case of the Fresnel fringes hidden in HRM, the zero-defocus images can also be used for the measurement of the thickness of an IGF. Fig. 2.15a shows the FF-FCI obtained from an image taken at zero-defocus from the Si_3N_4 sample. The inset in the figure (Fig. 2.15b) shows the profile across the IGF integrated over a width of 12.4 nm. The thickness measured from the profile (ZZ distance) is 1.2 nm which correlates well with the HRt of 1.2 nm. This method of zero-defocus imaging applied to a GB in the STO2 sample gives the thickness of the IGF as 1.2 nm (Fig. 2.14a). The thickness measured from the HRM (Fig. 2.14c) is about 1.0 nm. Only an approximate value could be obtained from the HRM due to the bent nature of the GB and local variations in the thickness. Fig. 2.16 illustrates the utility of zero-defocus images for the case of a dry boundary (Zero thickness). Fig. 2.16a shows the HRM and Fig. 2.16b shows the intensity profile across the FF-FCI. It is to be noted that the accuracy of determination of the thickness from a zero-defocus image is dependent on the accuracy with which the zero-defocus is set. FF-FCI comes to the aid here too and a practical approach would be, to determine the minimum thickness, from a series of images (FF-FCI) near expected zero-defocus. The zero-defocus condition can be chosen from the series of images, corresponding to the image at the minimum thickness measured or in the middle of a range of defocus values where the thickness is nearly constant.

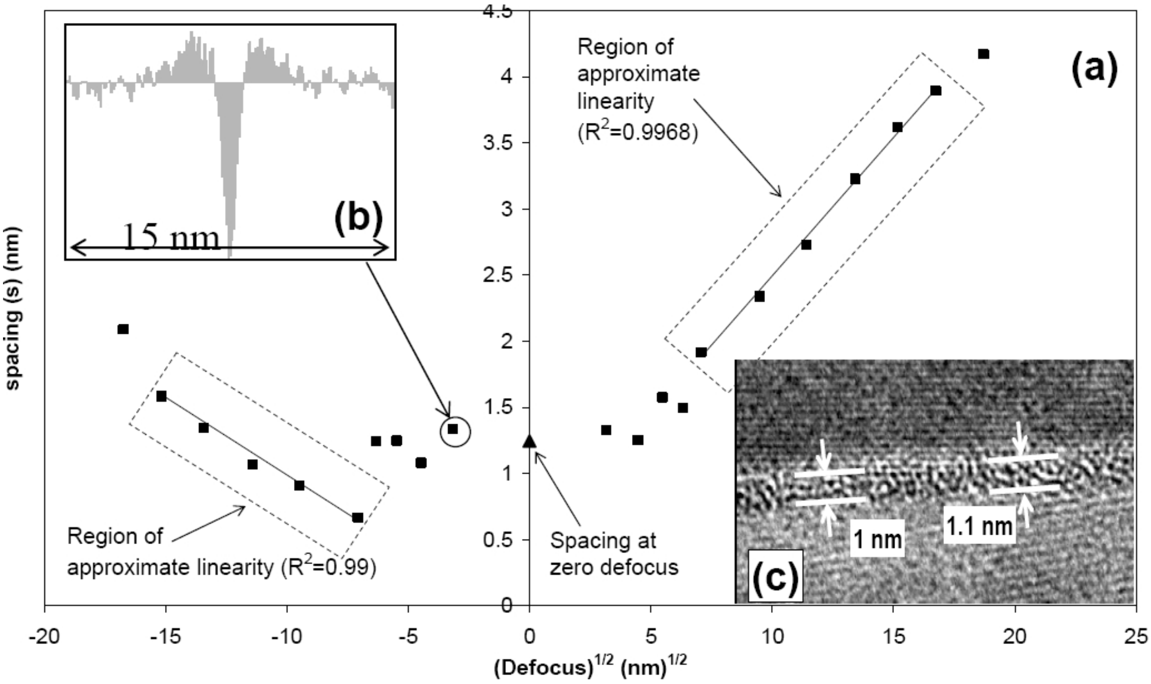

Fig. 2.14 FF-FCI ZZ data obtained from a GB containing an IGF from the non-stoichiometric $SrTiO_3$ (STO2) sample: (a) plot of the spacing (s) versus the root of defocus ((Δf)$^{1/2}$), (b) profile across an image taken at an underfocus of 10nm, integrated over a width of 12.4 nm.

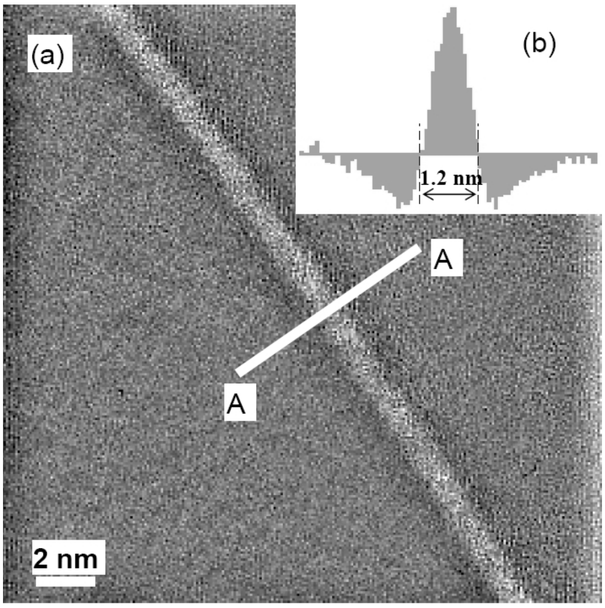

Fig. 2.15 Utility of zero-defocus FF-FCI in measuring the thickness of the IGF from the Si_3N_4 sample: (a) FF-FCI, (b) plot of the profile across AA integrated over a width of 12.4 nm.

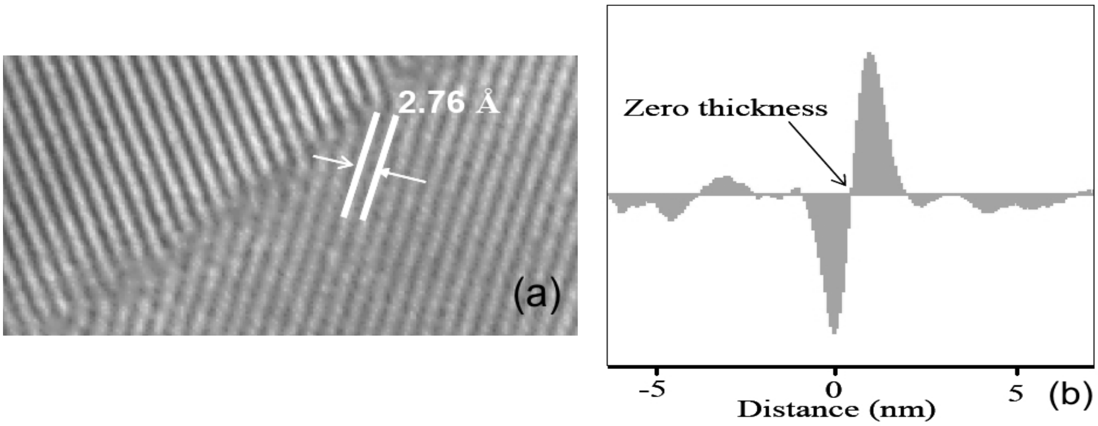

Fig. 2.16 Illustrative case for the use of zero-defocus images from a dry GB in $SrTiO_3$ (STO1): (a) HRM, (b) profile across the FF-FCI showing zero thickness.

2.6 Discussion

2.6.1 Fourier filtering of high-resolution micrographs

Due to microscope or material imposed constraints, it is sometimes not possible to obtain lattice fringes from both sides of the IGF. Previously such a HRM would be considered useless for the measurement of the thickness of an IGF. Using profiles across the FF-HRM the utility of such images can be enhanced and thickness of the IGF can be measured (as shown in Fig. 2.9 & Fig. 2.10).

It is seen that the procedure developed yields good results for two samples of vastly different nature (Si_3N_4 and $SrTiO_3$). The Si_3N_4 sample has mainly faceted grains (implying straight GBs) with sizes in the region of tens of nanometers, , and almost all the GB have IGFs. On the other hand the $SrTiO_3$ sample has grain-sizes of about 50 μm with curved GBs. Additionally, most of the GBs in the stoichiometric $SrTiO_3$ sample are dry [31]. Furthermore, different microscopes and defocus values were chosen to test the applicability of the method under a wider range of conditions. High-resolution microscopy on the Si_3N_4 sample was done on the JEOL 4000FX microscope (with a point-to-point resolution of 0.2 nm) and an overfocus value of 40nm was used for imaging. Microscopy on the $SrTiO_3$ samples was done on the JEOL 4000EX instrument (with a point-to-point resolution of 1.8 nm) at an underfocus of 40 nm.

2.6.2 Extrapolation of fringe spacing data for measuring IGF thickness

The technique of extrapolation of Fresnel fringe spacing data has proved to be a useful tool for the measurement of the thickness of IGFs. Unfortunately the Fresnel contrast obtained from many grain boundaries is poor. Additionally, there could be considerable scatter in the fringe spacing data, leading to a reduced accuracy of the extrapolation. Determination of zero-defocus using Fresnel contrast has also proven tricky. These problems are further compounded in the case of diffuse interfaces as the model for extrapolation is based on a square potential well (linear plot of spacing versus $(\Delta f)^{1/2}$). The presence of these issues is encountered even during the present investigation.

From the simulated Fresnel profiles in the current work (Fig. 2.8) and the work of Rasmussen and Carter [4] (Fig.6, Model A in the paper replotted as Fig. 2.17), it is seen that, the linearity in the plot of s versus $(\Delta f)^{1/2}$ is valid in certain regions only. Furthermore, extrapolation of the fringe spacing data does not lead to the correct value of thickness. From simulation of Fresnel intensity profiles, it is seen that both LR and OU symmetries, present in an ideal (using WPOA) Fresnel profile, could be broken; as seen in the results of the simulations (Table 2.3). However, due to limitations of an 1D potential profile, different kinds of profiles can lead to similar features in Fresnel contrast and hence, it is not possible to separate some of the structural effects causing the asymmetry in the potential profile.

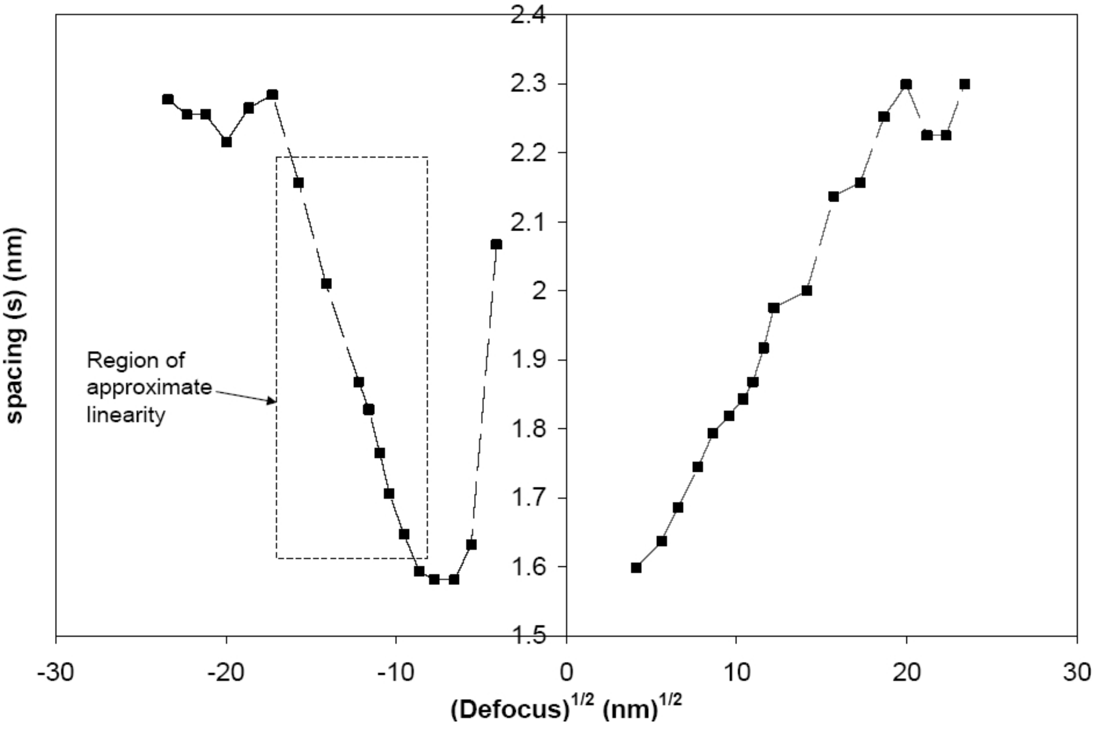

Fig. 2.17 Replot of data from Rasmussen and Carter [14] (Fig.6, Model A in the paper) showing Left-right (LR) asymmetry and regions of validity of linear s versus $(\Delta f)^{1/2}$.

In the current work (Lu-Mg doped Si_3N_4 sample) it is seen that some objectivity can be introduced into the calculations based on Fresnel fringe images. Instead of using the VV distance in underfocused images, use of the FWHM distance (Fig. 2.6) results in better symmetry between underfocus and overfocus data plots. It is seen that measurement of the ZZ distance in the FF-FCI (Fig. 2.7) is easier than measuring the FWHM. The reason for the restoration of symmetry by this procedure is not clear at this point, but in light of the presented simulations it is satisfactory that a reasonable value for the thickness of the IGF can be obtained by this method. However, given the limited validity of the extrapolation technique, it is rather surprising that the method works, albeit with limited precision. The reason for the good results obtained by the previous investigators, using the extrapolation technique on Si_3N_4 samples of different compositions ((i) Y_2O_3 + MgO doped Si_3N_4 [3], (ii) high-purity Si_3N_4 [12]), is also not understood in the light of the current research. It is to be noted that the previous investigators, instead of plotting s versus $(\Delta f)^{1/2}$, had plotted s versus Δf and had used this non-linear plot for extrapolation. Plot of s versus $(\Delta f)^{1/2}$ is better for visualization of the trends, especially in the linear regimes.

2.6.3 Fourier filtering of zero-defocus images

Fourier filtering of standard FCI enhances the contrast of that image. The zero-defocus value can be accurately set by using FF-FCI, as contrast is very poor under these low defocus conditions (Fig. 2.14). This enhancement in contrast also allows us to extend the useful range of defocus values from which fringe spacing data can be obtained. The thickness measured from zero-defocus FF-FCI is in good correspondence with that measured from HRM; the reason for which can be understood by simulating the 1D intensity profiles from potential profiles across the IGF. This neatly ties back well with the utility of the hidden Fresnel fringes in HRM for thickness measurement. As apparent, the resolution of the microscope needs to be good for ideal correspondence.

2.6.4 Different measurements of IGF thickness

Two IGF thicknesses were calculated by MacLaren [10] (HRM and FF-HRM). Using the current method it is seen that these values can be correlated well with the values obtained from hidden Fresnel fringes. The question as to where the boundary between the glass and the crystal should be drawn has remained somewhat arbitrary so far. Using hidden Fresnel fringes this issue can be objectively addressed and the measurement can be made more rigorous, by using the ZZ distance of the intensity profile across the IGF in FF-HRM (especially if there are local variations in thickness). A direct correlation is seen between the thicknesses obtained from HRM (HRt and FF-HRt) and the thicknesses measured using hidden Fresnel fringes (Table 2.4 and Fig. 2.9). The reason for this correlation can be understood from the simulations shown in Fig. 2.4c and e. As the HRMs (Fig. 2.9a, Fig. 2.10a) are taken at low defocus values, the FWHM of the boundary width captured in the FF-HRM, is not much different from the true width, which would be measured from a zero-defocus image. It is to be noted that (as also seen in Fig. 2.14), the Fresnel fringe spacing (ZZ) is an insensitive function of the defocus at low defocus values. Hence, the error introduced by imaging at low defocus values (as in the case of hidden Fresnel fringes in the high-resolution microscope) is small. However, under ideal conditions zero-defocus should be used.

For other material/microscope combinations, the microscopic parameters (defocus values, size of the objective aperture etc.) which give such correlations may have to be worked out.

In this context it should be noted that the HRt is usually thought to be representative of the core of the IGF (the width 'a' in Fig. 2.2a), i.e. it captures the part of the IGF with close to 100% amorphicity (Fig.2.3a). As the HRt is equal to the ZZ distance in the zero-defocus FF-FCI, which in turn is a measure of the FWHM of the potential profile (simulations: Fig. 2.2a, Fig. 2.4e); the HRt corresponds to the FWHM of the potential profile and not the inner width 'a'. Another way of interpreting the result would be to conclude that the IGF has no 'core' region and is fully diffuse (i.e. the diffuse profiles overlap). A note of caution here would be that, the FWHM could over or under-represent the width, depending on the shape of the potential profile (especially for very peculiar shaped profiles), and the correlations seen above can be assumed to be valid for 'reasonably shaped' potential profiles. As the MacLaren thickness is always greater than HRt, so, it might be the distance between the shoulders of the potential profile (distance a_0 in Fig. 2.2a) across the IGF.

2.6.5 Mask size needed for Fourier filtering

The optimum size of the mask used in Fourier filtering has been determined by calculations using a potential profile representing a diffuse interface. Real crystal-glass interfaces could have profiles which are far more complicated, especially in the presence of rare-earth additives to the ceramic, which could segregate to the interface. Additionally, the two interfaces could be different, breaking the symmetry assumed in an ideal mathematical model. The calculations show that the size of the mask is very important, as was to be expected. However, a change of 20-30% in mask size does not significantly affect the values measured from the Fourier filtered image. A simple rule of thumb can be derived from the calculations based on the ideal profile. These show that a mask having a size of $0.2/a_{FWHM}$ to $0.3/a_{FWHM}$ (a_{FWHM} is the FWHM of the GB potential profile) gives good results.

Finally, it should be noted that the above procedures may not be useful/needed for certain ideal choice of materials/microscopes.

2.7 Summary and conclusions

(i) The utility of Fresnel contrast and high-resolution images can be enhanced by Fourier filtering the images. This methodology, applied to high-resolution micrographs, allows the use of images in which lattice fringes are weak (or even absent) on one side of the IGF and in the case of Fresnel contrast images gives better interpretability from noisy images.

(ii) A simple new technique is put forth, wherein Fresnel contrast hidden in high-resolution images is used to objectively demarcate the glass-crystal interface and to measure the thickness of an IGF (by Fourier filtering the lattice fringes). The optimum mask size was determined by simulations on one-dimensional scattering potential profiles.

(iii) Experimental results (on Si_3N_4 doped with Lu-Mg and stoichiometric & non-stoichiometric $SrTiO_3$) and simulations show that the plot of fringe spacing (s) versus root of defocus ($(\Delta f)^{1/2}$) is not linear over the entire defocus range but only at intermediate defocus values. Other limitations of the Fresnel extrapolation technique are also enumerated, including the important observation that the correct thickness of the IGF is not obtained by this method.

(iv) A new method is developed wherein Fresnel fringe spacing is measured based on Fourier filtered Fresnel images. Appropriate choice of spacing values from over- and underfocus images is seen to give a better symmetry in plots of Fresnel fringe spacing data. It is also seen that this technique gives a better estimate of the thickness of the IGF from the same set of Fresnel contrast images by extrapolation to zero-defocus. The approximate validity of the extrapolation method could not be understood in the framework of the simulations performed.

(v) Simulations of Fresnel contrast using one-dimensional potential profiles have been used for understanding the different sources of left-right (LR) and underfocus-overfocus (OU) symmetry breaking being observed in experimental Fresnel contrast images (FCI).

(vi) In light of the limitations of the Fresnel extrapolation method a new technique for the Measurement of the thickness of IGFs based on Fourier filtered zero-defocus images has been tested on Si_3N_4 doped with Lu-Mg and non-stoichiometric $SrTiO_3$ samples. This has been found to be the simplest technique for the purpose of estimating the high-resolution thickness without actually performing lattice fringe imaging. Simulations are used to validate the method.

(vii) Thickness measured from lattice fringe imaging (HRt) is equal to the zero-to-zero distance in the zero-defocus FF-FCI (hidden in HRM or otherwise), which in turn is a measure of the FWHM of the potential profile (as seen in simulations). This implies: (a) the HRt corresponds to the FWHM of the potential profile and not the inner width ('a') or (b) the IGF is fully diffuse. The current work is not able to differentiate between the two cases. The measure of IGF thickness used by MacLaren [10] might be the distance between the shoulders of the potential profile across the IGF.

2.8 References

[1] H.-J. Kleebe, J. Ceram. Soc. Jpn. 105 (1997) 453.

[2] H.-J. Kleebe, J. Eur. Ceram. Soc. 10 (1992) 151.

[3] M.K. Cinibulk, H.J. Kleebe, M. Rühle, J. Am. Ceram. Soc., 76 (1993) 426.

[4] D. R. Rasmussen, C. B. Carter, Ultramicroscopy, 32 (1990) 337.

[5] C.T. Koch, S. Bhattacharyya, A. Subramaniam, and M. Rühle, Microscopy and Microanalysis, 10 (Suppl.) (2004) 254.

[6] N. Shibata, S.J. Pennycook, T.R. Gosnell, G.S. Painter, W.A. Shelton, P.F. Becher, Nature 428 (2004) 730.

[7] G.B. Winkelman, C. Dwyer, T.S. Hudson, D. Nguyen-Manh, M. Döblinger, R.L. Satet, M.J. Hoffmann, and D.J.H. Cockayne, Appl. Phys. Lett. 87 (2005) 061911.

[8] M. Elfwing and E. Olsson, J. Appl. Phys. 92 (2002) 5272.

[9] Y.K. Simpson, C.B. Carter, K.J.Morrissey, P. Angelini, J. Bentley, J. Mat. Sci. 21 (1986) 2689.

[10] I. MacLaren, Ultramicroscopy 99 (2004) 103.

[11] D.R. Clarke, Ultramicroscopy 4 (1979) 33.

[12] Q. Jin, D.S. Wilkinson, G.C. Weatherly, J. Eur. Ceram. Soc. 18 (1998) 2281.

[13] J.N. Ness, W.M. Stobbs, T.F. Page, Phil. Mag. A 54 (1986) 679.

[14] D.R. Rasmussen, C.B. Carter, Ultramicroscopy 32 (1990) 337.

[15] F.M. Ross, W.M. Stobbs, Phil. Mag. A 63 (1991) 37.

[16] R.E. Dunin-Borkowski, Ultramicroscopy 83 (2000) 193.

[17] J.C. Loudon, S.J. Lloyd, P.A. Midgley, N.D. Mathur, Inst. Phys. Conf. Ser. 168 (2001) p.449.

[18] Y.G. Wang, V.P. Dravid, Phil. Mag. Lett. 82 (2002) 425

[19] S. Bhattacharyya, C.T. Koch and M. Rühle, Ultramicroscopy (2005) submitted (Chapter 5)

[20] H. D. Ackler, Thermodynamic calculations and model experiments on thin intergranular amorphous films in ceramics, Ph.D. Thesis, Massachusetts Institute of Technology, Boston, 1997.

---

[21] M. Bobeth, D. R. Clarke, W. Pompe, J. Am. Ceram. Soc., 82 (1999) 1537.

[22] A. Ziegler, J. C. Idrobo, M. K. Cinibulk, C. Kisielowski, N. D. Browning, R. O. Ritchie, Science 306 (2004) 1768.

[23] M. Döblinger, D.J.H. Cockayne, R.R.Meyer, A.I.Kirkland, D.N. Manh, Proceedings of the 13th European Microscopy Congress (Eds.: D. Schryvers and J-P. Timmermans), Belgian Society for Microscopy, Liège, Vol. II (2004) 59.

[24] D.B. Williams, C.B. Carter, Transmission Electron Microscopy, Plenum Press, New York, 1996 p.492-93.

[25] R.L. Satet, M.J. Hoffmann, Key Engg. Mater. 264-268 (2004) 775.

[26] W.M. Stobbs, F.M. Ross, Evaluation of advanced semiconductor materials by electron microscopy, NATO ASI Series B, Vol. 203, D. Cherns (Ed.), Plenum press, London, 1989, p.183.

[27]D.R. Clarke, Ultramicroscopy 4 (1979) 33.

[28] C.T. Koch, S. Bhattacharyya, M. Rühle, R. L. Satet, M.J. Hoffmann, Microsc. Microanal., (2005) accepted.

[29]L.M. Peng, Micron 30 (1999) 625.

[30] J.C.H. Spence, Experimental high-resolution electron microscopy, Clarendon press, Oxford, 1981.

[31] A. Subramaniam, S. Šturm, C.T. Koch and M. Rühle, Grain boundaries in stoichiometric polycrystalline $SrTiO_3$, to be communicated.

CHAPTER 3

The evolution of amorphous grain boundaries during In-situ heating experiments in Lu-Mg doped Si_3N_4

S. Bhattacharyya, A. Subramaniam, C.T. Koch, R.M. Cannon and M. Rühle

Materials Science and Engineering: A, accepted

Abstract

The presence of 1-2 nm wide intergranular glassy films (IGF) found in ceramics such as Si_3N_4 and SiC strongly influences the properties of the material, including its fracture and creep behaviour. It is therefore important to know the evolution of the film as a function of temperature. Experiments, wherein liquid phase sintered Si_3N_4 samples were quenched from high temperatures, have been carried out before and shown intriguing results. In the current investigation, in-situ heating experiments have been conducted in 120 kV and 400 kV microscopes, in order to separate beam irradiation from temperature effects. Based on the literature, it was expected that no changes would occur to the IGF below 1000°C. However, it was surprising to note that the thickness measured at 950ºC was higher than that at room temperature. The correlation in trends observed in both microscopes shows that electron radiation has a minimal contribution to the change in IGF width at 950ºC. No change to the thickness was observed when heating up to 650ºC. After cooling back to room temperature there is a reduction in the thickness and thus a tendency to regain the original value of the thickness before heating. We conclude from these observations that certain material transport processes could be active at rather low temperatures (for Si_3N_4). Possible mechanisms and sources of artifacts are also discussed.

3.1 Introduction

It was an important realization, that in ceramic systems like Si_3N_4, SiC, $SrTiO_3$ etc., equilibrium thickness Intergranulaur Glassy Film (IGF) are present at grain boundaries [1]. This film is found to be resistant to crystallization and cannot be removed by usual post sintering heat treatments [2]. IGFs play an important role in determining the mechanical properties of the ceramic, such as fracture [3] and creep [4,5].

Important theoretical advances which have led to a better understanding of IGFs include: the force balance model of Clarke [6], the diffuse interface description of Bobeth et al [7], the phase field model [8] and the wetting/adsorption approach [9,10].

Experiments have been carried out which have enhanced our understanding of the effect of various stimuli and treatments like pressure [11], heating [4], oxidation [12], creep [13,4] etc., on the evolution of the IGFs. It is seen that pressure can lead to desegregation (dry boundaries) in the Bi_2O_3 doped ZnO ceramic [11]. The important point in the experiment by Wang and Chiang [11] is that: annealing at ambient pressure (650ºC, 24h), restored the 1-1.5 nm thick IGF, thus showing the reversibility of the process (of loss of IGF) and establishing that IGF is an equilibrium configuration. Prolonged annealing [4] and oxidation [12] can lead to thinning of the IGF. Creep led to a bimodal distribution of the IGF thicknesses [4] and has provided evidence to settle the long-standing discussion regarding squeezing out of intergranular amorphous material [14].

Understanding the evolution of these films as a function of temperature has important consequences, as these films have profound influence on the properties of the ceramic, at elevated service temperatures. The high-temperature quenching experiments of Clarke [15] and Cinibulk and coworker(s) [16,17] have provided detailed information on the thickness of these films at high temperatures in the region 1350-1650ºC. The results of Cinibulk et al. [16,17], wherein quenching from 1420ºC and 1500ºC led to anomalous thickness values, are surprising on one hand and somewhat confusing on the other.

In-situ heating experiments have proved to be an invaluable tool for the study of material behaviour with temperature [18]. In the case of IGFs, these types of experiments are expected to provide a direct access to the behaviour of these films as a function of temperature. The limitation in the case of in-situ heating experiments, applied to the study of IGFs, is that the maximum temperature obtainable, which is around 1000ºC, is far below the sintering temperature of ceramics like Si_3N_4 (~ 1800ºC).

It is conventionally thought that the kinetic processes are frozen below 1000ºC in Si_3N_4 [15,17] and hence little changes are expected to occur to IGFs. The observations of Clarke [15] and Cinibulk and Kleebe [17] correlate with this expectation. In the current work, in-situ heating experiments performed from room temperature (RT~24ºC) to 950ºC, on Lu-Mg doped Si_3N_4 in 400 kV and 120 kV microscopes. The choice of two different accelerating voltages is to study the effect of electron radiation (determined by the kV of the microscope), on the evolution of the IGF (if any). Lattice fringe imaging [19] is used in the 400kV microscope to measure the thickness of the IGF and in 120 kV microscope, Fresnel fringes are used. The Fresnel fringe techniques include: the method of extrapolation of the Fresnel fringe spacing [19,20], Fourier filtered zero-defocus images [21] and reconstruction of the imaginary part of the potential profile from zero-defocus images [22]. Multiple Fresnel techniques have been used for the determination of the thickness of the IGF to confirm the trends from the results obtained. This is essential due to errors inherent in the standard Fresnel extrapolation technique [21].

3.2 Procedures

3.2.1 Experimental

Dense silicon nitride samples have been prepared from milled and sieved α-Si_3N_4 (88.07 wt%), SiO_2 (2.16 wt%), MgO (1.07 wt%) and Lu_2O_3 (8.7 wt%) powders by first cold pressing, then sintering at 1750°C for 15 min at 10 bar pressure and finally hot isostatic pressing at 1750°C for 60 min at 100 bar as described by Satet and Hoffman [3]

Specimens for TEM experiments were prepared by the standard techniques of grinding, dimpling and ion-beam thinning (Precision Ion Polishing System, Gatan Inc.) with an angle of inclination of 8° of ion beam to the sample followed by coating with a thin layer of carbon to minimize charging under the electron beam.

In-situ heating was performed in two different microscopes (equipped with heating stages) which are operated at two different accelerating voltages. For these experiments boundaries of interest were tilted to orient them parallel to the incident electron beam.

The JEOL 4000 FX machine, operated at 400 kV, has a point to point resolution of 0.2 nm. Sample was heated in about 100 min, from room temperature (RT) to 950ºC(HT) and was kept at that temperature for 1 hr. Then the heating stage was switched off and the sample cooled to RT in about 5 min. Images were taken at RT , 650ºC, 950ºC (after 1 hr) and after cooling back to RT on Kodak electron image film (SO-163) at a magnification of 500000X.

The other microscope was the Zeiss-912 (LaB_6, Köhler illumination), operated at 120 kV and equipped with an in-column energy filter. Experiments were performed using an electron beam convergence semi- angle of 1 mrad.

For energy filtered images a 15 eV energy window, centered on the zero loss peak was selected. The images were captured onto a 1024×1024 pixel CCD array at a sampling density relative to the specimen of 0.19nm/pixel. A series of images (through focal series) were acquired in the defocus range of 1μm to 2.2 μm with a step size of 0.2 μm in both over and under focus conditions including the in-focus (zero-defocus) image. The zero-defocus condition was calibrated as accurately as possible. In this microscope the sample was heated in about 30 min from RT to HT and was kept at that temperature for about 1 hr and 15 min. Then the heating stage was switched off and the sample cooled down to RT in about 5 min. Images at a magnification of 80000X were taken before heating (at RT), at HT (10 min after reaching 950ºC) and after cooling to RT.

Digital micrograph software (Gatan Inc., Pleasanton, CA, USA) was used for image processing. The software was used to obtain the 1D intensity profiles across the image of the interface, from each the images recorded in Zeiss-912 and JEOL 4000 FX microscopes (integrated over a width of 100 pixels) and also for Fourier filtering of the images acquired in the Zeiss-912 miroscope.

3.2.2 Thickness measurement

Thicknesses from high resolution micrographs were measured using lattice fringe imaging [19].In the conventional Fresnel extrapolation method for measuring the thickness of IGFs, fringe spacing (s) values are plotted as a function of defocus (Δf) [20]. Jin et al. [23] used the following formula relating fringe spacing (W) to defocus (Δf):

$$W = W_0 + c\Delta f^{1/2} \tag{1}$$

Where, W_0 is the IGF thickness and 'c' is a microscope dependent constant.

This formula implies a linear plot of s versus root Δf and extrapolation to zero-defocus would give the thickness of the IGF. Investigations on Lu-Mg doped Si_3N_4 have shown the limitations of this approach for the calculation of the thickness of the IGF [21]. An alternative for better utilization of the fringe spacing data, is to plot the peak to peak distance in overfocus range and Fourier filtered zero to zero distance in underfocus range; as a function of Δf. This method is seen to yield a better estimate of the thickness of the IGF, from the same set of Fresnel data [21].

To obtain the thickness of an IGF from zero-defocus images, the image is first Fourier transformed and then a mask (diffuse mask with d_{FWHM}=0.2496 $Å^{-1}$) [21] is applied on the central spot. The unmasked area is inverse Fourier transformed to real space, where the distance between the points of zero intensity (zero to zero distance), is measured on the 1D intensity profile across the interface (integrated over a width of 100 pixels). This distance is seen to correspond to the thickness of the IGF [21].

The imaginary part of the scattering potential profile, obtained from zero-defocus and zero energy loss filtered images is additionally used for measuring the thickness of an IGF. The outline of the method is described next and details will be published elsewhere [24]. In the electron microscope the intensity of an image is given as $I(r) = \left|\psi(r) \otimes \mathrm{MTF}(\vec{r})\right|^2$; where, $\Psi_{(r)}$ is the complex-valued electron wave function at the bottom side (exit-face) of the sample. Within the phase object approximation the exit-face wave function is given by:

$$\Psi(\vec{r}) = \exp\left[i\sigma t \mathrm{V}(\vec{r})\right] = \exp\left(i\sigma t\left[V'(r) + iV''(r)\right]\right) \tag{2}$$

where σ is the electron-specimen interaction constant, V(r) the (complex) projected scattering potential, t the specimen thickness and MTF(r) the microscopic transfer function. The real part of the scattering potential (V'(r)) is due to elastic interaction of the electron with the specimen and the imaginary part (V"(r)) describes the loss of electrons from the elastic channel (and thus the zero energy filtered image), due to inelastic scattering events. I(r) is a one-dimensional intensity profile across an experimental image of the IGF. For zero-defocus imaging (and the assumed ideal aberration free imaging conditions; which is expected to hold good for the low-resolution conditions in the present work) the following can be set:

$$FT\left[MTF(\vec{r})\right] = mtf(\vec{q}) = \begin{cases} 1, |\vec{q}| \le q_{aperture} \\ 0, |\vec{q}| > q_{aperture} \end{cases} \tag{3}$$

Equation (3) describes a circular top-hat aperture function with a reciprocal-space radius of $q_{aperture}$. Ignoring coherent aberrations and envelope functions related to chromatic aberration, partial spatial coherence and microscope instabilities; the following equation is obtained under zero-defocus conditions:

$$\begin{aligned}\mathrm{I}(r) &= \left| \exp\left[-\sigma \cdot t \cdot V''(\vec{r})\right] \cdot \left\{ 1 - \int_{q_{aperture}}^{\infty} \left| FT\left\{ \exp\left[i\sigma t V'(\vec{r}\,')\right]_{\vec{r}\,'\approx\vec{r}} \right\}(\vec{q}) \right|^2 d^2q \right\} \right|^2 \\ &= \left| \exp\left[-\sigma \cdot t \cdot \left\{ V''(\vec{r}) + V'''(\vec{r}) \right\}\right] \right|^2 \end{aligned} \tag{4}$$

where,

$$\sigma t V'''\left(\vec{r}, q_{aperture}\right) = -\ln\left[\int_{0}^{q_{aperture}} \left| FT\left\{ \exp\left[i\sigma t V'(\vec{r}\,')\right]_{\vec{r}\,'\approx\vec{r}} \right\}(\vec{q}) \right|^2 d^2q \right] \tag{5}$$

is a specimen and objective aperture dependent ‘pseudo-absorptive’ scattering potential. Both the inelastic scattering described by V´´(r) and the pseudo-absorptive by V´´´(r) increase with the atomic number (Z) of the scattering element. In fact, the high-angle annular dark-field scanning transmission electron microscopy (HAADF STEM) technique, being mainly based on V´´´(r), is also called Z-contrast STEM for this reason. Hence, sum of both the terms will be referred to as the ‘absorptive potential’ (V_{abs}(r) = V´´(r) + V´´´(r)) from here on. The Fresnel contrast due to variations in the electrostatic potential V´(r, $q<q_{aperture}$) across the IGF vanishes at zero-defocus so that:

$$\sigma \cdot t \cdot \left\{ V''(\vec{r}) + V'''(\vec{r}) \right\} = -\ln\sqrt{I(r)} = -\frac{1}{2}\ln\left[I(\vec{r}) \right] \tag{6}$$

Taking t and σ to be constant, the LHS is representative of the inelastic and high-angle scattering and thus the concentration of heavy elements at position $\vec{r}$. The FWHM of a profile of absorptive potential across the IGF gives a measure of its chemical thickness. The resolution of this method is limited by the size of objective aperture which in the current study was 8 Å. MATLAB R12 software was used for implementing the algorithm to determine the imaginary part of the potential profile across the interface from zero-defocus images.

3.3 Results

The results of the heating experiment in the 400 kV JEOL microscope using lattice fringe imaging is presented first, followed by the Fresnel analyses of the data from the 120 kV Zeiss-912 microscope.

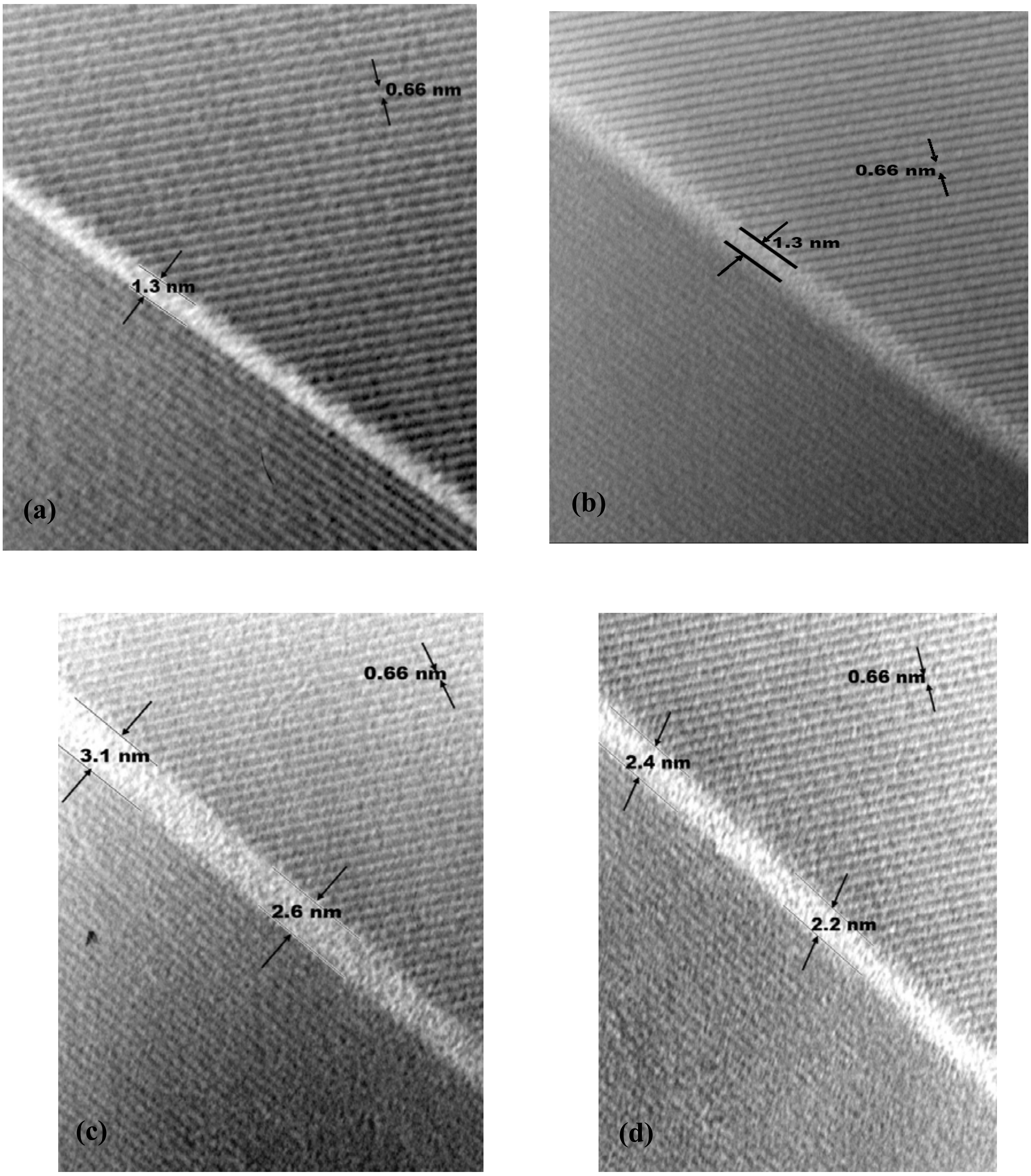

Fig. 3.1 High resolution micrographs (HRM) showing a comparison of the thickness of the IGF, during the stages of the heating cycle: (a) Room Temperature (RT= 24ºC), (b) 650ºC (c) 950ºC (d) cooled to RT. Lattice fringes seen in both of the grains are {100} planes according to [25]

Fig. 3.1 shows high-resolution micrographs from the sample at various stages of in-situ heating experiment. The thickness of the IGF follows the plot shown in Fig. 3.2. The times at which the measurements were taken are also shown in Fig. 3.2. It is seen that there is no change in the thickness of the film up to 650ºC. The thickness of the film increases to 2.6-3.1 nm on heating to 950ºC. On cooling back to room temperature the film thickness reduces to

2.2-2.4 nm. As seen in Fig. 3.1, the range of values of the thickness of the IGF at high temperature and in the cooled condition is due to the variation of the thickness along the IGF.

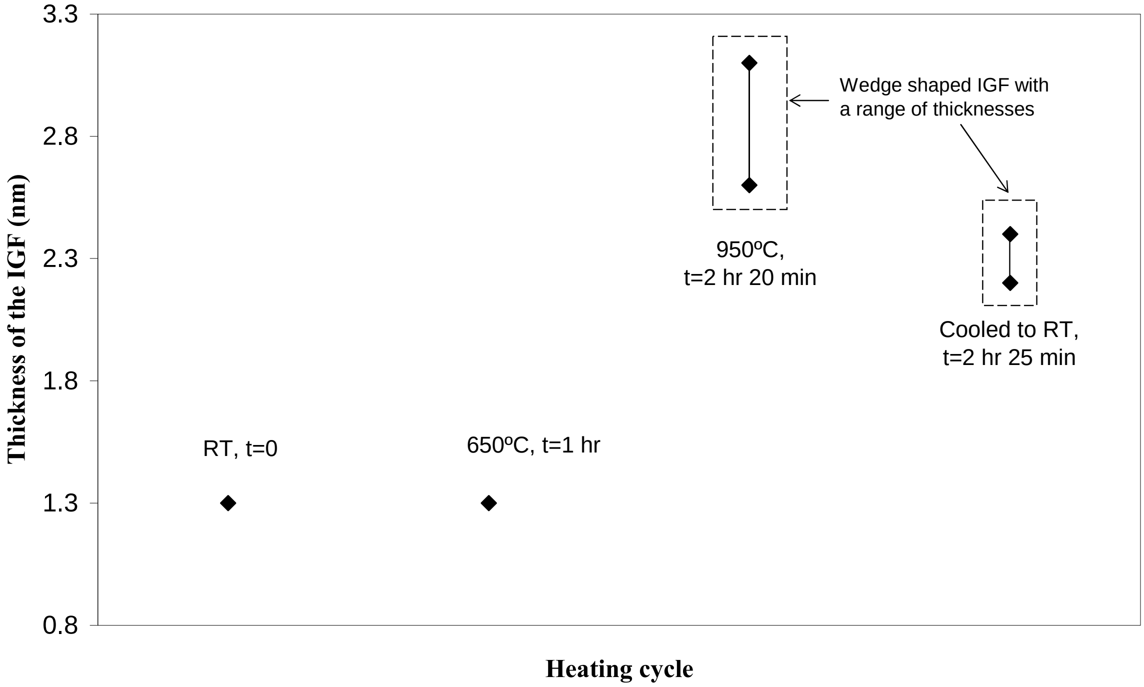

Fig. 3.2 Schematic showing the changes in the thickness of the IGF during heating, as seen from HRM.

Fig. 3.3a,b show the underfocus (-1 nm) and overfocus (1 nm) Fourier filtered Fresnel contrast images (FF-FCI), obtained from a grain boundary at room temperature at an accelerating voltage of 120kV (Zeiss-912 TEM). Since heating changes the equilibrium thickness of the grain boundary (Fig. 3.1) we had to use a new TEM sample of the same material for the experiment in Zeiss 912**.** The inset in these figures (Fig. 3.3a,b) shows the plot of the intensity profile across the image of the GB, which is used for the measurement of fringe spacing. Fig. 3.4 shows the plot of the fringe spacing data obtained at RT, 950ºC and from the sample cooled to RT, as a function of the root of the defocus. The plot is generated using the zero to zero distance from the FF-FCI in the underfocus condition and the peak to peak (PP) distance in the overfocus FCI. The thickness of the IGF is obtained by extrapolation of the Fresnel through focal series spacing data to a zero-defocus value. Usually, the extrapolations in the underfocus and overfocus lead to different thickness values and the average is taken to represent the thickness of the IGF; difference between the average value and either of the extreme (thicknesses obtained for overfocus and underfocus regions) is taken as the error in the measured thickness. It is noted from the figure (Fig. 3.4) that disparity is especially pronounced for the data from the specimen cooled to RT. The thicknesses obtained are: 0.8 nm (RT), 1.0 nm (950ºC) and 2.1 nm (cooled to RT).

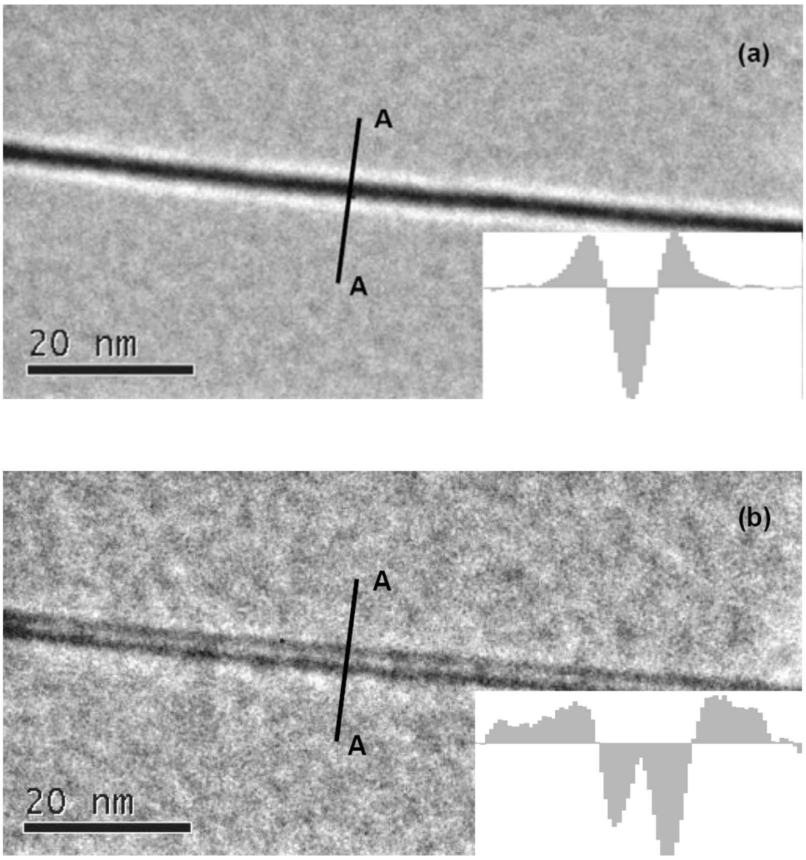

Fig. 3.3 Fourier filtered Fresnel contrast images (FF-FCI) of a grain boundary region at RT: (a) underfocus of 1 nm, (b) overfocus of 1 nm. Inset in (a) and (b) show the plot of the profile across the image of the GB (AA), integrated over a width of 18.8 nm; which is used for measurement of the fringe spacing.

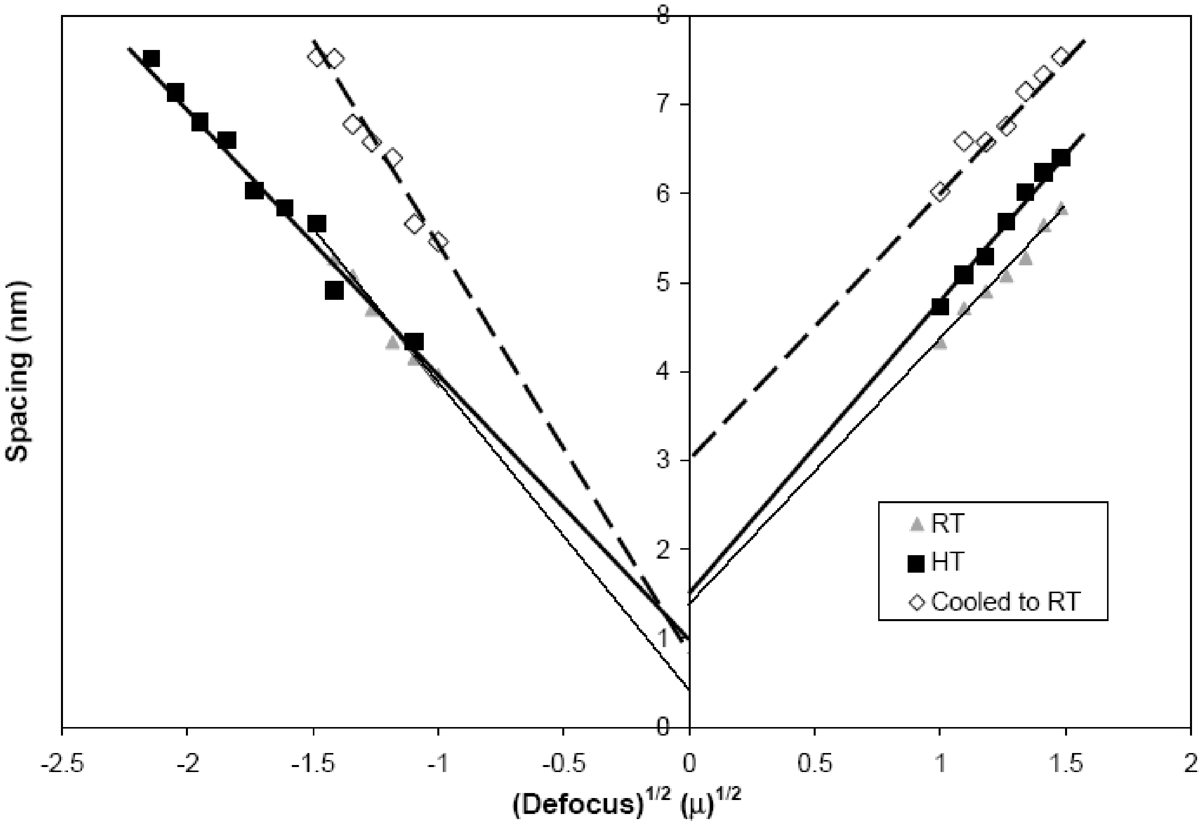

Fig. 3.4 Extrapolation of the Fresnel through focal series fringe spacing data to obtain the thickness of the IGF: (▲) RT, (■) 950ºC & (◇) cooled to RT (IGF thickness values and error bars are listed in Table 1).

The series of images in Fig. 3.5a-c show the FF-FCI taken at zero-defocus at various stages of the heating cycle. The zero to zero distance (ZZ), measured from the corresponding plot of profiles across the GB (shown as inset to the figures), gives the thickness of the IGF at the different stages of the heating cycle. The thicknesses measured using this technique are: 2.3 nm (RT), 2.5 nm (950ºC) and 3.2 nm (cooled to RT).

The absorptive potential profile (V′′(r)+V′′′(r)) from a zero-defocus image, is shown in Fig. 3.6. The FWHM measured from the plots gives a measure of the thickness of the IGF. The thicknesses obtained by this method are: 1.8 nm (RT), 2.1 nm (950ºC) and 3.0 nm (cooled to RT).

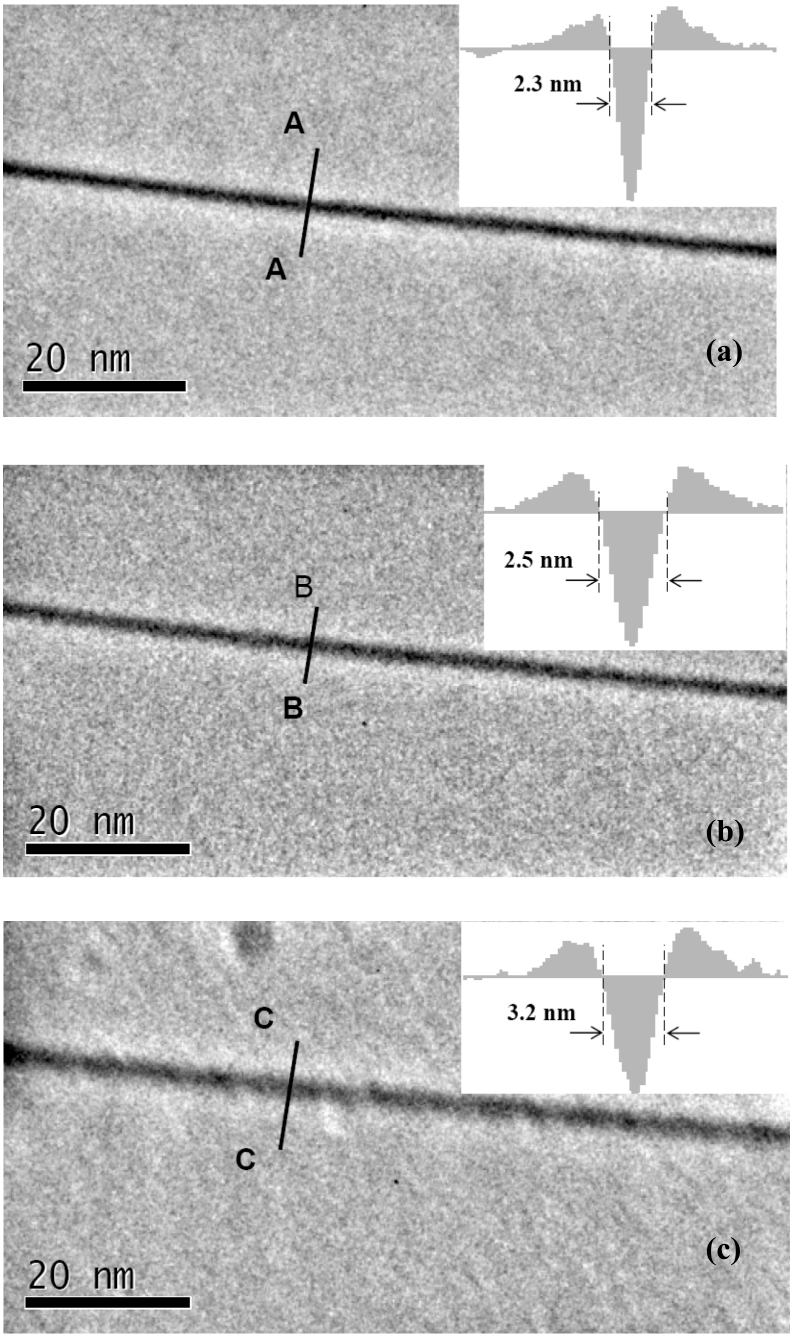

Fig. 3.5 FF-FCI taken at zero-defocus: (a) RT, (b) 950ºC, (c) cooled to RT. The insets in the figures show the profile across the GB (AA, BB & CC respectively), integrated over a width of 18.8 nm. The thickness of the IGF, measured as the zero to zero (ZZ) distance in the profile are marked in the inset figures.

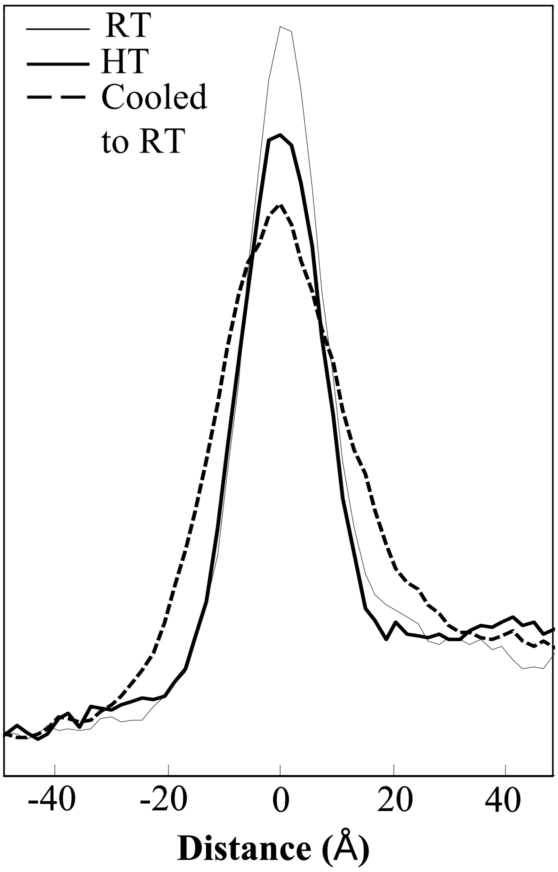

Fig. 3.6 Comparison of exit wave reconstructed profiles, of the imaginary part of the inner potential, using zero-defocus Fresnel fringe images: (–) RT, (**—**) 950ºC, (--) cooled to RT. The FWHM measured from the profiles gives a measure of the thickness of the IGF.

A compilation of the thickness obtained by the Fresnel techniques and high-resolution microscopy is shown in Table 1. To make a meaningful comparison of the different thicknesses obtained, the following points must be kept in mind,: (i) the resolution of the two microscopes used for the experiment are not the same, (ii) the resolution of the different Fresnel fringe techniques used for measuring the thickness are different, (iii) the high-resolution and Fresnel fringe techniques are expected to be sensitive to different aspect of the IGF structure and composition (e.g. the high-resolution method is expected to capture 'crystallinity' of the IGF, mainly being determined by the width of the core (of the possibly diffuse IGF structural profile); while, the Fresnel techniques are expected to capture the FWHM of the scattering potential profile), (iv) the dwell time at high temperature and heating/cooling rates are different for the experiments in the two microscopes.

Temperature	**High-resolution** (400 kV microscope)	**Fresnel fringes** (120 kV microscope)		
	HRt (nm)	**Extrapolation Ft (nm)**	**From zero-defocus image (Fourier filtered) (nm)**	**By zero-defocus Fresnel reconstruction (FWHM, nm)**
(Error bar ⇨)	*±0.1*	-	*±0.2*	*±0.2*
Room Temperature (24ºC)	1.3	0.8 *±0.5*	2.3	1.8
650ºC	1.3	-	-	-
950ºC	2.6 - 3.1*	1.0 *±0.1*	2.5**	2.1**
Cooled to 24ºC	2.2 – 2.4	2.1*±1.2*	3.2	3.0

Table 3.1 A comparison of the values of thickness obtained by HREM and Fresnel fringe extrapolation technique during the heating cycle. * ⇒ micrograph was taken 1 hr 10 min after reaching 950ºC; ** ⇒ micrograph was taken 15 min after reaching 950ºC.

From the compilation of the results (Table 1) it is seen that the trend observed is similar amongst the different Fresnel fringe techniques. However, there is considerable disparity in the actual values measured. It is also observed, that the trend in the thickness values obtained using Fresnel fringe techniques, correlates with the high resolution measurements at RT and HT but not in the sample cooled to RT.

3.4 Discussion

The results obtained in the present investigations are rather surprising in the light of the conventional line of thinking seen in the literature. Changes to IGFs are expected to occur at temperatures above 1200ºC as observed in the quenching experiments of Cinibulk and Kleebe [17] (henceforth referred to as CK).

The answer to the question: "the equilibrium configuration of the IGF is representative of which temperature?" is still not clear yet. It is usually assumed that the equilibrium film forms at the sintering temperature, especially in the case of quenched samples. IGFs have often been regarded as films due to partial wetting or as prewetting films [26,9]. They have also been described as graded multilayer adsorbates [27,28]. In such a framework of description the thickness of the film should decrease with decreasing temperature. Increasing the temperature, on the other hand, may lead to complete wetting as well. It may therefore be concluded, that heating to any temperature lower than the sintering temperature, should lead to thinning of the IGF in the light of wetting theories; if this is kinetically permissible. This thinning of IGF has been observed in prolonged annealing experiments [4]. However, in terms of the enhanced kinetics at the GB, the striking similarity to premelting/prewetting phenomena observed in segregation in metallic systems, is to be noted [29,30]. In systems like Cu-Bi, enhanced GB diffusivity is observed due to prewetting of GBs by a liquid like layer [31].

The results of the present annealing experiments are different from the quenching experiments of CK, wherein they observe an increase in thickness with increasing quenching temperature (except for samples quenched from 1420ºC and 1500ºC). Keeping in mind differences in sample composition and the heat treatments, we will try to compare the results of the current studies with the experiments of CK. The major differences between the current experiments and those of CK are: (i) Samples used by CK did not include Lu_2O_3, (ii) The thickness of the samples that CK used for quenching was about 100 μm (iii) temperature range sampled by CK was greater than in the present study.

Due to the inherent limitation in the precision of the Fresnel fringe extrapolation method [32], the thickness measured from the high-resolution micrographs (HRt), can be compared with the thickness measured by the Fresnel extrapolation method (Ft) only approximately and trends during the heating cycle rather than absolute values need to be observed. An increase in thickness at high temperature is observed using both methods. However, a significant difference is seen in the thickness measured on cooling to RT. On the other hand the trends observed by the different Fresnel fringe techniques are similar. Hence, from now on the HRt will be used for making quantitative comparison. One important difference between the experiments in two different microscopes is the dwell time before the HT micrographs were recorded. In the high-resolution microscope, the HRM was taken 70 min after reaching 950ºC (to allow for drift to stop), while in the Zeiss microscope the picture was taken after 15 min. Hence, it is conceivable that complete equilibrium may not have been attained at the HT in the Zeiss microscope, as reflected in the thicknesses measured by the Fresnel methods.

From the results obtained using the JEOL 4000FX microscope, it is seen that there is a tendency to restore the film thickness to a lower value than that at 950ºC, in spite of the fast cooling rate. The TEM heating stage temperature decreased from 950ºC to room temperature in about 5 min and had reached 650ºC, the temperature below which thickness changes are expected to be negligibly slow, in about 2 minutes. This implies that material transport processes may be rather fast even at temperatures well below 1000ºC.

The observation of such dramatically fast processes, occurring at temperatures less than half the sintering temperature, may on the one hand question the exact value of the temperatures that CK's quenched samples were representative of; but more importantly, suggests effects inherent to the particular experimental setup used in this study to be non-negligible.

For the interpretation of the experimental results of the present investigation, the following possible influences have to be kept in mind:

(i) Electron radiation damage.

(ii) Thin specimen effects (0.01μm in our specimen vs. 100μm in CK's experiment).

  (a) Short diffusion paths to the nearest surface

  (b) Less mechanical constraints due to lack of interlocking grains.

  (c) Stress on the IGF may be large due to small cross-sectional area

(iii) Stresses due to thermal gradients in the sample during heating.

The effect of electron radiation may be ruled out by the argument that the observed trends were independent of electron beam accelerating voltage. Additionally, in the Zeiss-912 instrument, operating at a comparatively low 120kV, the sample was not exposed to the electron beam for most of the heating cycle ('beam-blanker' was used for this purpose). It was only directed on the sample for the very short time, during recording of the images. In fact, after recording the first set of images (15 min after reaching 950°C), the next image was taken after the sample had cooled back to RT; in-between which, most of the changes in film thickness have occurred.

The thin TEM specimen affects the experiment in different ways. The part of the specimen investigated by TEM is usually near the edge and is free to move not only in the direction normal to the plane of the specimen, but also along inward radial direction. The proximity of free surfaces can act like a source or a sink for the material from the IGF and hence, the kinetics of processes like alteration of IGF width, may be enhanced. Additionally, thin specimen implies that the load on the grains has to be borne by an IGF material having a small cross-sectional area and hence stress concentration might be high. This can even lead to stress enhanced transport of material.

The argument of very fast diffusion processes being possible in such extremely thin specimen implies the observed IGF widths at elevated temperature to be equilibrium values. In light of no experimental evidence in literature for comparatively wide films and dramatic changes with temperature in bulk specimen annealed for much longer times (including the CK experiments), this seems rather implausible. The fact that the IGF thickness is not constant along the grain boundary strongly questions whether the amorphous layer is in any equilibrium state at all.

The third source of experimental artifact (as compared to a bulk specimen) seems the most plausible one. TEM samples of Si_3N_4 material having undergone tensile stress experiments revealed anisotropy in the distribution of IGF widths in the sample [4]. Films normal to the direction of external (tensile) force had widened to about 3nm; while those parallel to it remained at 1-1.5nm. In the absence of any external force acting on the specimen, stress induced by thermal gradients present in the sample, maybe playing a major role in producing the effects observed.

The geometry of the TEM specimen is sketched in Fig 3.7a. For simplicity of argument we assume a constant thickness gradient defined by the wedge angle θ_w = asin(dt/dr); where, 't' is the thickness and 'r' is along the radial direction. The heat is transferred to the specimen by conduction along the outer rim of the disc. The heat flow to the center of the specimen is limited by the heat conductivity through the ceramic. The heat conductivity of Si_3N_4 is 40 $Wm^{-1}K^{-1}$ and given that the specimen is very thin (i.e. a very small cross-sectional area / surface area ratio), we expect significant temperature gradients to be necessary for allowing enough heat to flow towards the center of the sample, in order to keep up with the heat loss due to radiation. The steady-state at which heat supply by conduction (Q_{in})equals the heat loss by radiation of the surfaces (Q_{out})is described by the following equation:

$$Q_{in}(r) = \int_0^r Q_{out}(r')dr' \tag{7}$$

Equation (7) implies that the amount of radial heat flow passing through a ring in the specimen of radius 'r', needs to be equal to the total heat flow through the top and bottom surfaces of this ring by radiation. Plugging in the correct terms for describing the circular geometry of the sample, a wedge angle θ_w and assuming the validity of the Stefan-Boltzman law ($Q_{out} = A\sigma(T^4 - T_{RT}^4)$), (Where, $\sigma = 5.67 \cdot 10^{-8}$ $Wm^{-2}K^{-4}$, A=area, T=temperature & T_{RT}=temperature of microscope specimen chamber) for the radiative heat loss, we obtain the following expression for the radial temperature gradient:

$$\frac{\partial T}{\partial r}(r) = \frac{2\sigma}{K\sin(\theta_w)r(r - r_{hole})}\int_{r_{hole}}^{r} r'[T^4(r') - T_{RT}^4]dr' \qquad (8)$$

This equation may be evaluated using standard numerical methods. Fig 3.7b shows the variation of the gradient with wedge angle, for a value of 'r' corresponding to typical distances from the specimen edge and a heat conductivity of 40 $Wm^{-1}K^{-1}$ (=K). For the conditions mentioned above, this gradient is not very sensitive to the radius of the specimen, but remains almost constant across the size of a standard TEM specimen. The temperature gradient is large for small wedge angles and smaller for larger angles, as expected. Assuming a thermal expansion coefficient of $3.5 \cdot 10^{-6}$ K^{-1}, the temperature gradient may be translated into thermally induced strain as shown on the right vertical axis in the plot (Fig. 3.7b). The unit of strain has been adjusted to correspond to the typical microstructure observed in these ceramics (TEM image in background of plot). Assuming that the Si_3N_4 grains have a thermal expansion coefficient much smaller than that of the glass and that all the thermally induced strain has to be compensated by redistribution of glassy material; a strain of 8Å/µm would imply that the IGFs linking a chain of 1µm wide grains would widen by 8Å each.

Since the specimen thickness along the electron beam was below 100 nm a mechanism similar to the one depicted in the Fig. 3.7c (stretching of IGF) may be able to explain the apparent mass flow within the IGF.

In reality, effects of the microstructure of the ceramic are much more complicated than the assumptions made in the above discussion. Some grains may therefore also be forced to rotate with respect to one another, potentially leading to IGF configurations of non-constant width, as seen in this work. The local stresses produced in this way are expected to compound with the dispersion and steric forces envisaged in Clarke's model [6]. A ceramic sample having relaxed all tensile stresses produced during heating, will be under compressive strain when cooling down again.

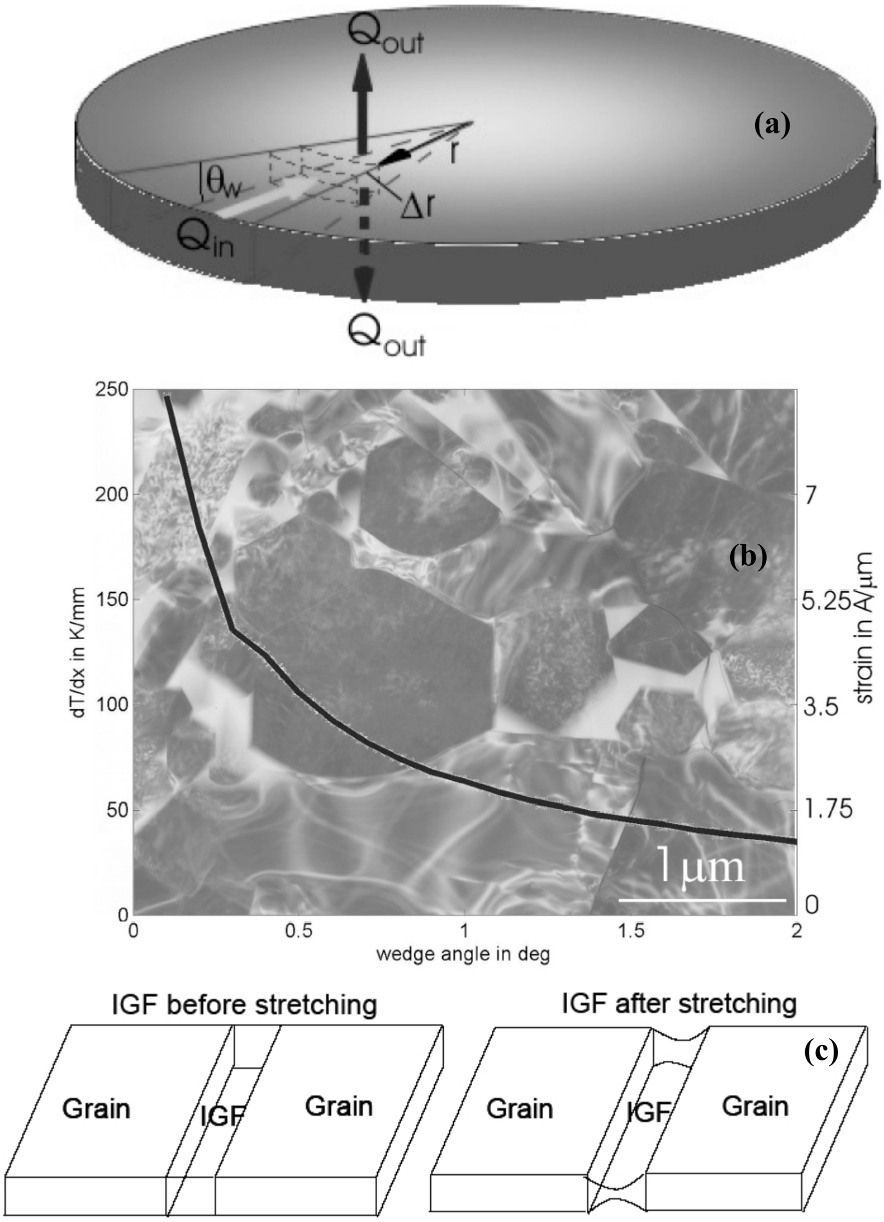

Fig. 3.7 (a) Sketch of the geometry of the central part of a dimpled TEM sample. The center of the disc has been thinned to perforation. The specimen thickness is assumed to increase linear with the radius. Heat is supplied to the specimen center by conduction from the perimeter and is lost predominantly by radiation to the TEM specimen chamber which is either at room temperature or cooled to approx. 100K. (b) Radial strain in the sample as function of wedge angle. The background of the plot shows a TEM micrograph representative of the microstructure of the Si_3N_4 ceramic. (c) Schematics to show the apparent mass flow within the IGF while stretching.

The new thickness could therefore be representative of a new equilibrium at the higher temperature or one of the twisted interface configurations shown schematically in Fig. 3.8. A combination of the three possibilities shown in Fig. 3.8 can also be envisaged. It should be noted that Fig. 3.8c is expected to be strongly influenced by the thin specimen used in a TEM. In the current experiment, soon after reaching 950ºC the configuration seemed to be a combination of that shown in Fig. 3.8a and Fig. 3.8c, with lattice fringes penetrating into the IGF. On waiting for half an hour (when the micrograph in Fig. 1c was taken), complete equilibrium still seemed not to have been attained; with variation in thickness along the length of the IGF. This kind of configuration, additionally gives a good explanation of the thicknesses measured by the Fresnel techniques on cooling to RT.

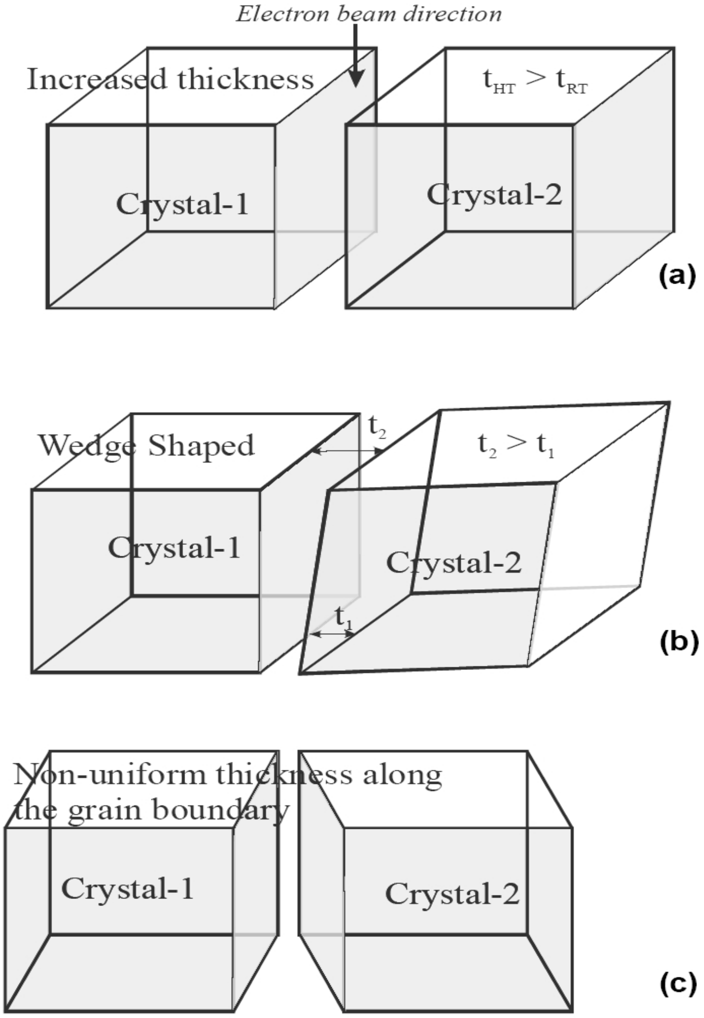

Fig. 3.8 Schematic representation of the possible high-temperature configurations of a grain boundary with an IGF: (a) increased thickness, (b) wedge shaped, (c) non-uniform thickness along the GB (wedge with different orientation). Though (b) and (c) represent similar cases they are differentiated based either on crystallography or/and proximity to a free surface.

The above mentioned effect of specimen geometry offsetting intergranular forces makes a direct comparison of the present work with experiments on bulk specimen difficult. However, the obvious accessibility of the current experimental conditions to observe fast material transport processes in these materials, opens up a whole range of new possible experiments to study diffusion kinetics, viscosity of the amorphous phase, chemical composition of the IGF at different film widths, etc.

To reiterate, it is difficult to comprehend the results of the current work using the conventional line of thinking. The fracture experiments of Satet and Hoffmann [3], wherein they observe intergranular fracture, leads one to postulate that there must be a weak plane in the IGF, which debonds during fracture. In the absence of the weak plane, given the comparable strength of the bulk glass and the Si_3N_4 ceramic, the crack would propagate in a transgranular mode. Motivated by these observations, it is conceivable that there is a 'core' region in the IGF, wherein material transport processes are vastly different from the bulk glass.

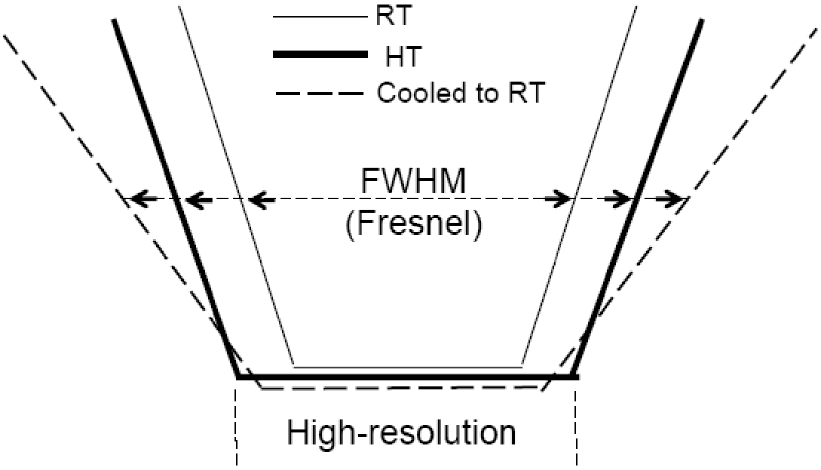

Fig. 3.9 Summary of the experimental results in the light of the discussions, taking into account the various factors affecting the thickness and profile of the IGF. The potential profiles during the different stages of the heating cycle are represented schematically.

3.5 Summary and conclusions

Keeping the various points brought out in the discussion in mind, the TEM observations of this work can be summarized as in Fig. 3.9. The Fresnel methods seem to capture the FWHM of the potential profile, while the HRt is representative of the core potential. The following conclusions can be drawn from the present investigations:

(i) Fast changes to IGF thickness (in Lu-Mg doped Si_3N_4) can occur at comparatively low temperatures (<1000ºC) under low irradiation doses, with electron beam energies as low as 120 keV.

(ii) The tendency of the IGFs to regain the width they had before annealing has been observed. However, the relaxation times were not long enough to observe complete reversibility of the changes in IGF width.

(iii) A tensile-compressive straining cycle may be realized by heating and cooling the sample due to thermal gradients in the TEM sample, as a result of its special geometry.

(iv) Although local stress vectors, induced by thermal gradients in the sample, may offset the forces determining the IGF equilibrium width in the force balance model, dynamic observations (e.g. video recording) of the kinetics of the relaxation process may give insight into details of diffusion processes and the viscosity of the intergranular glassy phase.

3.6 References

[1] H.-J. Kleebe, J. Ceram. Soc. Jpn. 105 (1997) 453.

[2] J. S. Vetrano, H.-J. Kleebe, E. Hampp, M.J. Hoffmann, M. Rühle, R.M. Cannon, J. Mater. Sci. 28 (1993) 3529.

[3] R.L. Satet, M.J. Hoffmann, Key Engg. Mater. 264-268 (2004) 775.

[4] Q. Jin, D.S. Wilkinson, G.C. Weatherly, W.E. Luecke, S.M. Wiederhorn, J. Am. Ceram. Soc. 84 (2001) 1296.

[5] Y.W. Kim, S.H. Kim, M. Mitomo, T. Nishimura, Key Engg. Mater. 247 (2003) 267.

[6] D. R. Clarke, J. Am. Ceram. Soc. 70 (1987) 15.

[7] M. Bobeth, D. R. Clarke, W. Pompe, J. Am. Ceram. Soc., 82 (1999) 1537.

[8] C.M. Bishop, Continuum models for intergranular films in silicon nitride and comparison to atomistic simulations, Ph.D. Thesis, Massachusetts Institute of Technology, Boston, 2003.

[9] I. Tanaka, J. Ceram. Soc. Jpn., 109 (2001) S127.

[10] R. M. Cannon, L. Esposito, Z. Metallkd., 90 (1999) 1002.

[11] H. Wang, Y.M. Chiang, J. Am. Ceram. Soc. 81 (1998) 89.

[12] M.K. Cinibulk, H.J. Kleebe, J. Mater. Sci, 28 (1993) 5775.

[13] C.M. Wang, M. Mitomo, T. Nishimura, Y. Bando, J. Am. Ceram. Soc. 80 (1997) 1213.

[14] F.F. Lange, J. Am. Ceram. Soc. 65 (1982) C-23.

[15] D.R. Clarke, J. Am. Ceram. Soc. 72 (1989) 1604.

[16] M.K. Cinibulk, H.J. Kleebe, G.A. Schneider and M. Rühle, J. Am. Ceram. Soc. 76 (1993) 2801.

[17] M.K. Cinibulk, H.J. Kleebe, Ceramic Microstructure: Control at the Atomic Level, ed. A. P. Tomsia and A. Glaeser, Plenum Press, New York, (1998) pp. 123.

[18] Y. Ikuhara, J.Ceram. Soc. Japan 110 (2002) 139.

[19] D.R. Clarke, Ultramicroscopy 4 (1979) 33.

[20] M.K. Cinibulk, H.-J. Kleebe, M. Rühle, J. Am. Ceram. Soc 76[2] (1993) 426.

---

[21] Somnath Bhattacharyya, Anandh Subramaniam, C.T. Koch, M. Rühle, J. Microsc. (Oxf), accepted (Chapter 2).

[22] Somnath Bhattacharyya, C.T. Koch, M. Rühle, to be communicated.

[23] Q. Jin, D.S. Wilkinson, G.C. Weatherly, J. Eur. Ceram. Soc. 18 (1998) 2281.

[24] S. Bhattacharyya, Anandh Subramaniam, M. Rühle, to be communicated.

[25] EMS online <http://cimesg1.epfl.ch/CIOLS/crystal4.pl>

[26] R. M. Cannon and L. Esposito, Z. Metallkd., 90 (1999) 1002.

[27] R.M. Cannon, Structure-composition-stability relations in ceramic interfaces, talk at Max Planck Institute, Stuttgart, 2004.

[28] R.M. Cannon, M. Rühle, M.J. Hoffmann, R.H. French, H. Gu, A.P. Tomsia, E. Saiz, Mat. Sc. & Engg. A., accepted.

[29] B.B. Straumal, P. Zięba, W. Gust, Int. J. Inorg. Mater. 3 (2001) 1113.

[30] B. Straumal, B. Baretzky, Interface Sci. 12 (2004) 147.

[31] L.-S. Chang, E. Rabkin, B.B. Straumal, B. Barezky, W. Gust, Acta Mater. 15 (1999) 4041.

[32] D.B. Williams, C.B. Carter, Transmission Electron Microscopy, Plenum Press, New York, (1996) p.492-93,

CHAPTER 4

Projected potential profiles across interfaces obtained by reconstructing the exit face wave function from through focal series

S. Bhattacharyya, C. T. Koch and M. Rühle

Ultramicroscopy, submitted

Abstract

An iterative method for reconstructing the exit face wave function from a through focal series of TEM image line profiles across an interface is presented. Apart from high-resolution images recorded with small changes in defocus this method works also well for a large defocus range as used for Fresnel imaging. Using the phase-object approximation the projected electrostatic as well as the absorptive potential profiles across an interface are determined from this exit face wave function. A new experimental image alignment procedure was developed in order to align images with large relative defocus shift. The performance of this procedure is shown to be superior to other image alignment procedures existing in the literature. The reconstruction method is applied to both the simulated and the experimental images.

4.1 Introduction

Interfaces play an important role in material science. Intergranular glassy films in polycrystalline ceramics, quantum well layers in semiconductors, precipitate matrix interfaces etc. control many important mechanical, physical, chemical and electrical properties of the materials containing them. Charge defects are often accumulated at interfaces between two phases in electrically active systems. Such charge defects and consequently accumulated space charge clouds at the interface lead to spatially varying electrostatic potentials across them [1]. For metal-semiconductor interfaces, the potential profile gives rise to the formation of a Schottky barrier [2]. The formation of a particular specially shaped potential profile across GaAs devices is probably caused by charge trapping at the interface between the epitaxial layer and the substrate [3]. Potential profiles across intergranular glassy films in polycrystalline ceramics may provide information regarding structural and compositional changes across that grain boundary [4]. In general, potential profiles across interfaces can provide useful information about their structure, composition, density, ionicity of their constituents, the presence of space charge layers, etc. So determination of potential profiles across interfaces has great importance in the field of material science.

Transmission electron microscopy (TEM) techniques, based on phase contrast imaging, can determine local variations in electrostatic potential. Electrostatic potential variation and accumulated space charge across an interface produce phase shift of the transmitted electron beam wave function. Apart from off-axis holography, in which the phase of the transmitted wave function is measured by interference of a reference wave with microscope aberrations [1], such as defocus and spherical aberration may also be used to encode local variations in the phase of the exit face wave function in the image intensity. Stobbs and coworkers [5-7] developed an approach to use the Fresnel contrast (contrast in largely defocused images of objects containing local phase differences) to analyze potential profiles across interfaces by fitting a few parameter model of the mean inner potential profile to the fringe contrast. This approach was reviewed and extended further by Dunin-Borkoski [8]. According to this method, the line profiles across an interface from a series of experimental images with varying defocus are required. Using a least squares optimization routine, the interface width, its potential magnitude and the diffuseness of its boundaries are fitted to the experimental image intensity profiles by comparing them with simulated ones at every defocus for the entire experimental focal series. This procedure thus requires a global non-linear optimization problem to be solved, which is the reason for the low limit on the number of parameters that can be used to describe the potential profile.

Using the phase-object approximation (POA) electron holographic methods can be used to map the electrostatic potential of a given specimen and, as will be the focus of this work, across an interface [1]. In off-axis holography, which determines the phase of the scattered electrons by letting them interfere with a known reference wave requires the microscope to be equipped with a biprism. In this work we will report on the use of in-line holography, i.e. the reconstruction of the complex exit-face wave function from a Fresnel image series, to determine local variations in the mean inner potential of the scattering specimen.

In order to extract the contribution due to pure electric charge from a map of the projected specimen potential, the mean inner potential due to the local composition must be known. Because of the monotonic correlation of high-angle (Rutherford) scattering and atomic number (Z), annular dark field scanning transmission electron microscopy (ADF-STEM) has good sensitivity to local composition. We will show that in addition to the phase of the scattered electrons, information about local composition may be extracted from the focal series reconstruction of a zero-loss energy filtered Fresnel image series recorded with an objective aperture. This allows, in principle, space charge and composition contributions to the projected potential to be separated.

To retrieve the complex electron wave function from a focal series of experimental images, numerical phase retrieval methods must be applied. These methods reconstruct the wave function at the exit surface of the specimen. Various approaches exist in the literature to retrieve the exit-face wave function using images of varying defocus [9-15]. In one of the approaches, the wave function is reconstructed iteratively by projecting in different focal planes [12,13]. Vincent [14] modified the iterative approach, introducing conjugate gradient optimization for global convergence. The latest version of the iterative approach is the iterative wave function reconstruction (IWFR) method [15].

The IWFR algorithm was originally designed for reconstructing the exit face wave function using high-resolution images of a small defocus range. In this paper this algorithm is modified to reconstruct the exit face wave function using images of a large defocus range produced by a partially coherent electron beam in a medium resolution transmission electron microscope (TEM). Numerical instabilities in the IWFR algorithm due to the suppression of spatial frequencies by the spatial coherence envelope for large defoci, as well as the difficulty of aligning images of strongly different defocus made these modifications necessary. Because of the focus of this work on potential profiles across interfaces we limited ourselves to the one-dimensional case by performing the reconstruction on integrated line scans from experimental images recorded with different objective lens defocus.

Finally, the projected potential profile across the interface is derived from the reconstructed wave function using the phase-object approximation (POA)

$$\psi(r) = \exp\big(i\sigma t V(r)\big), \tag{1}$$

where the average projected potential V(r) (per unit thickness) may be complex σ is the electron interaction constant and t the specimen thickness. From here on the average projected potential profile will be referred as ‘potential profile’.

The real part of the reconstructed potential profile contains information regarding the phase shift, while its imaginary part is produced by inelastic and high-angle (scattering angle greater than objective aperture) scattering events and provides therefore chemical information. We will show that, when the information regarding the phase shift across an interface is scaled with respect to a reference phase (e.g. near the specimen edge, where vacuum may be used for reference), absolute mean inner potential values may be retrieved by this method.

The reconstruction method is tested for both simulated as well as for the experimental cases. To test it for experimental case, a specimen edge of an Al_2O_3 specimen, i.e. a vacuum-Al_2O_3 interface is used. Point to point resolution of the reconstruction method, in the framework of the present investigation, is also derived experimentally using a specimen containing a nominally abrupt Al-Al_2O_3 interface. Using simulated intensity profiles instead of experimental ones as input, the accuracy of the new image alignment and reconstruction procedure is demonstrated. A comparison of this new alignment procedure with other image alignment methods based on different correlation functions is also presented.

The limitations of the method are listed below:

- While the use of an objective aperture allows the high-angle scattering to be separated and the chemical information to be retrieved, it also limits the resolution. However, the use of the phase-object approximation for retrieving the projected potential is most valid for low spatial frequency information anyway.
- The electrostatic potential may only be retrieved across distances of the order of the coherence length of the incident electron beam.
- A large defocus range is necessary for retrieving low spatial frequency components of the electrostatic potential.
- Dynamic scattering effects are taken into account by the POA only in the zero wavelength and zero excitation error limit.

4.2. Reconstruction procedure

4.2.1 The phase retrieval algorithm

The iterative exit face wave function reconstruction algorithm, used in the present investigation, is a modified version of the work presented by Allen et. al.[15]. In addition to the new image drift correction method, the modifications also include the use of weighted averaging of the wave functions instead of an unweighted one.

The reciprocal space wave function at focal plane *n* may be obtained from the exit face wave function by multiplying it with the exponential of the phase distortion function $\exp[\chi(k,\Delta f_n)]$ [16] (*k* is the reciprocal space coordinate and Δf_n the defocus of image *n*) as well as the envelope functions related to temporal coherence($E_\Delta(k)$) and spatial coherence($E_s(k,\Delta f)$). Considering only symmetric lens aberrations up to third order, the above mentioned functions are given by

$$\chi(k,\Delta f) = \pi\lambda\Delta f k^2 + \frac{1}{2}\pi\lambda^3 C_s k^4 \tag{2}$$

$$E_\Delta(k) = \exp\left[-\frac{1}{4}\pi^2\Delta_f^2\lambda^2 k^4\right] \tag{3}$$

$$E_s(k,\Delta f) = \exp\left[-\pi^2\beta^2(k^2\Delta f^2 + 2\Delta f\lambda^2 C_s k^4 + \lambda^4 C_s{}^2 k^6)\right] \tag{4}$$

Here λ is the electron wavelength, Δf is the defocus spread and β represents the beam convergence semi angle. While propagating from image plane *n* back to the $\Delta f = 0$ plane we must divide the wave function by these terms in reciprocal space again (or, in real space, deconvolute by their Fourier transforms). The spatial coherence envelope $E_s(k,\Delta f)$ vanishes for large ranges of *k* at large defoci (for the present study the selected defocus range is; Δf = -4 μm … +4 μm), making division by this term numerically unstable. The IWFR algorithm only requires the computation of an average exit face wave function and not the individual back-propagated wave functions obtained from each focal plane. Numerical stability may therefore be gained by computing a weighted average of the wave functions, where more weight is given to those wave functions whose envelope function is large at a given spatial frequency *k*.

$$\psi^j_{avg}(k) = \frac{\sum_{n=1}^{N}\psi^j_{n,0}(k)\, w_n(k,\Delta f)}{\sum_{n=1}^{N} w_n(k,\Delta f)} \tag{5}$$

with $w_n(k,\Delta f) = E_s(k,\Delta f_n)\, E_\Delta(k)$. The original IWFR algorithm uses $w_n(k,\Delta f_n) \equiv 1$.

An outline of the modified algorithm is presented in Fig. 4.1 and described in detail below:

1. From a through focal series comprising N experimental images line profiles across the interface in each focal plane n (denoted by $I_n(r)$) are extracted. From prior work in literature [17], $N \geq 3$ should suffice for obtaining a unique result.
2. The complex electron wave function at focal plane n is given by:

   $$\Psi_n^j(r) = \sqrt{I_n(r)}\, e^{i\phi_n^j(r)} \tag{6}$$

   where j denotes the number of the iteration steps, r denotes the real space coordinate and $\phi_n^j(r)$ is the phase of the wave function. The algorithm starts with an initial guess of $\phi_n^1(r) = 0$, i.e. $\psi_n^1(r) = \sqrt{I_n(r)}$.
3. The wave function in each focal plane is propagated to the nominal exit surface plane ($\Delta f = 0$). This is done dividing the Fourier transform $\Psi_n^j(k)$ of $\Psi_n^j(r)$ by $\exp[i\chi(k,\Delta f_n)]E_s(k,\Delta f_n)\,E_\Delta(k)$ and multiplying it by the weighting factor $w_n(k,\Delta f_n) = E_s(k,\Delta f_n)\,E_\Delta(k)$, so that

   $$\psi_{n,0,w}^j(k) = \psi_n^j(k)\exp[-i\chi(k,\Delta f_n)] \tag{7}$$

   where, $\psi_{n,0,w}^j(k)$ is the wave function at $\Delta f = 0$ propagated from plane n weighted by the corresponding weighting function $w_n(k,\Delta f_n)$. So this can be expressed as $\psi_{n,0,w}^j(k) = \psi_{n,0}^j(k)\,w_n(k,\Delta f_n)$.
4. An new estimate of the exit face wave function is obtained by averaging over the individual back-propagated weighted wave functions $\psi_{n,0,w}^j(k)$ and renormalizing:

   $$\psi_{avg}^j(k) = \sum_{n=1}^{N}\psi_{n,0,w}^j(k) \Big/ \sum_{n=1}^{N} w_n(k,\Delta f_n) \tag{8}$$

5. The use of an objective aperture of radius $k_{aperture}$ limits the spatial resolution of the reconstruction to spatial frequencies within a circle defined by $k_{aperture}$. The division of $\psi_{avg}^j(k)$ by $\sum_{n=1}^{N} w_n(k,\Delta f_n)$ in the previous step amplifies spatial frequencies outside this range. The application of a sharp numerical aperture,

to limit the spatial frequency content of $\psi^j_{avg}(k)$, may introduce artifacts. So we decided to use a smooth aperture function $\exp\left[-(A|k|)^q\right]$ (i.e. multiply this function with $\psi^j_{avg}(k)$) to suppress the high frequency noise at $k \geq k_{aperture}$. The value of A is chosen to match the amplitude of the sum of the weighting functions at $k = k_{aperture}$, From $\exp\left[-(A|k|)^q\right] = \sum_{n=1}^{N} w_n(k, \Delta f_n)$ we obtain

$$A = \frac{1}{k_{aperture}} \sqrt[q]{-\ln\left[\frac{1}{N}\left(\sum_{n=1}^{N} w_i(k_{aperture})\right)\right]} \tag{9}$$

Fig. 4.2 shows plots of $\exp\left[-(A|k|)^q\right]$ for several values of q. The value of q should be chosen according to the noise level in the experimental data. Low values of q might be used for noisy data, while larger values may be used for less noisy data.

6. The averaged wave function in reciprocal space is propagated to each of the n image planes to obtain $\tilde{\psi}^j_n(k)$. The estimated wave functions are now given by:

$$\tilde{\psi}^j_n(k) = \psi^j_{avg}(k)\exp\left[i\chi(k,\Delta f)\right]E_s(k,\Delta f)E_\Delta(k) \tag{10}$$

7. The real space wave function is obtained by inverse Fourier transformation

$$\psi^j_n(r) = FT^{-1}(\tilde{\psi}^j_n(k)) \tag{11}$$

The phase of $\psi^j_n(r)$ is now used as the input phase for the next iteration beginning at step 2.

8. As in the original algorithm by Allen et al convergence is reached when $SSE^{j-1}_{avg} - SSE^j_{avg} < \xi$ for a chosen convergence criterion ξ, where

$$SSE^j_n = \frac{\sum\left[\sqrt{I_n(r)} - \left|\psi^j_n(r)\right|\right]^2}{\sum I_n(r)} \quad \text{and} \tag{12}$$

$$SSE^i_{avg} = \frac{1}{N}\sum_{n=1}^{N} SSE^j_n \tag{13}$$

The real space exit face wave function is now obtained by inverse Fourier transform

$$\psi(r) = FT^{-1}\left[\psi^{final\ step}_{avg}(k)\right] \tag{14}$$

The image drift correction incorporated into the algorithm is as follows:

The reconstruction starts with the normalized 1D experimental image intensity profiles across the same area of the interface with varying defocus. After completing a specified number of iteration steps (e.g. 1000), a region around the interface of the experimental profiles and reconstructed profiles is selected where maximum changes in image intensity with defocus occur (e.g. up to 50 Å on either side of the interface). Then the selected portions of all the profiles are smoothened by convoluting them with a Gaussian function.

$$A_n(J) = FT^{-1}\left[FT\left\{\sqrt{I_n(J)}\right\}\exp\left(-Bk^2\right)\right] \tag{15}$$

and

$$B_n(J) = FT^{-1}\left[FT\left\{\left|\psi_n^j(J)\right|\right\}\exp\left(-Bk^2\right)\right] \tag{16}$$

J denotes the selected region and B is a constant. Instead of aligning images with different defocus, each of the experimental (A_n) line profiles is now aligned with the corresponding simulated one (B_n) by minimizing

$$\chi_n^2 = \sum\left|B_n(J) - A_n(J+px)\right|^2 \tag{17}$$

where, px indicates the number of pixels that $A_n(J)$ is shifted with respect to the corresponding $B_n(J)$. After aligning all the experimental profiles, the aligned profiles are taken as input to step 1 of the reconstruction algorithm.

4.2.2 Retrieval of the projected potential

Retrieval of the projected potential from the exit face wave function is outlined in Fig. 4.1 and described in more detail here:

According to the phase-object approximation (POA) the exit face wave function produced by the scattering potential of the specimen can be described as

$$\psi(r) = e^{i\phi} \tag{18}$$

where

$$\phi = \sigma V(r)t \tag{19}$$

Here, *t* is the specimen thickness parallel to the beam direction, $V(r)$ is the (complex) projected scattering potential, and σ is the relativistic electron interaction constant given by [18]:

$$\sigma = \frac{2\pi}{\lambda}\frac{E_0 + E}{2E_0 + E}|e| \tag{20}$$

where, E_0 is the electron's rest energy, *E* is electron's kinetic energy and *e* is the charge of an electron.

For the reconstructed in-focus exit-face wave function, regions of vacuum within the image have the largest exit face wave function amplitude and may be used for normalization, so that ϕ may be obtained by

$$\phi = -i\ln\left(\frac{\psi(r)}{\max|\psi(r)|}\right) \tag{21}$$

If the imaged region contains no vacuum, this normalization makes at least sure that we will positive absorption everywhere, which is physically sensible. The information regarding the phase shift and the compositional changes across the interface may then only be interpreted in relation to a given location within the imaged region.

The specimen thickness along the direction of the electron beam can be determined using energy filtered TEM (EFTEM). Only two images, a zero-loss filtered one (I_0) and an unfiltered one (I_l), both recorded with the same exposure time, are needed for this purpose. Extracting line profiles from the same area of the images as that used in the focal series reconstruction, the local specimen thickness, t, is calculated according to [19]:

$$t = \lambda_{inel}\ln\left(\frac{I_l}{I_0}\right) \tag{22}$$

where, λ_{inel} is the inelastic mean free path (IMFP) of the electron in the given material that can be calculated as described by Egerton [19].

The projected potential $V(r)$, is now given by

$$V(r) = \frac{\phi}{\sigma\, t} \tag{23}$$

and may be split up into [20]

$$V(r) = V'(r) + i[V''(r) + V'''(r)] \tag{24}$$

where, potential $V'(r)$ is due to the elastic interaction of the electron with the specimen refereed to as the 'electrostatic potential', $V''(r)$ describes the loss of electrons due to inelastic scattering events involving electronic excitations and $V'''(r)$ describes the elastic (and quasi-elastic TDS) scattering outside the objective aperture which can be described as an objective aperture dependent 'pseudo-absorptive' scattering potential. The sum of both the terms $V''(r)$ and $V'''(r)$ will from now on be referred to as 'absorptive potential'

$$V_{abs}(r) = V''(r) + V'''(r) \tag{25}$$

In addition to enhancing Fresnel contrast, the objective aperture thus allows to extract high-angle scattering information from the experimental data.

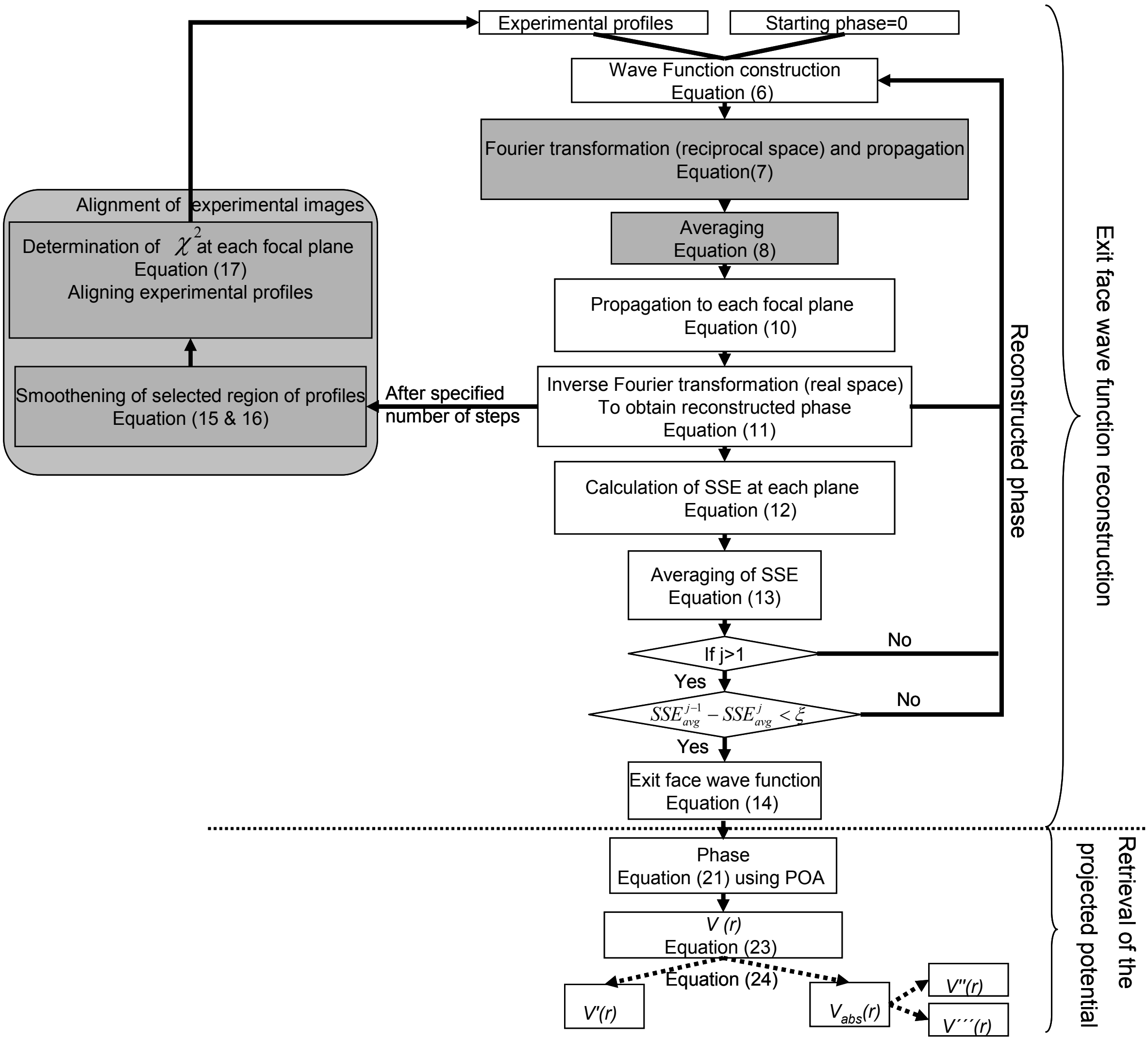

Fig. 4.1 Outline of the iterative exit face wave function reconstruction algorithm (shaded boxes indicate the modification to the IWFR algorithm) combined with the outline of the projected potential retrieval from a complex exit face wave function.

4.3 Application to simulated images

At first the reliability of the new alignment procedure was tested using 14 simulated images (at defocus values of 1 μm to 4 μm with a step size of 0.5 μm in both over and under focus directions) which had intentionally been misaligned. From the model potential profile shown in Fig. 4.3a, the exit face wave function was calculated using expression (1). A series of defocused images was calculated by forward propagation to different focal planes according to

$$\psi_n(r) = FT^{-1}\left\{FT(\psi(r))\exp[i\chi(k)]E_s(k,\Delta f)E_\Delta(k)\, f_{aperture}\right\} \tag{26}$$

where $f_{aperture}$ is the objective aperture function in reciprocal space. All other terms are the same as in section 2.1. All parameters used in the simulation are listed in Table. 1.

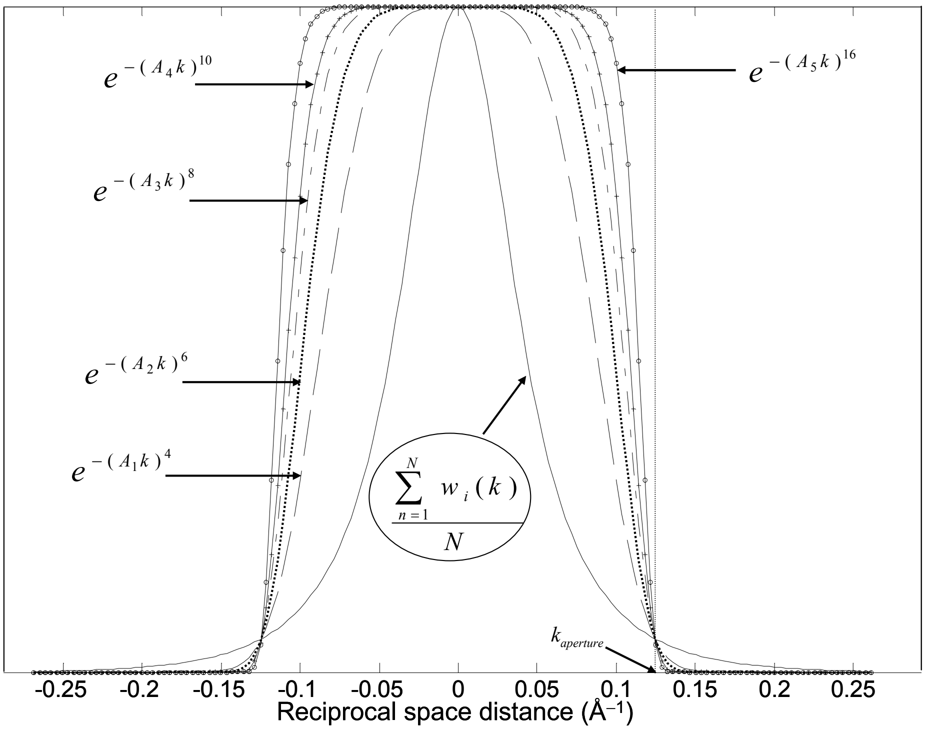

Fig. 4.2 Plots of the smoothening functions used in the averaging step (5) of the exit face wave function in reciprocal space. Values of A_1, A_2, A_3, A_4 and A_5 calculated using equation 6 are 10.55, 9.62, 9.19, 8.94 and 8.58 respectively.

Poisson noise was added to the image intensities using

$$\bar{I}_n(r) = I_n(r) + \frac{1}{\sqrt{N^{e^-}_{pixel}}}\sqrt{I_n(r)}\,G(r) \tag{27}$$

where, $\bar{I}_n(r)$ is the intensity including noise, $N^{e^-}_{pixel}$ is the mean number of electrons per pixel averaged over the relevant specimen area and G(r) are normally distributed random numbers with the mean being zero, variance one and standard deviation one.

In order to realistically simulate images recorded by CCD, point spread function of the slow scan CCD camera of the Zeiss 912 [21] was convoluted with $\bar{I}_n(r)$. Four simulated profiles at different defocus values with $N^{e^-}_{pixel} = 1000$ and without focus/image shift are shown in Fig. 4.3b.

Parameter	Value
Cell length	150 pixel
Sampling density	1.875 Å
Specimen thickness	30 nm
Accelerating voltage (V_0)	120 kV
Wavelength (λ)	0.0335 Å
Spherical aberration (C_s)	2.7 mm
Chromatic aberration (C_c)	2.7 mm
Beam convergence semi-angle (β)	0.25 mrad
Root mean square value of high voltage fluctuation ($\sqrt{\sigma^2 V_0}$)	1.5 V
Objective aperture Size	radius =0.1248 $Å^{-1}$
Interaction constant (σ)	8.6361×10^3 $V^{-1}nm^{-1}$

Table 4.1 Parameters used in simulation

At first the simulated profiles of each focal plane were shifted by different but fixed numbers of pixels from their original positions. In addition to the image shift, we also added uncertainty in defocus. This was done in order to reflect inaccurate measurements of objective lens current (random focus shifts for each defocus) as well as inaccurate estimates of the Δf=0 focal plane (a constant focus offset in all focal planes). The reliability of the focus/image shift reconstruction algorithm was quantified using the following figure of merit

$$SSE2 = \frac{\sum_{n=1}^{N} \Delta x^2}{N} \tag{28}$$

where Δx is the difference between the initial imposed shift and the final shift after alignment in pixels for each of the simulated intensity profiles, and N stands for the number of profiles. Table. 2 shows how $N^{e^-}_{pixel}$ and the focus shift affect the profile alignment procedure. The alignment was performed twice for every case to achieve maximum accuracy. Table. 2 also illustrates the rigidity of the present alignment method. The choice of smoothening function (in step 5 of the reconstruction algorithm) does not have any effect on the alignment procedure. Image noise also does not influence the alignment procedure (as seen from Table. 2), because SSE2 = 0.0714 corresponds to 1 pixel misalignment of only 1 image within 14 images.

Focus shift	SSE2											
	Using $N^{e^-}_{pix}$=2000			Using $N^{e^-}_{pix}$=1000			Using $N^{e^-}_{pix}$=600			Using $N^{e^-}_{pix}$=300		
	pfs	*nfs*	*fu*	*pfs*	*nfs*	*Fu*	*Pfs*	*nfs*	*fu*	*pfs*	*nfs*	*fu*
500	0	0	0	0	0	0	0	0	0	0	0	0
1000	0	0	0	0	0	0	0	0	0	0	0	0
2000	0	0.0714	0	0	0.0714	0	0	0	0	0	0	0
3000	0	0.0714	0	0	0.0714	0	0	0.0714	0	0	0	0
4000	0	0.0714	0	0	0.0714	0	0	0.0714	0	0	0	0
5000	0	0.0714	0	0	0.0714	0	0	0.0714	0	0	0	0
6000	0.0714	0.0714	0	0.0714	0.0714	0.0714	0.0714	0.0714	0.0714	0.0714	0	0

Table 4.2 Effect of mean number of electrons per pixel integrated over sample thickness and focus shift on intensity profiles alignment procedure of the current study. Columns *pfs, nfs* and *fu* represent the SS2 values related to the focus shift in positive (overfocus) direction, negative (underfocus) direction and random focus shifts (focus uncertainty) respectively. For example, SSE2 for a systematic focus offset of + (psf) 2000 at N^{e}_{pix}=2000 is 0, but for df_{offset}=-(nfs)2000 it is 0.0714, while random focus shifts (fu) with a maximum amplitude 1000 for each image produce again perfectly aligned images (SSE2=0). Focus offsets in the focus uncertainty (fu)-columns are determined by the focus shift value in column 1 multiplied by uniformly distributed random numbers in the interval [-0.5…0.5].

Image alignment procedure	$SSE2 = \frac{\sum_{n=1}^{N} \Delta x^2}{N}$
This work	0
Using cross correlation	846.67
Using mutual correlation	499.17
Using phase correlation	45.17

Table 4.3 Comparison of intensity profile alignment procedure of current study with cross, mutual and phase correlation method for a series of overfocus images ranging from 1µm to 4 µm with a step size of 0.5 µm using $N^{e^-}_{pix} = 1000$ and without focus shift.

For comparison, three different correlation functions, described by Meyer et al [22], were tested for the same misaligned simulated intensity profiles, giving very poor results. The contrast reversal of images at overfocus and underfocus is the main reason for the failure of these image alignment methods based on different correlation functions in the framework of the current study. Table 4.3 compares the alignment method of the current study with cross-mutual and phase correlation functions only for the overfocus intensity profiles. Here also the correlation function-based image alignment methods do not work properly. Instead of using high resolution images of relatively small defocus range (as described in previous works [15,22]), images across a very large defocus range were used in the present investigation, explaining the result shown in Table. 4.3.

Fig. 4.3c and 4.3d show the reconstructed absorptive and electrostatic potentials respectively for the image profiles shown in Fig. 4.3b, using all the smoothing functions presented in Fig. 4.2. For reconstructing the exit face wave function from a through focal series of simulated images, SSE_{avg} of the last iteration step was chosen to be of the same order of magnitude in the reconstruction of the experimental data in the present study. The function $\exp\left(-(10.5452\cdot k)^4\right)$ produces minimum high frequency noise for both electrostatic and the absorptive potential. Fig. 4.3c also shows that the algorithm can reconstruct $V_{abs}(r)$ quite accurately, as the reconstructed absorptive potential has the same difference in the $V_{abs}(r)$ value ($\Delta V_{abs}(r) = 1.95V$) between the two sides of the interface as the input absorptive potential.

4.3.1. Retrieval of low spatial frequency components of $V'(r)$

The shape of the reconstructed electrostatic potential (Fig. 4.3d) suggests that while the potential drop has been reconstructed rather faithfully, its low spatial frequency components are wrong. This is due to the fact that the microscope transfer function, MTF(k) (expression (2) for small *k*), in relation to the noise present in the data, does not change very much between images for low values of k, despite the very large range of defocus values used here. The DC-component (*k*=0), for example, cannot be reconstructed at all, since the absolute phase is not encoded in the images. In addition, the experimental data presented in this study suffers from the fact that the partially coherent illumination used in our experiments forbids any coherent interaction between points on the specimen that are more than about 100Å apart.

A plot of

$$P(k) = \ln \left\| FT(input\, V'(r)) \right| - \left| FT(reconstructed\, V'(r)) \right\| \qquad (29)$$

serves to identify the range of k-values that have been reconstructed wrongly. The noise introduced in the simulation makes a perfect reconstruction impossible, so that $P(k) > 0$ for most values of k. However, a few low spatial frequency components in $P(k)$ are significantly above average and have therefore not been sufficiently well encoded in the image series, i.e. they are free parameters which must be fixed using additional information about the specimen. For the present investigation, the number of free parameters obtained in this way did not exceed 4 (i.e. for a total length of line profiles of 218Å, k*218Å=*-2, -1, 1, 2*) and turned out to be independent of the value of $N_{pixel}^{e^-}$.

For samples investigated in the present study it is safe to assume that the grains on both sides of the interface are homogeneous. This means that in regions where the correctly reconstructed absorptive potential profile V_{abs}(r) is constant, $V'(r)$ must also be constant, i.e.

$$\left.\frac{\partial V'(r)}{\partial r}\right|_{r\in R} = \left.\frac{\partial V_{abs}(r)}{\partial r}\right|_{r\in R} \qquad (30)$$

Here R defines the range (ideally, one region in each grain) of real space coordinate r over which $V_{abs}(r) \approx const.$ Using the derivative in expression (30) has the advantage that knowledge of the proportionality factor (which depends on material properties as well as the local diffraction conditions) between $V'(r)$ and $V_{abs}(r)$ is not required. A computer program equipped with a graphical user interface (GUI) for very fast definition of the range R by the user, has been written to determine the low spatial frequency components of $V'(r)$ automatically by first performing an exhaustive search and then a least squares refinement. The reconstructed electrostatic potential profile (using a smooth aperture function of $\exp\left[-(10.5452k)^4\right]$) corrected in the way described above is shown in Fig. 4.3e. Apart from some residual noise stemming from the Poisson noise added to the simulated images, it agrees very well with the input. A comparison of Figs. 4.3b and 4.3e shows that feeding the algorithm with 14 images was able to significantly reduce the level of residual noise in the reconstruction. The

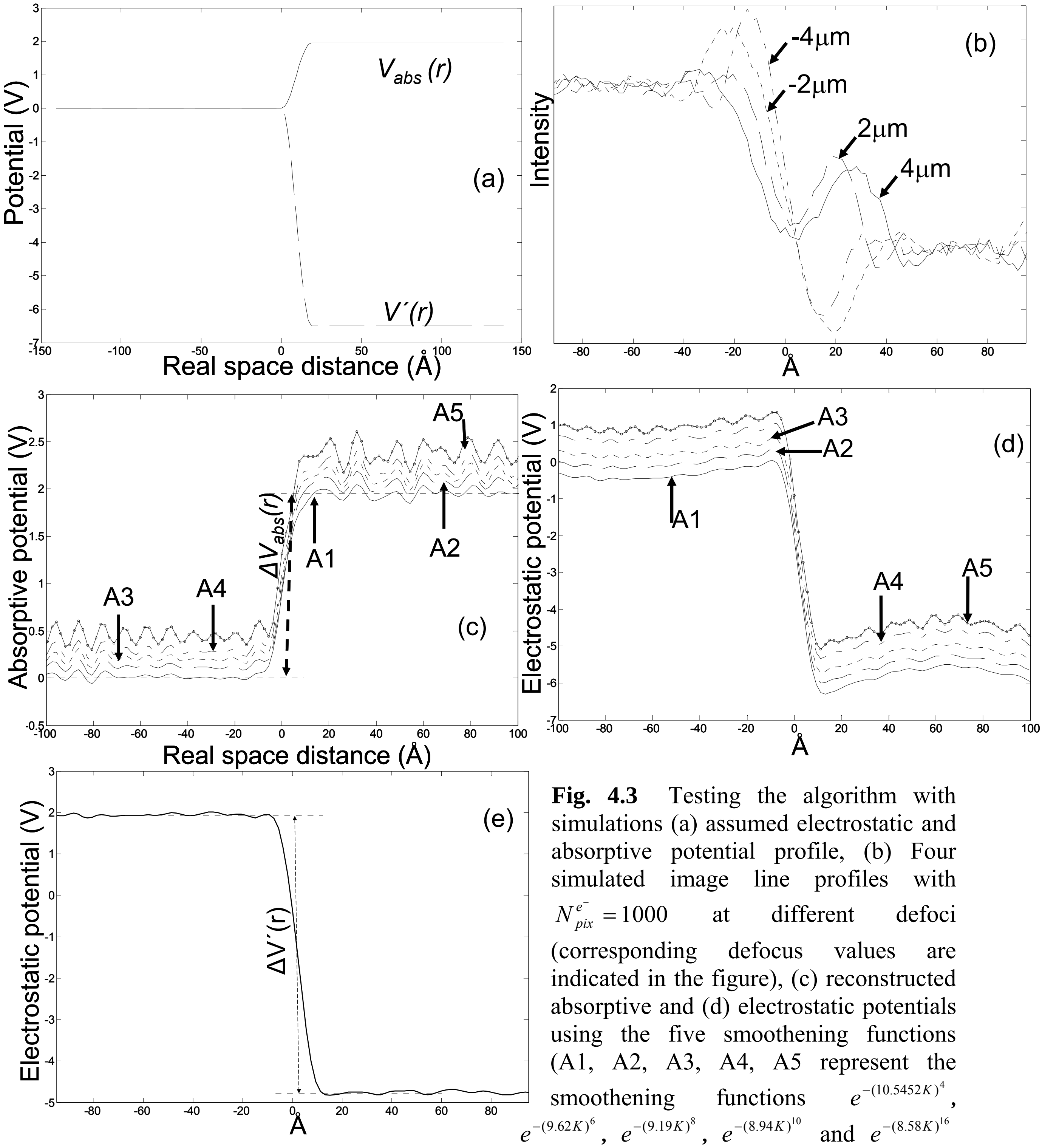

Fig. 4.3 Testing the algorithm with simulations (a) assumed electrostatic and absorptive potential profile, (b) Four simulated image line profiles with $N_{pix}^{e^-} = 1000$ at different defoci (corresponding defocus values are indicated in the figure), (c) reconstructed absorptive and (d) electrostatic potentials using the five smoothening functions (A1, A2, A3, A4, A5 represent the smoothening functions $e^{-(10.5452K)^4}$, $e^{-(9.62K)^6}$, $e^{-(9.19K)^8}$, $e^{-(8.94K)^{10}}$ and $e^{-(8.58K)^{16}}$ respectively) presented in Fig.2. Profiles are shifted intentionally with respect to one another to show the effect of different smoothening functions.(e) electrostatic potential after correcting for wrongly reconstructed low spatial frequency components (with smoothening function $e^{-(10.5452K)^4}$). Here the distance chosen for fitting the low-k components were from -107.1 Å to – 20.5 Å at left side and from 21.4 Å to 96.8Å to the right of the interface.
]

difference between both sides of the interface in the final reconstructed electrostatic potential is the same as in the input ($\Delta V'(r) = 6.65$ V).

4.4 Experimental details

The experimental images were obtained using a Zeiss 912 microscope (Cs=2.7 mm, Cc=2.7 mm, Köhler illumination), operated at 120 kV voltage and equipped with an in-column Omega-type energy filter. The experiments were done using an electron beam of 0.25mrad illumination semi-angle and an objective aperture of size 0.1248 $Å^{-1}$. All focal series were recorded with the energy filter selecting zero energy loss, i.e. 15 eV energy slit centered on the zero loss peak was used.

One experiment was done using a plan view sample of single crystal Al_2O_3 to obtain a through focal series of images from a vacuum-specimen interface. In another experiment, a through focal series of images was captured from an Al-Al_2O_3 interface of a cross-sectional sample where on the Al_2O_3 substrate, layers of Al and Cu, each of 400nm thickness, had been deposited (see [23] for further details about the Al-Al_2O_3 interface). This TEM specimen was provided by Dr. Gunthar Richter and Ms. Limei Cha (Max-Planck-Institut für Metallforschung, Stuttgart, Germany). Both of the specimens were coated with a thin layer of carbon to minimize charging under the electron beam.

Care was taken to keep the interfaces of interest parallel to the incident electron beam. All the experimental images were captured onto a 1024×1024 pixel CCD array using 5 second exposure time at a magnification producing an image scale of about 0.19 nm per pixel. The in-focus condition was calibrated as accurately as possible by minimizing Fresnel contrast. The through focal series of images were taken for defocus values of 1 μm to 4 μm with a step size of 0.5 μm in both over and under focus directions. Digitalmicrograph® software (*Gatan Inc., Pleasanton, CA, USA*) was used to extract line profiles across the same area of the interface from each of the images (line scans were integrated over a width of 100 pixels). The focal series reconstruction and image alignment algorithm was programmed in the Matlab language using MATLAB 7.0® software.

4.5 Application to experimental images

To study the performance of the reconstruction method for experimental data, it was applied to a vacuum- Al_2O_3 interface and an Al –Al_2O_3 interface. The microscopic and experimental parameters, which were used for reconstruction, are listed in Table 1. Led by our results from simulations, we decided to use a smooth aperture function with $q=4$, i.e. $\exp\left[-(10.5452k)^4\right]$ in step 5 of the reconstruction algorithm, since it introduces the least amount of high frequency noise in the reconstructed potential profiles. This aperture function is used for both of the experiments.

4.5.1 Vacuum-Alumina interface

An image of the vacuum-Al_2O_3 interface at an overfocus of 2.5 μm is shown in at the inset of Fig. 4.4a. The dotted box shows the area from where the integrated line scans were taken. Some of the aligned line profiles (of different defocus) across the interface are shown in this figure. As a demonstration of convergence of the algorithm, Fig 4.4b shows a plot of $\ln(SSE_{avg}^{j})$ vs. the number of iterations j. The specimen thickness across the interface along the electron beam is presented in Fig. 4.4c. Reconstructed electrostatic (after fitting the low-k components to the vacuum region) and absorptive potentials are shown in Fig. 4.4d and Fig. 4.4e respectively. Numerical instabilities due to the vanishing specimen thickness in the vacuum region, forced us to set $V'(r) = V_{abs}(r)=0$ for $r<0$.

In Fig. 4.4d, Al_2O_3 shows a more negative electrostatic potential than vacuum. This is because the electrons, being negatively charged particles, are decelerated by the repulsion of the electron clouds of the atoms of the material while traveling through the specimen. Hence the specimen produces a negative phase shift and therefore shows negative electrostatic potential with respect to the vacuum.

The absorptive potential is produced by the sum of the electron scattering outside the objective aperture used in these experiments and the inelastic scattering outside the energy slit of 15 eV width centered at the zero loss peak. The loss of electrons in both, the diffraction plane (by the objective aperture) and the energy-dispersive plane (by the energy slit) produces a positive absorptive potential inside the sample relative to vacuum (Fig. 4.4e).

Just as in off-axis electron holography [1], the estimates for the electrostatic potential are absolute, since they are made in reference to vacuum, where we know that $V'(r)$ $=0$.

All experiments were done using partially coherent electron beam illumination. The coherence width (X_{c}) [24] is the distance at the object over which the illuminating radiation may be treated as perfectly coherent. The coherence width can be calculated as $X_{\mathrm{c}} = \lambda / 2\pi\theta_c$, where λ is the electron wavelength, and θ_c is the illumination semi-angle (the beam divergence). The illumination semi-angle was kept at 0.25mrad for the experiments presented here, resulting in a width of 21.3Å over which the electrons can be treated as being perfectly coherent. For partially coherence beam, another criterion is the incoherence width (X_i) [24], which defines the distance at the object above which the illumination is completely incoherent. The illumination at the object over distances between X_{c} and X_i is partially coherent. X_i is defined as $X_i = \lambda / \theta_c$, which, for the present investigation is 134Å. So it can be stated safely that in the present experimental condition, for both vacuum-Al_2O_3 and Al- Al_2O_3 interface, keeping the interface at the middle, the reconstruction of $V'(r)$ is valid beyond distances of 21.3Å, but not in excess of 134 Å.

Fig. 4.4d shows that the change of $V'(r)$ from vacuum to Al_2O_3 is not abrupt but gradual. This could be due to the formation of an amorphous layer just near the hole produced during ion milling (the final TEM specimen preparation step). A less dense amorphous material consisting of the same atomic species is expected to have lower amplitude of electrostatic potential than its crystalline counter part Al_2O_3.
The mean inner potential of an assembly of neutral atoms is calculated using the equation

$$V_0 = \frac{h_0}{2\pi m_0 |e| \Omega} \sum_{j=1}^{N_{atoms}} f_{el}^{(j)}(s=0) \tag{31}$$

where, Ω is the unit cell volume, m_0 is the rest mass of the electron, e is the charge of an electron, h_0 is Planck's constant and $\sum_{j=1}^{N_{atoms}} f_{el}^{(j)}(s=0)$ is the electron scattering factor of an assembly of neutral atoms [25] at zero scattering angle. Using the information that α- Al_2O_3 has 10 atoms/ unit cell [26] and Ω for Al_2O_3 is 254.81 Å^3

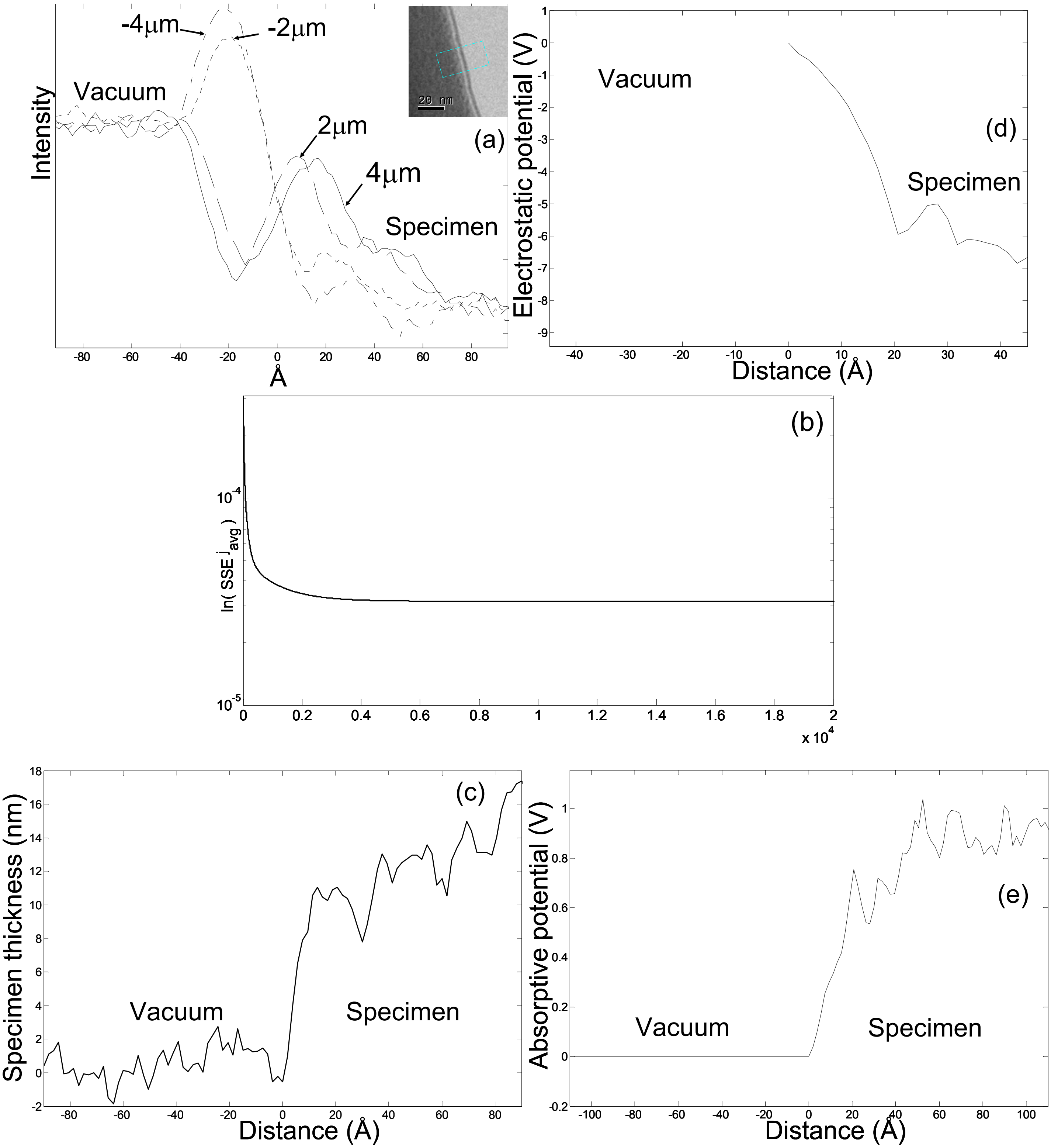

Fig. 4.4 (a) An image of vacuum- Al_2O_3 interface at an overfocus value of 2.5μm (inset) with four experimental 1D intensity profiles across this interface (corresponding defocus values are indicated in the legend), (b) change of averaged sum squared value [$\ln(SSE_{avg})$] with number of iterations, (c) thickness change along the electron beam across the interface (instead of infinity, IMFP for vacuum was chosen the same value as Al_2O_3. The oscillations on the vacuum side are just noise) (d) reconstructed electrostatic potential (after correcting for wrongly reconstructed low-k components), (e) reconstructed absorptive potential

[27], V_0 for Al_2O_3 becomes 6.65 V. For Al (fcc unit cell, lattice parameter 4.0496 Å) we obtain V_0 = 16.97 V.

Fig. 4.4d shows that the experimentally obtained mean inner potential of alumina is 6V <*V(r>edge region)*<7V, i.e. in good agreement with the calculated value of 6.65V.

4.5.2 Al-Al_2O_3 interface

Fig. 4.5a shows an image of the Al-Al_2O_3 interface at an overfocus of 2 μm containing two regions of opposite contrast conditions, caused mainly by local bending. The dotted boxes show the regions (1 & 2) from where the integrated line scans were taken. Fig. 4.5b compares the reconstructed absorptive as well as the electrostatic potentials (after correcting for wrongly reconstructed low-k components) from both of the regions shown in Fig. 4.5a. Although, because of the different diffracting conditions region 1 and 2 have very different absorptive potential profiles, the electrostatic potential profiles look similar and have the same difference at the interface between Al and Al_2O_3. This demonstrates that the local diffraction condition does not have any influence on the reconstructed electrostatic potential.

Since an objective aperture is used in the present study, the expected point to point resolution of the reconstructed potential profiles from the size of the objective aperture is limited to 8 Å. The Al-Al_2O_3 interface, which was investigated in the present study, has been reported to be abrupt [23]. So, this interface may thus be used to determine the resolution of the reconstruction method experimentally. Using Schematic diagrams, Fig. 4.5c demonstrates a way to determine the point to point resolution of the reconstructed potential profiles. An abrupt potential drop (A) at the interface becomes a gradual drop (B) due to limited point to point resolution. In order to estimate the width of this potential drop, the upper portion of the curve B should be flipped about a horizontal mirror axis midway between the potential of the left and right side of the interface. The full width at half maximum (FWHM) of the resulting peak is expressed as the point to point resolution with which the sharp interface can be resolved.

For the actual purpose, the resolution must be determined from the reconstructed electrostatic potential since the reconstructed absorptive potential depends mainly on local diffracting conditions which do not change as abruptly as the material composition. Using the reconstructed electrostatic potential of region 1, the point to point resolution determined is about 8Å as shown in Fig. 4.5d. So, the experimentally determined resolution agrees with that expected from the size of the objective aperture.

The reconstructed $V'(r)$ of the vacuum-Al_2O_3 interface shows that Al_2O_3 has lower potential than vacuum. In the same way, for Al-Al_2O_3 interface, Al should show a lower electrostatic potential than Al_2O_3. However, the electrostatic potentials in Fig. 4.5b indicate the opposite. Hence, to retrieve the real phase change at this interface, the phase should be unwrapped. Since Al has a more negative potential than Al_2O_3, a phase-shift of 2πn (n=0, 1, 2, 3…) needs to be added to the phase of the reconstructed exit face wave function on the Al_2O_3 side of the interface. Fig. 4.5e shows the electrostatic potential after adding 4π to the reconstructed $\mathrm{Real}(\phi)$ at the Al_2O_3 side for region 1. In this case the choice of n=2 was motivated by prior knowledge of the material properties. Focal series reconstructions at specimen areas of different thicknesses would be required to determine n from experiment alone.

This figure shows that the difference $\Delta V'(r)$ at the interface between Al and Al_2O_3 stays near to the calculated value of ΔV_0 (Al-Alumina) = 10.3 V. Errors may be present in both, the experimental, as well as the calculated value of V_0. Our computation of V_0, for example, assumed neutral atoms, and may for this reason alone be incorrect.

4.6 General discussion

The accuracy of the retrieved potential profile, and therefore an additional source of the discrepancy between the calculated and reconstructed mean inner potential, depends on a good estimate of the IMFP of Al and Al_2O_3 (essential for accurate specimen thickness determination), as well as the Stobbs factor [28]. One should also bear in mind that dynamic scattering effects are not fully taken into account by the phase-object approximation. However, a new, more accurate method of retrieving the projected potential of a crystalline sample by dynamic inversion from an exit face wave function has recently been developed [29].

If no vacuum reference phase is available, the reconstructed electrostatic potential profile represents only the relative change of the potential across the interface, as in the second example above, the Al-Al_2O_3 interface. However, knowing the mean inner potential of at least one of the components next to the interface will allow an absolute scale to be given to the potential profile. The exit face wave function was normalized with respect to its maximum value (while retrieving the projected potential). This

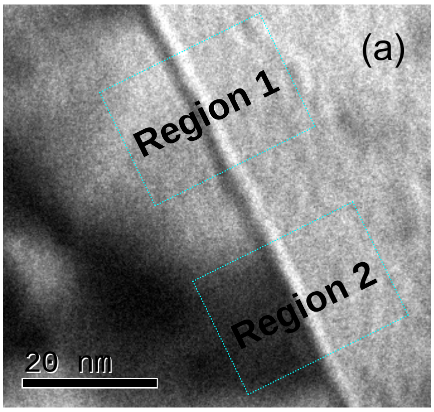

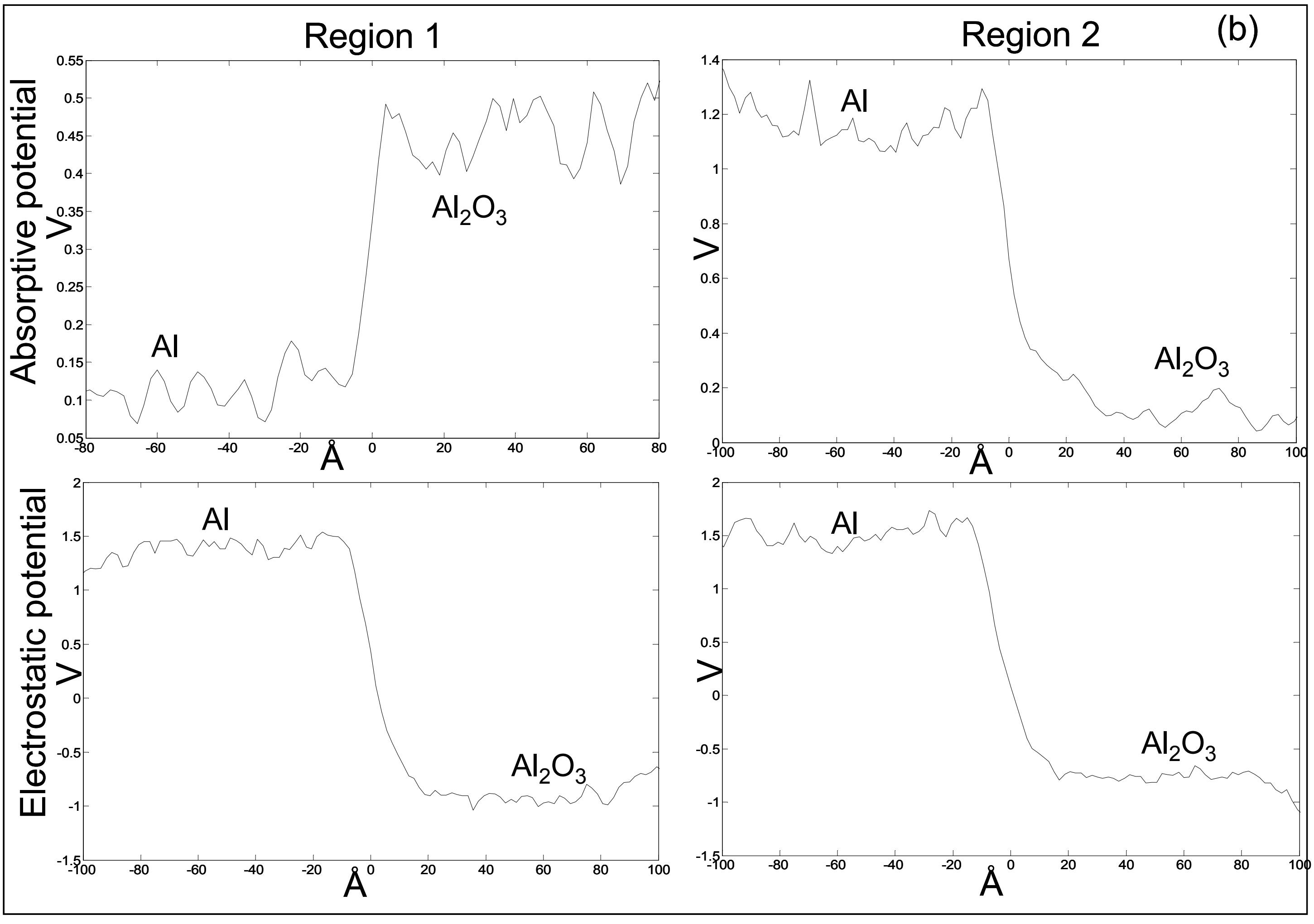

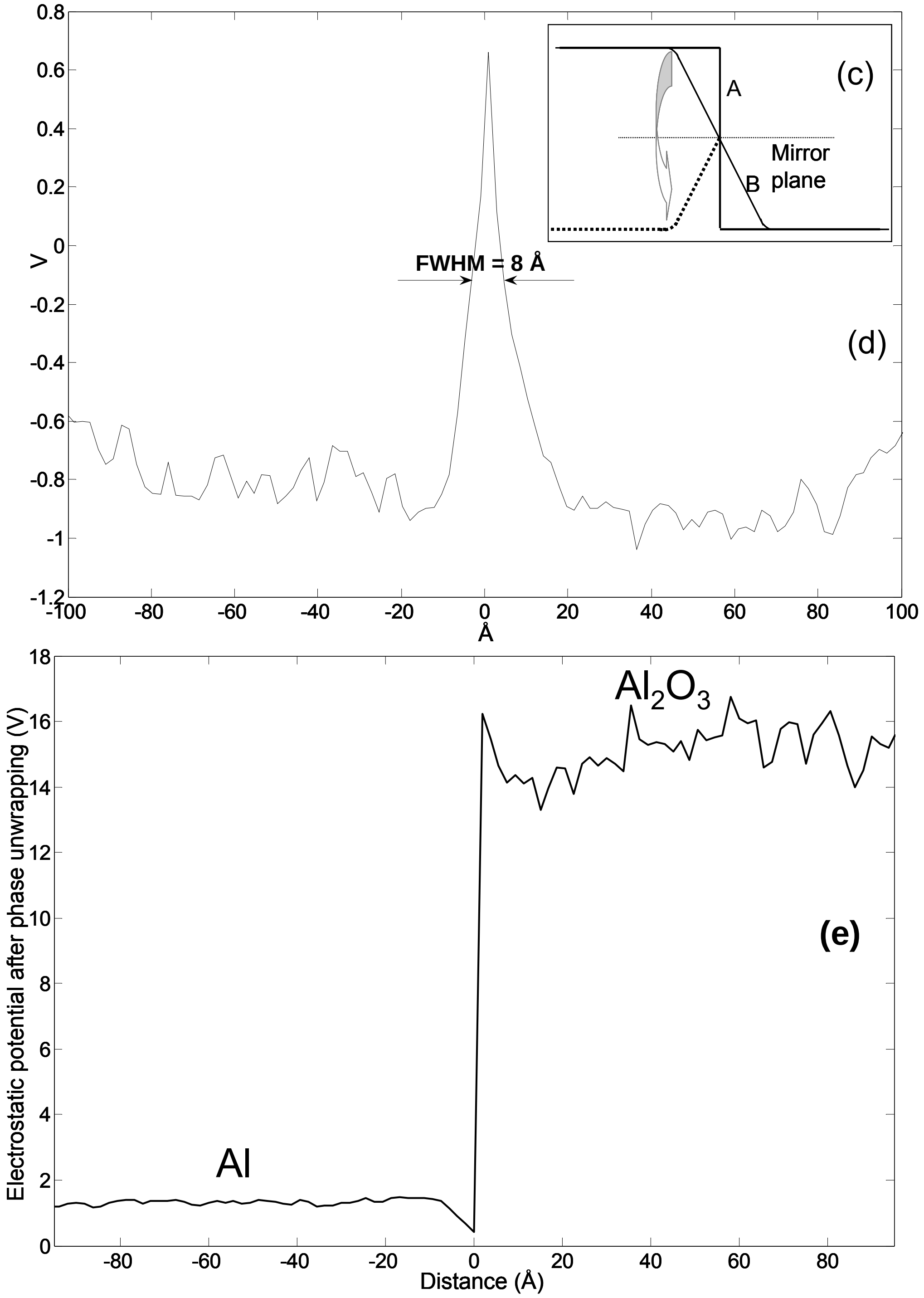

Fig. 4.4 (a) An image of Al- Al_2O_3 interface at an overfocus value of 2 μm, showing contrast variations due to local bending. (b) comparison of the reconstructed absorptive as well as the electrostatic potentials (after correcting for wrongly reconstructed low-k components) from region 1 and 2, (c) Schematic to demonstrate the way to determine the point to point resolution of the reconstructed profiles (d) determination of point to point resolution from the reconstructed electrostatic potential of region 1 (e) electrostatic potential across Al-Al_2O_3 interface from region 1 after phase unwrapping.

procedure eliminates negative values in the absorptive potential, i.e. the apparent production of electrons by the sample itself. The scale of the absorptive potential is therefore relative to the least absorbing point within the field of view. A more rigorous normalization would be to divide by a flat field image (an image recorded without a specimen in the field of view) recorded under the same imaging conditions. This would give the absorptive potential profile an absolute scale and may be important for quantitative measurements involving both absorptive, as well as the electrostatic potential, or their ratio.

It may also be mentioned that it is possible to check whether the reconstructed exit face wave function is really at the in-focus ($\Delta f=0$) plane. Using expression (26), it is possible to propagate the complex wave function in free space until the contrast in its amplitude is minimized since the in-focus plane is the focal plane of minimum (Fresnel) image contrast.

Both the inelastic scattering described by $V''(r)$ and the pseudo-absorptive by $V'''(r)$ increase with the atomic number (Z) of the scattering element. In fact, high-angle annular dark-field scanning transmission electron microscopy (HAADF-STEM) technique, being mainly based on $V'''(r)$, is also called Z-contrast STEM for this very reason. If no energy slit is used, then the absorptive potential represents only the scattering outside the objective aperture, i.e. scattering to relatively high angle. However, the high-angle scattering signal present in images is strongly attenuated by the temporal and spatial coherence envelopes.

4.7 Conclusions

A modified version of the iterative wave function reconstruction (IWFR) method [15] for reconstructing the exit face wave function using through focal series has been presented. It was applied to reconstruct the wave function using line profiles across interfaces. The electrostatic and absorptive potential profiles across interfaces are obtained from the reconstructed wave function using the phase-object approximation (POA). A new alignment procedure of experimental line profiles has been introduced and its robustness in the presence of high noise and uncertainties in defocus has been tested using simulated images. For the present study, it produces the best alignment in comparison with alignment procedures existing in the literature. Mean inner potentials retrieved by this method agreed well with literature values. The resolution of the reconstruction is determined by the size of the objective aperture, as was confirmed by tests on an abrupt interface. The reconstructed electrostatic potential has been found to be insensitive to the sample orientation, although, due to the presence of an objective aperture, the absorptive potential is strongly depended on the local orientation and thus diffracting condition.

For surfaces, i.e. vacuum-specimen interfaces, the electrostatic potential profile represents the absolute mean inner potential profile of the material next to the vacuum. For internal interfaces, only relative changes in potential can be measured. This method can prove to be very useful for determining phase shift and the compositional changes across interfaces such as intergranular glassy films in ceramics.

4.8. References:

---

[1] Y.G. Wang, V.P. Dravid, Phil. Mag. Letters 82 [8] (2002) 425.

[2] B.A. Gurovich, B.A. Aronzon, V.V. Ryl'kov, E.D. ol'shanskii, E.A. Kuleshova, D.I. Dolgii, D.Y. Kovalev, V.I. Filippov, Semiconductors 38 [9] (2004) 1036.

[3] M. Arakawa, S. Kishimoto, T. Mizutani, Japanese Journal of Applied Physics Part 1, 36 [3B] (1997) 1826.

[4] C.T. Koch, S. Bhattacharyya, M. Rühle, R.L. Satet, M.J. Hoffmann, Microsc. Microanal., in press (2005)

[5] F.M. Ross, W.M. Stobbs, Philos. Mag. A 63 (1991) 1 37.

[6] J.N. Ness, W.M. Stobbs, T.F. Page, Philos. Mag. A 54 (1986) 679.

[7] F. Kara, R.E. Dunin-Borkowski,C.B. Boothroyd, J.A. Little, W.M. Stobbs, Ultramicroscopy 66 (1996) 59.

[8] R.E.Dunin-Borkowski, Ultramicroscopy 83 (2000) 193.

[9] E.J. Kirkland, Ultramicroscopy 15 (1984) 151.

[10] W.M.J. Coene, A. Thust, M. Op de Beeck , Ultramicroscopy 64 (1996) 209.

[11] A. Thust, W.M.J. Coene, M. Op de Beeck, D. Van Dyck Ultramicroscopy 64 (1996) 211.

[12] L.J. Allen, M.P. Oxley, Opt. Commun. 199 (2001) 65.

[13] L.J. Allen, M.P. Oxley, D. Paganin, Phys. Rev. Lett. 87(2001)123902.

[14] R. Vincent, Ultramicroscopy 90 (2002) 135.

[15] L.J. Allen, W. McBride, N.L. O'Leary, M.P. Oxley, Ultramicroscopy 100 (2004) 91.

[16] D.B. Williams and C.B. Carter, Transmission Electron Microscopy, Plenum Press, New York, 1996, p. 463.

[17] L.J. Allen, H.M.L. Faulkner, K.A. Nugent, M.P. Oxley, D. Paganin, Phys. Rev. E 63 (2001) 037602.

[18] D. R. Rasmussen, C.B. Carter, Ultramicroscopy 32 (1990) 337.

[19] R.F. Egerton, Electron Energy-Loss Spectroscopy in the Electron Microscope, 2nd edition, Plenum Press, New York, 1996, p.302-305.

[20] S. Bhattacharyya, A.Subramaniam, C.T. Koch, M. Rühle, Mat. Sc.& Engg. A., accepted (2005) (Chapter 3).

[21] W. Nüchter, Ph.D thesis, Universität Stuttgart, 1997, p. 41.

---

[22] R.R. Meyer, A.I. Kirkland, W.O. Saxton, Ultramicroscopy 92 (2002) 89.

[23] G. Dehm, B.J. Inkson, T. Wagner, Acta Mater. 50 (2002) 5021.

[24] J.C.H. Spance, Experimental High Resolution Electron Microscopy, Clarendon Press, Oxford,1981, p. 93-119.

[25] L.-M. Peng, Micron 30 (1999) 625.

[26] I Levin and D. Brandon, J.Am.Ceram.Soc. 81 [8] (1998) 1995.

[27] JCPDS-International Centre for Diffraction Data, v. 1.30 (1997).

[28] A. Howie, Ultramicr. 98 (2004) 73-79.

[29] N.L. O' Leary and L.J. Allen, Acta Cryst. A 61 (2005) 252.

CHAPTER 5

Projected potential profiles across intergranular glassy films

S. Bhattacharyya, C. T. Koch and M. Rühle
Journal of the American Ceramic Society, Submitted

Abstract

Projected electrostatic and absorptive potential profiles across intergranular glassy films (IGFs) and interfaces between grains and glassy pockets in silicon nitride ceramics were obtained by reconstructing the electron exit face wave function from a series of defocused TEM images. The phase-object approximation (POA) was used for extracting the projected potential from the complex-valued exit-face wave function. The electrostatic as well as the absorptive potentials were scaled with respect to vacuum. For La_2O_3-MgO doped Si_3N_4, the potential profiles across the grain / glassy pocket interface and the IGF were observed to be very similar and give very strong evidence for the existence of a space charge layer at the interface.

5.1 Introduction

Understanding structure and composition of interfaces is crucial for the design of ceramic materials. In ceramics such as Si_3N_4 [1] and SiC [2] 1-2nm thick intergranular glassy films (IGF) are present at the grain boundaries. Although most literature focuses on IGFs in Si_3N_4, ZnO and SiC, they have also been observed at grain boundaries in other ceramics (e.g., $SrTiO_3$[3], Al_2O_3[4]), at metal-ceramic interfaces (e.g. Si_3N_4-Al [5],Al_2O_3-Ni [6]), and at hetero-interfaces in composite creamics (e.g. ruthenate-silicate glass [7], Si_3N_4-SiC [8]) etc. Varying the composition of IGFs has profound influence on material properties such as creep resistance, oxidation resistance, fracture toughness etc. Many transmission electron microscopic techniques have been used so far to investigate structure and chemistry of IGFs. The film width has commonly been measured by high resolution lattice fringe imaging, diffuse dark field imaging or Fresnel fringe imaging [3,9]. Energy dispersive X-ray spectroscopy (EDXS) and electron energy loss spectroscopy (EELS) have been used to study their chemistry [10, 11] Recently segregation of heavy elements at IGFs was imaged using high-angle annular dark field scanning transmission microscopy (HAADF-STEM)[12, 13, 14] High frequency components of the phase across the IGF of yttria doped Si_3N_4 were mapped at atomic resolution using high resolution images at different foci [15]. Off-axis electron holography has been used to determine the local electrostatic potential and associated space charge across an IGF [16] while electron diffraction experiments were able to provide IGF potential profiles averaged over large distances along the boundary [17].

The mean inner potential profile across grain boundaries provides useful information about variations in composition and density across it, as well as about intrinsic potentials accociated with depletion layers or space charge [18]. The projected electrostatic potential within a TEM specimen induces a phase-shift in the wave function describing a fast electron passing through the specimen, and may therefore be measured by either off-axis or in-line holographic methods [19]. Stobbs and coworkers developed an approach to use the Fresnel contrast (contrast in largely defocused images produced by a wave function containing local phase differences, i.e. in-line holography) to analyze potential profiles across interfaces by fitting a model potential profile described by only a few parameter to the fringe contrast. This approach was reviewed and extended further by Dunin-Borkoski [18]. Since variations in projected potential are only expected across, but not along an interface the Fresnel contrast method, in this case, only requires line profiles extracted from a series of images with varying defocus normal to the plane of the defect. Minimizing the difference between experimental and simulated images, Dunin-Borkoswki fitted the interface width, the magnitude of its potential well or hill and the diffuseness of its boundaries to the experimental image intensity profiles by comparing them with simulated ones at every defocus for the entire experimental defocus series. The solution to this global non-linear optimization problem is a projected potential profile that can be described by the given parameter set [18] and produces Fresnel contrast images most similar to the experimental ones.

Recently, Bhattacharyya et al [20] reported the development of a phase retrieval method suitable for application to energy-filtered Fresnel contrast focal series based on the iterative wave function retrieval (IWFR) algorithm developed by Allen et al [21]. This method solves the above mentioned global optimization problem without the need for reducing the parameter space, or limitations on the defocus step size as is the case for the transport-of-intensity-equation (TIE) based approach [22, 23] It therefore does not require the assumption of any model shape describing the potential profile. The projected potential may be extracted from the reconstructed wave function using the phase-object approximation (POA).

$$\psi(r) = \exp\left(i\sigma t V(r)\right), \tag{1}$$

where V(r) is the projected potential and may be complex. Ψ(r), σ and t are the exit face wave function, relativistic electron interaction constant and specimen thickness along the electron beam respectively. The real (electrostatic) part of the projected potential produces a pure phase shift in the exit face wave function, while its imaginary part (responsible for inelastic and high-angle scattering outside the objective aperture, as produced by the presence of atomic species of higher Z) affects only its amplitude.

In this paper, we used the above mentioned method to retrieve potential profiles across IGFs in Si_3N_4, a ceramic material with many industrial applications, whose mechanical properties vary strongly with composition of the IGFs [24]. Koch et. al. [17] reconstructed the shape of the projected potential profile across an IGF of Lu_2O_3-MgO doped Si_3N_4 ceramics with an arbitrary scale from a tilt series of energy-filtered electron diffraction patterns. To the best of our knowledge, this paper contains the first report of the potential profiles across an IGF in a Si_3N_4 ceramic with absolute scale. A new measure of the IGF width, referred to as “potential well width”, is also introduced here. For one of the samples, not only the projected potential profiles across the IGF but also across the adjacent grain/glassy pocket interface were determined which gives a new insight about the nature of the potential profiles across the IGF.

5.2 Experimental details

Dense silicon nitride samples with Lu_2O_3 and MgO doping have been prepared by Satet and Hoffmann [24] from milled and sieved α-Si_3N_4 (88.07 wt%), SiO_2 (2.16 wt%), MgO (1.07 wt%) and Lu_2O_3 (8.7 wt%) powders, by first cold pressing, then sintering at 1750°C for 15 min at a pressure of 10 bar and finally hot isostatic pressing (HIP) at 1750°C for 60 min at 100 bar. To prepare the La_2O_3 and MgO doped Si_3N_4 sample, a mixture of milled and sieved α-Si_3N_4 (88.6 wt%) with SiO_2 (2.20 wt%), MgO (2 wt%) and La_2O_3 (7.2 wt%) powders was cold pressed followed by sintering at 1780°C for 14 min at a pressure of 10 bar and finally hot isostatic pressing at 1780°C for 30 min at 100 bar.

The specimens for transmission electron microscopy were prepared by the standard techniques of grinding, dimpling and ion-beam thinning (Precision Ion Polishing System, Gatan Inc.). The ion-beam thinning was carried out at an angle of inclination of 8° of the ion beam to the sample. The Si_3N_4 specimens were coated with a thin layer of carbon to minimize charging under the electron beam.

The experiments were performed using a Zeiss 912 microscope (Cs=2.7 mm, Cc=2.7 mm, Köhler illumination), operated at 120 kV voltage and equipped with an in-column Omega-type energy filter. Same experimental conditions were maintained for every experiment by using an electron beam illumination semi-angle of 0.25 mrad and an objective aperture of size 0.1248 $Å^{-1}$.

Care was taken to orient the interfaces of interest (e.g. grain boundaries) parallel to the incident electron beam (edge-on condition). The specimens were further tilted, keeping the grain boundaries of interest edge-on, in a way to orient the grains on either side of the boundary to weak diffracting conditions [25].

To acquire the energy filtered images, a 15 eV energy slit centered on the zero loss peak was used. All the experimental images were captured onto a 1024×1024 pixel CCD array using 5 second exposure time at a magnification producing an image scale of about 0.19 nm per pixel. The through focal series of images were taken from the defocus value of 1 μm to 4 μm with a step size of 0.5 μm in both over and under focus directions. Digital micrograph software (*Gatan Inc., Pleasanton, CA, USA*) was used to extract line profiles across the same area of the interface from each of the images ((line scans were integrated over a width of 100 pixels). The data were processed using programs written in MATLAB 7.0 software to reconstruct the exit face wave function.

5.3 Retrieval of the projected potential

The projected potential was retrieved from the Fresnel contrast image focal series as described by Bhattacharyya et al.[20]. This algorithm reconstructs the exit face way function in an iterative way. The distinct features of this algorithm are:

1. Image drift compensation for images recorded with largely different focus and thus contrast.
2. Numerical stability even in the presence of missing spatial frequency components in the microscope transfer functions at some defoci.
3. Low spatial frequency components of the electrostatic potential may be retrieved by applying prior knowledge of areas of constant potential (e.g. inside the grains, or regions of vacuum).

An outline of the projected potential retrieval procedure is presented in Fig. 5.1. Finally, the projected potential is split up as

$V(r) = V'(r) + iV_{abs}(r)$,

where, potential $V'(r)$ is due to the elastic interaction of the electron with the specimen referred to as the 'electrostatic potential', and $V_{abs}(r) = [V''(r)+V'''(r)]$ describes the loss of electrons due to inelastic scattering events ($V''(r)$) and elastic scattering outside the objective aperture ($V'''(r)$) and may be called objective aperture dependent 'pseudo-absorptive' scattering potential[20, 26]. While the use of a small objective aperture greatly enhances Fresnel contrast it also allows this 'pseudo-absorptive' potential to be mapped with better signal/noise ratio.

In the work reported previously [20], the reconstructed exit face wave function was normalized with respect to its maximum value (for extracting the projected potential) to eliminate physically insensible negative values in the absorptive potential, i.e. the apparent production of electrons by the sample itself. The scale of the absorptive potential is therefore relative to the least absorbing point within the field of view. A more rigorous normalization is proposed also in that paper where images of all focal planes are divided by a flat field image (an image recorded without a specimen in the field of view) recorded under the same imaging conditions to give the absorptive potential profile an absolute scale. This latter method of normalization has been applied in the work presented here.

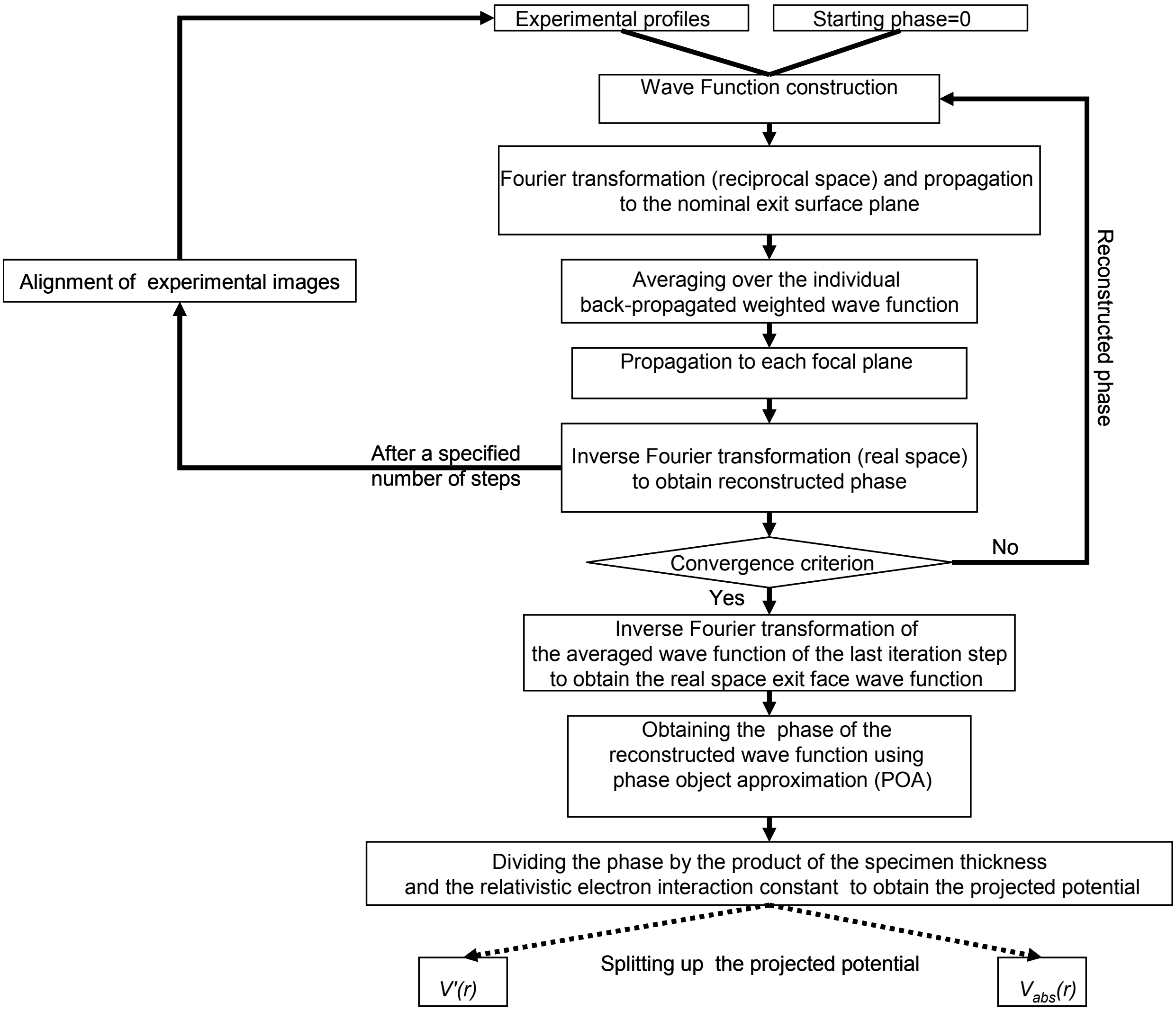

Fig. 5.1 Outline of the projected potential retrieval procedure

Despite its potential the method as implemented for this work also suffers from the limited resolution of 8 Å imposed by the objective aperture. The use of a thermionic LaB_6 electron gun also limits the spatial coherence which puts an upper limit on the IGF widths that can be observed. For the present study the film widths have been well within the limits imposed by the spatial coherence. Although dynamic scattering effects are not completely taken into account by the phase-object approximation, differences to the exact multiple scattering theory including finite excitation errors are expected to be negligible for amorphous materials imaged at only intermediate resolution.

5.4 Results

The specimen thickness along the direction of the electron beam was determined using only two images, one zero-loss filtered one (I_0) and one unfiltered one (I_l), both recorded with the same exposure time. Using the 1D intensity profiles taken from the same area of the images as the ones in the focal series reconstruction, the local specimen thickness, t, is calculated according to Egerton [27] :

$$t = \lambda_{inel} \ln\left(\frac{I_l}{I_0}\right) \qquad (2)$$

where, λ_{inel} is the inelastic mean free path (IMFP) of the electron in the given material that was calculated as described by Egerton[27]. For Si_3N_4 λ_{inel}=132.2nm.

Where no vacuum reference phase was available within the field of view the reconstructed electrostatic potential profile of IGF and Si_3N_4 grain/triple pocket interface has been scaled with respect to the mean inner potential of the Si_3N_4 grains experimentally determined from a Si_3N_4/vacuum interface. This is possible because of the insensitivity of the specimen induced electron wave phase shift on grain orientation, i.e. the local diffraction condition [20]. Just as in off-axis holography [28], the estimates for the electrostatic potential are absolute, since they are made in reference to vacuum, where we know that $V'(r) = 0$.

5.4.1 Vacuum / Si_3N_4 interface

An image of the vacuum / Si_3N_4 interface at an overfocus of 1.1 μm is shown in Fig. 5.2a. The dotted box shows the area from where the integrated line scan was taken. Some of the aligned and normalized 1D experimental intensity profiles (of different defocus) across the interface are shown in Fig. 5.2b. To make the thickness variation smooth, starting from the edge to the sample, the thickness profile was replaced by a fitted 2nd order polynomial as shown in Fig. 5.2c. Reconstructed electrostatic and absorptive potentials of this interface are shown in Figs. 2d and 2e respectively. Numerical instabilities due to the vanishing specimen thickness in the vacuum region forced us to set $V'(r) = V_{abs}(r) = 0$ for $r<0$.

In Fig. 5.2d, Si_3N_4 shows a more negative electrostatic potential than vacuum. This is because the fast electrons, being negatively charged particles, are decelerated by the repulsion of the electron cloud induced potential of the atoms of the material while traveling through the specimen. Hence the specimen produces a negative phase shift and therefore shows negative electrostatic potential with respect to the vacuum.

The absorptive potential is basically the sum of the electron scattering outside the objective aperture used in these experiments and the inelastic scattering outside the energy slit of 15 eV width centered at the zero loss peak. The loss of electrons in both, the diffraction plane (by the objective aperture) and the energy-dispersive plane (by the energy slit) produces a positive absorptive potential inside the sample relative to vacuum (Fig. 5.2e).

All experiments were done using partially coherent electron beam illumination. The coherence width (X_c) [29] is the distance at the object over which the illuminating radiation may be treated as perfectly coherent. The coherence width can be calculated as $X_c = \lambda/2\pi\theta_c$, where λ is the electron wavelength, and θ_c is the illumination semi-angle (the beam divergence). The illumination semi-angle was kept at 0.25 mrad for all the experiments presented here, resulting in a width of 21.3 Å over which the electrons can be treated as being perfectly coherent. For partially coherence electron irradiation, another criterion is the incoherence width ($X_i = \lambda/\theta_c$ =134Å) [29], which defines the distance at the object above which the illumination is completely incoherent. Spatial frequency components of the illuminating electron wave function corresponding to wave numbers between 21.3Å and 134Å are partially coherent. The present experimental conditions are therefore sufficient for the reconstruction of $V'(r)$ across distances relevant to IGFs in Si_3N_4.

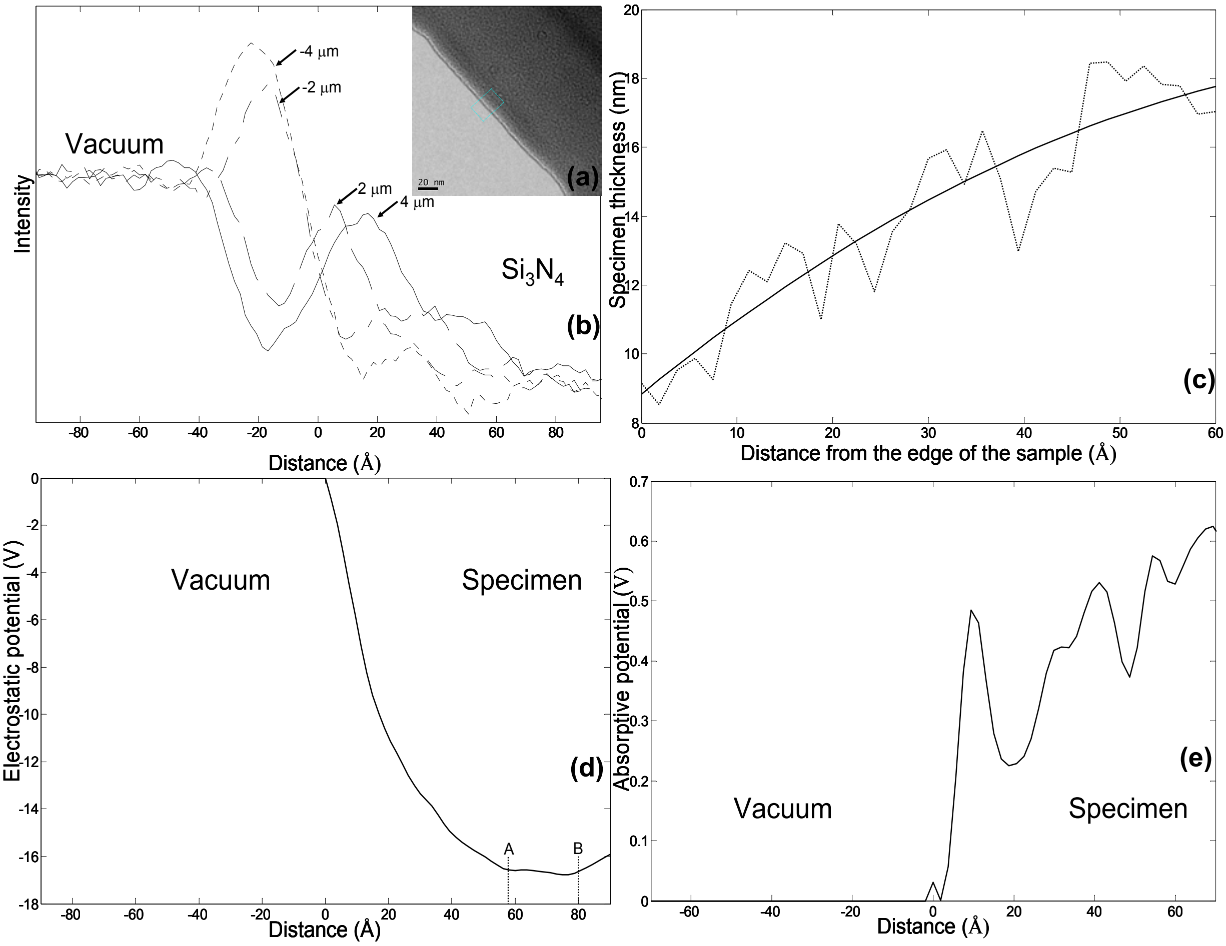

Fig. 5.2 (a) Image of a vacuum / Si_3N_4 interface at an overfocus value of 1.1μm. (b) Line profiles across the grain boundary extracted from 4 images of different foci (corresponding defocus values are indicated in the legend), (c) specimen thickness along the electron beam (d) reconstructed electrostatic potential (low spatial frequency components were determined by assuming that the vacuum region for $-112.6Å<x<-28.9Å$ is featureless) and (e) reconstructed absorptive potential

Figure 2d shows that the change of $V'(r)$ from vacuum to Si_3N_4 is not abrupt but gradual. This could be due to the formation of an amorphous layer just near the hole produced during ion milling, the final TEM specimen preparation step. A less dense amorphous material consisting of the same atomic species is expected to have lower amplitude of electrostatic potential than its crystalline counter part Si_3N_4.

The average electrostatic potential of Si_3N_4 as determined from the region AB of Fig. 5.2d is -16.7 V. This experimentally determined mean inner potential of Si_3N_4 is in good agreement with the calculated value (-17.4 V [17]). The discrepancy between the calculated and reconstructed mean inner potential, depends on a good estimate of the IMFP of Si_3N_4 (essential for accurate specimen thickness determination), the neutral atom assumptions related to the calculation, as well as the Stobbs factor [30]. Beyond point B (Fig. 5.2d) $V'(r)$ again increases due to the limited spatial coherence in the microscope used for this investigation.

5.4.2 La_2O_3-MgO doped Si_3N_4

5.4.2.1 Intergranular glassy film

An image of the grain boundary of interest together with the glassy pocket, at an overfocus value of 3 μm, is shown in Fig. 5.3a. Here also the dotted boxes show the areas from where the integrated line scans were taken. The specimen thickness along the electron beam direction is presented in Fig. 5.3b. As the exact composition of the IGF is not known, the IMFP of Si_3N_4 was also used for the IGF. Since the thickness did not vary much within each of the 2 grains, averaged numbers have been used instead of the more noisy experimentally determined thickness profile (numbers given in Fig. 5.3b). The mean of these two thickness values was assumed as the specimen thickness across the IGF. This assumption ignores any preferential thinning near the grain boundary due to ion milling.

The scaled (absolute) reconstructed electrostatic and the absorptive potentials across the IGF are presented in Fig. 5.3c and Fig. 5.3d respectively. The full width at half maximum (FWHM) of the electrostatic potential profile across the IGF will be regarded as the "potential well width" from here on. This width, for the profile shown Fig. 5.3c, is 2.3 nm. This figure shows that the IGF has less negative electrostatic potential i.e. less mean inner potential than the Si_3N_4 grains adjacent to it.

Due to different diffracting conditions, the grains in either side of the IGF show different absorptive potentials, as shown in Fig. 5.3d. Elastic scattering to large angles may be approximated rather well by the Rutherford elastic scattering cross section which is proportional to the square of the atomic number of the scattering element. As reported by different researchers [12,13,14] using HAADF-STEM, in La_2O_3-MgO doped Si_3N_4 ceramics, La atoms segregate at the IGF / grain interface when the prism plane of β-Si_3N_4 constitutes the interface plane. In Fig. 5.3e, the overview of the examined area at lower magnification, shows that in grain 2 which is a grain with high aspect ratio, the longest plane is the interface plane (IGF / grain interface). According to Petzow and Herrmann [31], in β-Si_3N_4 ceramics, the longest planes of the grains with high aspect ratio, are the prism planes. So, here the interface plane of grain 2 is probably the prism plane on which La atoms segregate. Since the atomic number of La is $Z_{La}=57$ ($Z_{Si}=14$, $Z_N=8$), high-angle scattering outside the objective aperture is expected to be larger within the IGF than in the adjacent Si_3N_4 grains. That is why the IGF shows a larger absorptive potential than the grains next to it.

5.4.2.2 Grain / glassy pocket interface

The image of this interface at an overfocus of 3 μm is shown in Fig. 5.3a. Since the exact composition of the amorphous material in the triple pocket is not known, it is assumed that the thickness along the beam direction remains constant across the interface and the average thickness of the Si_3N_4 grain at one side of the interface was used for the whole line profile. This assumption ignores preferential thinning in the triple pocket region during ion milling. The scaled (absolute) electrostatic and the absorptive potentials across this interface are shown in Fig. 5.4a and Fig. 5.4b respectively. Assuming the electrostatic potential of the Si_3N_4 grain as the base, the potential well width of this interface is 2.6 nm.

According to Winkelman et al [14], in this material, La atoms segregate to the glassy pocket / grain interface when prism planes of β-Si_3N_4 constitute the interface plane. So, for the same reason as IGF, the glassy pocket shows a higher absorptive potential than the adjacent grain.

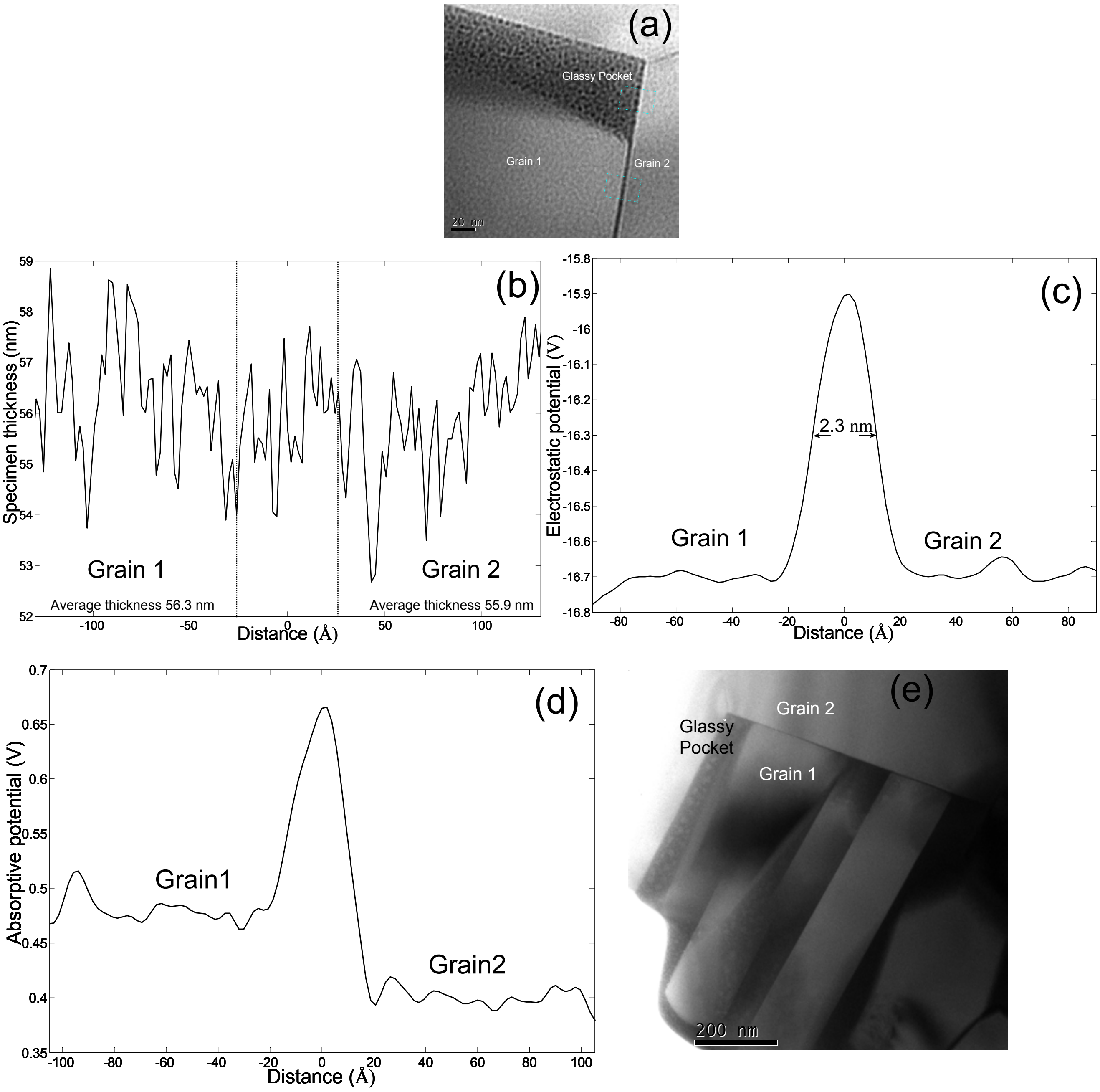

Fig. 5.3 (a) Image of an IGF and glassy pocket in a La$_2$O$_3$-MgO doped Si$_3$N$_4$ ceramics at an overfocus value of 3μm. (b) Specimen thickness along the electron beam (c) reconstructed electrostatic potential (The potential was assumed to be constant for -101.5Å<x<-23.3Å and also for 40.9Å<x<127.6Å) and (d) reconstructed absorptive potential across IGF (e) overview of the area at low magnification.

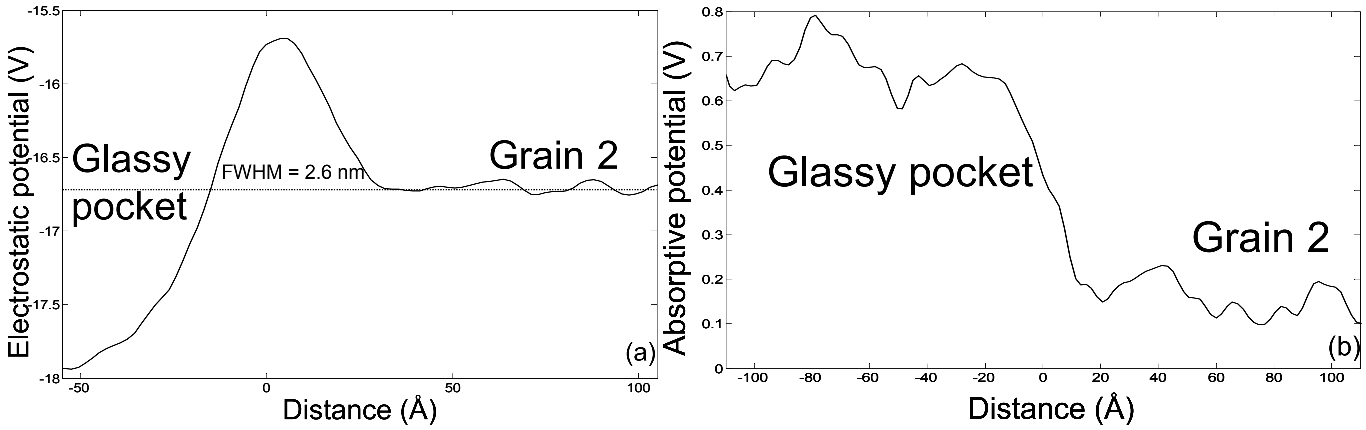

Fig. 5.4 (a) Reconstructed electrostatic potential (from the potential was assumed to be constant for 15.8Å<x<105.2Å) and (b) reconstructed absorptive potential of IGF/ glassy interface.

5.4.3 Lu_2O_3-MgO doped Si_3N_4

An image of the IGF of interest at an overfocus of 2 μm is shown in Fig. 5.5(a). Here also the dotted box indicates the region from which the line profile has been extracted. To determine the specimen thickness along the electron beam we used the same procedure as used for the IGF in the La_2O_3-MgO doped Si_3N_4 ceramics.

The reconstructed electrostatic and absorptive potentials across the IGF are presented in Figs. 5b and 5c respectively. Fig. 5.5b shows that the IGF also has a less negative electrostatic potential than the Si_3N_4 grains adjacent to it. The slanted region AA' of the profile just beside grain 1 has no equivalent in the absorptive potential profile. The measured potential well width is 2.2 nm which agrees well, within the resolution limit of the present method, with the FWHM of the electrostatic potential profile of an IGF of the same material (2.03 nm) as investigated by Koch et al [17]. Just as in the previous example, in Lu_2O_3-MgO doped Si_3N_4 ceramics, Lu atoms segregate at the IGF / grain interface when a prism plane of β-Si_3N_4 constitutes the interface plane [13,14]. Here again grain 1 is a grain with high aspect ratio bordering the IGF with one of its long sides (the prism plane).

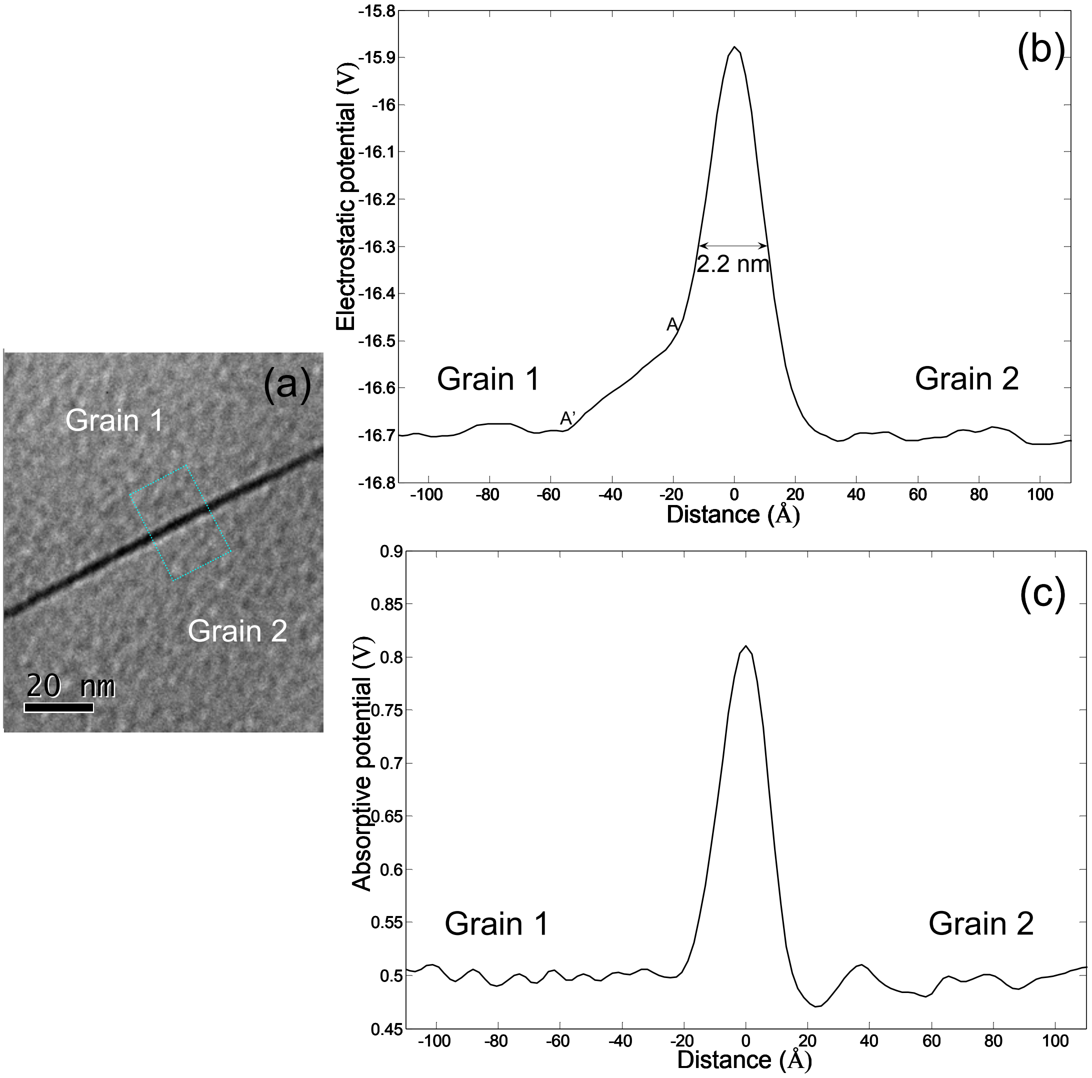

Fig. 5.5 (a) Image of an IGF in a Lu_2O_3-MgO doped Si3N4 ceramic at an overfocus of 2μm. (b) reconstructed electrostatic potential (–The potential was assumed to be constant for -137.8Å<x<-56.8Å and 32.6Å<x<133.2Å) (c) reconstructed absorptive potential.

5.5 Discussion

Comparing the absorptive potentials of the La- and Lu-containing ceramics (Figs. 5.3d and 5.5c) the Lu-containing IGF (Z_{Lu}=71) has an approximately 40% larger inelastic and high-angle scattering 'pseudo-absorptive' potential than the La-containing one. This is to be expected from the much higher nuclear charge of Lu, even if Lu- and La-concentrations within the amorphous film are almost equal [24].

Generally, one would expect the absorptive and the mean inner potential to be approximately proportional. However, since the pseudo-absorptive potential also includes the high-angle scattering, this proportionality constant depends very much on the size of the objective aperture as well as the local composition. The potential profile across the grain/glassy pocket interface is therefore needed to separate the contribution of local chemistry and space charge to the electrostatic potential profile. Under the assumption that space charge vanishes at large distance from the interface the electrostatic potential within the glassy pocket in Fig. 5.4a may be assigned entirely to the composition (SiO_2 + MgO + La_2O_3) of the amorphous material. This gives us, without the knowledge of the electrostatic / pseudo-absorptive potential proportionality constant, the information that, under the assumption of equal composition of pocket and interface, the mean inner potential of the amorphous material within the IGF and at the pocket/grain interface should be more than 1V more negative than that of the Si_3N_4 grains. The observation of a rise of the electrostatic potential at these interfaces by more than 1V may therefore only be explained by the presence of a space charge layer which is similar to the observations of Elfwing and Olsson [16] on the grain boundary of ZnO varistor material. This hypothesis is further supported by the observation of anion segregation to prism planes by HAADF-STEM [12,13,14], which is expected to attract compensating charge. This knowledge of space charge accumulation at IGFs and glassy pockets of Si_3N_4 will help to validate MD and first principle simulation methods [32] for this material.

The slanted region of electrostatic potential profile indicated by A-A’ in Fig. 5.5c may be interpreted as incomplete space charge screening within the IGF. However, further investigation of this phenomenon and additional experiments, such as spatially resolved spectroscopy are necessary for a more definite explanation to be found.

5.6 Conclusions

The projected electrostatic as well as the absorptive potential profiles across IGFs and grain/glassy pocket interface of Si_3N_4 ceramics were obtained from the reconstructed exit face wave function (using POA). Since the electrostatic as well as the absorptive potentials were scaled with respect to vacuum, an absolute scale may be assigned to them. As the estimates for the electrostatic potentials are absolute, so they represent the same results like off-axis electron holography. A new measurement of IGF width, referred as ‘potential well width’, is proposed which is basically the FWHM of the potential well. For La_2O_3-MgO doped Si_3N_4, the potential profile across the grain / glassy pocket interface was observed to be very similar to that across the IGF.

.

5.7 References

---

[1] H.-J. Kleebe, J. Ceram. Soc. Japan*,* 105 (1997) 453.

[2] H.-J. Kleebe, J. Eur. Ceram. Soc., 10 (1992) 151.

[3] X. Pan, H. Gu, S. Stemmer, M. Rühle, Mater. Sci. Forum, 207-209 (1996) 421.

[4] R. Brydson, S.-C. Chen, F.L. Riley, S.J. Milne, X. Pan, M. Rühle , J. Am. Ceram. Soc.*,* 81 [2] (1998) 369.

[5] H.G. Jeong, K. Hiraga, M.Mabuchi, K. Higashi, Philos. Mag. Lett.*,* 74 (1996) 73.

[6] A. Avishai, C. Scheu, W.D. Kaplan, Z. Metallkd.*,* 94 (2003) 272.

[7] Y.M. Chiang,L.A. Silverman, R.F. French, R.M. Cannon, J. Am. Ceram. Soc.*,* 77 [5] (1994) 1143.

[8] K. Daschowdhury, R.W. Carpenter, W.Braue, Ultramicroscopy*,* 77 (1994) 1143.

[9] D.R. Clarke, Ultramicroscopy*,* 4 (1979) 33.

[10] D.B. Williams, A.D. Romig, Ultramicroscopy*,* 30 (1989) 38.

[11] H.Gu, X. Pan, R.M. Cannon, M. Rühle, J. Am. Ceram. Soc.*,* 81 [12] (1998) 3125.

[12] N. Shibata, S.J. Pennycook, T.R. Gosnell, G.S. Painter, W.L. Shelton, P.A. Becher, Nature*,* 428 (2004) 730.

[13] A. Ziegler, J.C. Idrobo, M.K. Cinibulk, C. Kisielowski, N.D. Browning, R.O. Ritchie, Science, 306 (2004) 1768.

[14] G.B. Winkelman, C. Dwyer, T.S. Hudson, D. Nguyen-Manh, M. Döblinger, R.L. Satet, M.J. Hoffmann, D.J.H. Cockayne, Philos. Mag. Lett.*,* 84 [12] (2004) 755.

[15] A. Ziegler, C. Kisielowski, M.J. Hoffmann, R.O. Ritchie, J.Am. Ceram. Soc., 86 [10] (2003) 1777.

[16] M. Elfwing, E. Olsson, J. Appl. Phys., 92 [9] (2002) 5272.

[17] C.T. Koch, S. Bhattacharyya, M. Rühle, R.L. Satet, M. Hoffmann, Microsc. microanal.*,* (2005) in press.

[18] R.E. Dunin-Borkowski, Ultramicroscopy*,* 83 (2000) 193.

[19] D. Gabor, Rev. Mod. Phys. 28 (1956) 260.

[20] S. Bhattacharyya, C.T. Koch, M. Rühle, Ultramicroscopy*,* (2005) submitted (Chapter 4).

[21] L.J. Allen, W. McBride, N.L. O'Leary, M.P. Oxley, Ultramicroscopy, 100 (2004) 91.

[22] M.R. Teague, J. Opt. Soc. Am. 73 (1983) 1434.

[23] K. Ishizuka, B. Allman, Microscopy Today, 13 [3] (2005) 22.

[24] R.L. Satet, M.J. Hoffmann, Key Engineering Materials, 264-268 (2004) 775.

[25] W.M. Stobbs, F. M. Ross, Evaluation of Advanced Semiconductor materials by Electron Microscopy, NATO ASI series B, D. Cherns(Ed.) ,Plenum Press, London*,* 203 (1989) 183.

[26] S. Bhattacharyya, A. subramaniam, C.T. Koch, M. Rühle, Mater. Sc.& Engg. A.. (2005) accepted (Chapter 3).

[27] R.F. Egerton, Electron Energy-Loss Spectroscopy in the Electron Microscope, 2nd edition, Plenum Press, New York, (1996) p.302-305,.

[28] Y.G. Wang, V.P. Dravid, Philos. Mag. Lett., 82 [8] (2002) 425.

[29] J.C.H. Spance, Experimental High Resolution Electron Microscopy, Clarendon Press, Oxford, (1981) p. 93-119.

[30] A. Howie, Ultramicroscopy, 98 (2004) 73.

[31] G. Petzow, M. Herrmann, Silicon Nitride ceramics, Structure and Bonding, 102 (2002) 47.

[32] P. Rulis, J. Chen, L. Ouyang, W. Y. Ching, X. Su, S.H. Garofalini, Phys. Rev. B.*,* 71 (2005) 235317.

CHAPTER 6

Summary

Understanding structure and composition of interfaces is crucial for the design of ceramic materials with specific properties. In ceramics such as Si_3N_4 and SiC 1-2nm thick intergranular glassy films (IGFs) are present at the grain boundaries. Although most literature focuses on IGFs in Si_3N_4, ZnO and SiC, they have also been observed at grain boundaries in other ceramics (e.g., $SrTiO_3$, Al_2O_3), at metal-ceramic interfaces (e.g. Si_3N_4-Al, Al_2O_3-Ni), and at hetero-interfaces in composite creamics (e.g. ruthenate-silicate glass, Si_3N_4-SiC) etc. Varying the composition of IGFs has profound influence on material properties such as creep resistance, oxidation resistance, fracture toughness, electrical behaviour etc. Various transmission electron microscopic techniques have been used to study the structure and chemistry of IGFs for almost three decades. The film width has commonly been measured by different researchers using diffuse dark field imaging, Fresnel fringe imaging, high-resolution lattice fringe imaging, and most recently, by Fourier filtering high resolution electron micrographs (HREMs). Techniques based on Energy dispersive X-ray spectroscopy (EDXS) and electron energy loss spectroscopy (EELS) have been used by many researchers to study the chemistry of IGFs. Recently segregation of heavy elements at IGFs was imaged using high-angle annular dark field scanning transmission microscopy (HAADF-STEM) by some researchers. Off-axis electron holography has been used to determine the local electrostatic potential and associated space charge across an IGF while electron diffraction experiments were able to provide IGF potential profiles averaged over large distances along the boundary by different researchers.

The main aim of all studies referred to above is to characterize the structure and composition of IGFs which will provide complete control over the design of the material containing IGFs. The aim of the present PhD work is to apply a variety of conventional as well as newly developed TEM techniques to characterize these films which will help to drive the understanding of IGFs.

The theme of chapter 2 is the use of Fresnel fringes and Fourier filtering for the measurement of the thickness of IGFs. The methodologies developed in this chapter were tested on experimental images of Lu-Mg doped Si_3N_4 and $SrTiO_3$ (stoichiometric and non-stoichiometric) samples because both of these samples represent vastly different cases, when it comes to processing routes, grain-size, frequency of occurrence of IGFs, faceting of the grains and 'straightness' of the grain boundaries. The interpretability of noisy Fresnel contrast images and high-resolution images in which lattice fringes are weak or even absent on one side of the IGF can be enhanced by Fourier filtering. After Fourier transforming the images, masking either only the central spot (for normal bright field images) or all the diffraction spots along with the central spot (for high-resolution lattice fringe images) followed by inverse Fourier transformation of the unmasked region produce Fourier filtered images. Fresnel contrast hidden in high-resolution images is used to objectively demarcate the glass-crystal interface and to measure the thickness of an IGF (by Fourier filtering the lattice fringes). The optimum mask size was determined by simulations on one-dimensional projected scattering potential profiles. Image simulations using one-dimensional projected potential profiles were used to understand the different sources of left-right and underfocus-overfocus symmetry breaking, as observed in experimental images. Experimental results as well as image simulations have revealed a major problem in the standard Fresnel fringe extrapolation technique, showing that the plot of fringe spacing versus root of defocus ($(\Delta f)^{1/2}$) is not linear over the entire defocus range, as assumed by the technique, but only at intermediate defocus values. . Other limitations related to this technique are also enumerated, including the important observation that the correct thickness of the IGF is not obtained by the extrapolation method. Instead of using fringe spacings from over and underfocus images, appropriate choice of spacing values measured after Fourier filtering those images is seen to give a better symmetry in plots of Fresnel fringe spacing data. It is also seen that this technique gives a better estimate of the thickness of the IGF from the same set of images by extrapolation to zero-defocus. The approximate validity of the extrapolation method could not be understood in the framework of the simulations performed. In light of the limitations of the Fresnel extrapolation method, a new technique for the measurement of the thickness of IGFs based on Fourier filtered zero-defocus images has been proposed and tested. It has been found to be the simplest technique for the purpose of estimating the high-resolution thickness of IGFs. Simulations are used to validate the method. A comparison is made between the standard high resolution lattice fringe technique, the standard Fresnel fringe extrapolation technique and the methods of analyses introduced in the current work, to bring out their utility and merits. Taking experimental difficulties into account, this work is intended to be a practical toolkit for the study of IGFs.

Understanding the evolution of IGFs as a function of temperature has important consequences, as these films have profound influence on the properties of the ceramic, at elevated service temperatures. In-situ heating experiments are expected to provide a direct access to the behaviour of these films as a function of temperature. The limitation in the case of in-situ heating experiments using TEM, applied to the study of IGFs, is that the maximum temperature obtainable, which is around 1000ºC, is far below the sintering temperature of ceramics like Si_3N_4 (~ 1800ºC). In Chapter 3 in-situ heating experiments performed from room temperature (RT~24ºC) to 950ºC on Lu-Mg doped Si_3N_4 in 400 kV and 120 kV transmission electron microscopes (TEMs) are reported about. The choice of two different accelerating voltages is to study the effect of electron radiation (determined by the accelerating voltage of the microscope) on the evolution of IGF (if any). Lattice fringe imaging was used in the 400kV microscope to measure the thickness of the IGFs, while in the 120 kV microscope Fresnel fringes techniques were used. These techniques include: the method of extrapolation of the Fresnel fringe spacing, Fourier filtered zero-defocus images and reconstruction of the imaginary part of the potential profile from zero-defocus images. Multiple Fresnel techniques have been used for the determination of the thickness of the IGFs. This was done because of the errors inherent in the standard Fresnel extrapolation technique.

An increase in thickness at high temperature was observed in experiments performed in both microscopes. A significant difference was seen in the thicknesses measured after cooling the sample back to room temperature, compared with the initial thickness. The trends observed by the different Fresnel fringe techniques were similar. One important difference between the experiments in two different microscopes was the dwell time before the micrographs at high temperature (HT) were recorded. In the high-resolution machine, the HREM was taken 1 hr 10 min after reaching 950ºC (to allow for drift to stop), while in the 120 kV microscope the picture was taken after 15 min. Hence, it is conceivable that complete equilibrium may not have been attained at the HT in the 120 kV microscope, as reflected in the thicknesses measured by the Fresnel methods. The TEM observations of this chapter were summarized in Fig. 3.9. The Fresnel methods seem to capture the FWHM of the potential profile, while the thickness measured from HREM is representative of the core of the IGF. It can be clearly noticed that changes to the IGF thickness (in Lu-Mg doped Si_3N_4) can occur at comparatively low temperatures (<1000ºC) under low irradiation doses, with electron beam energies as low as 120 keV. Also the tendency of the IGFs to regain the width they had before annealing has been observed in the experiment in the 400 kV microscope, however, the relaxation times were not long enough to observe complete reversibility of the changes in IGF width. Due to the special geometry of the TEM sample, thermal gradients within the sample may produce a tensile-compressive straining cycle by heating and cooling which is thought to be the main reason for the changes observed in IGF thickness. Although local stress vectors, induced by thermal gradients in the sample, may offset the forces determining the IGF equilibrium width in the force balance model, dynamic observations (e.g. video recording) of the kinetics of the relaxation process may give insight into details of diffusion processes and the viscosity of the intergranular glassy phase.

In Chapter 4, an iterative method for reconstructing the exit face wave function from a through focal series of TEM image line profiles across an interface is presented. Apart from high-resolution images recorded with small changes in defocus this method works also well for a large defocus range as used for Fresnel imaging. A new experimental image alignment procedure is developed in order to align images with large relative defocus shift and its robustness in the presence of high noise and uncertainties in defocus is tested using simulated images. For the present study, it produces the best alignment in comparison with alignment procedures existing in the literature. Outline of this algorithm is presented in Fig. 4.1. Using the phase-object approximation the projected potential across the interface is determined from this exit face wave function. This is again subdivided into an electrostatic and an absorptive part, where the electrostatic potential describes the elastic interaction of the electrons with the specimen and the absorptive potential represents the loss of electrons due to inelastic scattering events involving electronic excitations in addition to the elastic (and quasi-elastic TDS) scattering outside the objective aperture. The reconstruction method is applied to both, simulated and experimental images.

For surfaces, i.e. vacuum-specimen interfaces, the electrostatic potential profile represents the absolute mean inner potential profile of the material next to the vacuum. For internal interfaces, only relative changes in potential can be measured. Mean inner potentials retrieved by this method using experimental images agree well with literature values. The resolution of the reconstruction is determined by the size of the objective aperture and is confirmed by tests on a real abrupt interface. Using experimental images from two areas with different diffracting conditions of the same interface, the reconstructed electrostatic potential is found to be insensitive to the sample orientation, although, due to the presence of an objective aperture, the absorptive potential is strongly depended on the local orientation and thus diffracting condition.

The mean inner potential profile across grain boundaries provides useful information about variations in composition and density across it, as well as about intrinsic potentials associated with depletion layers or space charge. In Chapter 5 the method described in Chapter 4 is used to retrieve potential profiles across IGFs and interfaces between grains and glassy pockets in rare earth oxide and MgO doped Si_3N_4 ceramics, a material with many industrial applications. The projected electrostatic as well as the absorptive potentials are scaled with respect to vacuum. As the estimates for the electrostatic potentials are absolute, they represent results comparable to off-axis electron holography. A new measurement of IGF width, referred as ‘potential well width’, is proposed which is basically the FWHM of the potential well. For La_2O_3-MgO doped Si_3N_4, the potential profile across the grain / glassy pocket interface is observed to be very similar to that across the IGF and also gives very strong evidence for the existence of a space charge layer at the interface. This knowledge of space charge accumulation at IGFs and glassy pockets of Si_3N_4 will help to validate MD and first principle simulation methods for this material.

CHAPTER 7

Zusammenfassung

Die Kenntnis der Struktur und Zusammensetzung von Grenzflächen ist essentiell für das Design keramischer Materialien. In Keramiken, wie zum Beispiel Si_3N_4 und SiC, treten 1-2nm dicke intergranulare Filme (IGF = intergranularer Film) an Korngrenzen auf. Zwar befasst sich der Hauptanteil der relevanten Literatur über IGFs mit Si_3N_4, ZnO und SiC, doch werden diese Filme auch in anderen Keramiken (zB. $SrTiO_3$, Al_2O_3), an Metall-Keramik Grenzflächen (zB. Si_3N_4-Al, Al_2O_3-Ni), an Heterogrenzflächen in Verbundkeramiken (zB. Ruthenat-Silikat Glass, Si_3N_4-SiC) beobachtet. Änderungen in der Zusammensetzung von IGF haben großen Einfluss auf die Materialeigenschaften, wie zum Beispiel Kriechverhalten und Oxidations-, Bruchfestigkeits- und elektrische Eigenschaften. Verschiedene Methoden der Transmissionselektronenmikroskopie wurden in den vergangenen 30 Jahren für das Studium von Struktur und Chemie von IGF eingesetzt. Von Interesse sind die Messung der Filmdicke und deren Variation über die Probe und die Beziehung der chemischen Zusammensetzung mit möglichst guter örtlicher Auflösung. Die Filmdicke lässt sich mit verschiedenen Verfahrne ermitteln: diffuser Dunkelfeldabbildung, Fresnelabbildung, hochauflösende Gitterebenenabbildung, und, seit jüngster Zeit, auch mittels Fourier-Filtern von Hochauflösungsbildern (HREM). Energie-dispersive Röntgenspektroskopie (EDXS) oder Elektronenenergieverlust-spektroskopie (EELS) kommen zur Ermittlung der Zusammensetzung zum Einsatz. Verschiedene Forschungsgruppen bildeten kürzlich die Segregation schwerer Elemente an IGF mittels Dunkelfeld-Rastertransmissionselektronenmikroskopie (HAADF-STEM) abgebildet. Andere Forscher verwendeten Elektronenholographie, um das ortsaufgelöste elektrostatische Potential und die damit verbundene Raumladungsverteilung über IGFs hinweg zu bestimmen. Auch liessen Elektronenbeugungsexperimente innerhalb der hier vorgestellten Arbeit über größere Distanzen hinweg gemittelte Potentialprofile gemessen werden.

Das Haupteinsatzgebiet der oben erwähnten Studien, die die Charakterisierung von Struktur und Zusammensetzung von IGF beinhalten, ist das kontrollierte Design von IGF-haltigen Materialien. Das Ziel dieser Dissertation ist es, eine Reihe von konventionellen und neu entwickelten TEM Methoden anzuwenden, um so die Wissensbasis über IGF zu erweitern.

Das zweite Kapitel umfasst die Anwendung der Fresnelsaummethode und des Fourierfilterns der aufgenommenen Bilder zur Messung der Dicke von IGF. Die in diesem Kapitel neu entwickelten Methoden wurden experimentell an Bildern von Lu-Mg dotiertem Si_3N_4 und $SrTiO_3$ (stoichiometrischen und nicht-stoichiometrischen) Proben gestestet, da diese beiden Beispiele im Bezug auf Verarbeitung, Korngröße, Häufigkeit der Präsenz von IGF, Facettierung der Körner und Rundung der Korngrenzen sehr verschiedene Materialgruppen repräsentieren. Die Interpretierbarkeit verrauschter Fresnelbilder und hochaufgelöster TEM Bilder, in denen Gitterebenen nur schwach oder auf einer der Seiten gar nicht zu sehen sind, kann durch Fourierfiltern erhöht werden. Die gefilterten Bilder erhält man, indem man die rohen Bilddaten erst Fourier transformiert, dann den zentralen Strahl (für Hellfeldbilder) oder alle Gitterreflexe (für Hochaufgelöste Kristallgitterabbildungen) maskiert, und schließlich wieder zurück transformiert. Die in so erhaltenen Hochaufgelösten Bildern enthaltenen Fresnelsäume werden verwendet, um die Position der Glass-Kristall Grenzfläche objektiv festzulegen und so die Dicke der IGF (durch Fourierfiltern von Gitterabbildungen) zu bestimmen. Die optimale Maskengröße wurde anhand von Simulationen von eindimensionalen Potentialprofilen bestimmt. Bildsimulationen von Potentiallinienprofilen wurden auch herangezogen, um die Ursachen für die fehlende Symmetrieachse in Fresnelsäumen und deren gebrochene Symmetrie zwischen Über- und Unterfokussierung, wie experimentell beobachtet, herauszufinden. Experimentelle Ergebnisse und Bildsimulationen haben gezeigt, dass die Relation von Saumabstand zu $\sqrt{}$Fokus ($\sqrt{\Delta f}$) nicht über den gesamten Defokusbereich linear ist, wie dies in der Standard Fresnelsaumextrapolationsmethode angenommen wird, sondern nur in einem mittleren Bereich. Weitere Limitationen der Standardmethode wurden beschrieben, zum Beispiel die wichtige Beobachtung, dass die exakte IGF Breite nicht durch die übliche Extrapolationsmethode ermittelt werden kann. Extrahiert man die Fresnelsaumabstände nicht aus den rohen Über- und Unterfokusbildern, sondern aus den Fourier-gefilterten Daten, so wird die Symmetrie im Fresnelsaumabstand-Defokus-Diagramm verbessert. Es wurde auch gezeigt, dass mittels dieser Methode die Breite von IGF durch Extrapolation nach $\Delta f=0$ aus dem selben Datensatz besser bestimmt werden kann. Die Gründe für die näherungsweise Gültigkeit der Extrapolationsmethode konnten anhand der Simulationen nicht gefunden werden. Wegen der limitierten Validität der Fresnelsaumextrapolationsmethode wurde eine neue Methode, basierend auf Fourier-gefilterten, fokussierten Bildern, vorgeschlagen und getestet. Es wurde als die einfachste Methode zur Bestimmung der Hochauflösungsbreite von IGF empfunden. Simulationen wurden herangezogen, um die Validität der Methode zu verifizieren. Ein Vergleich zwischen den Standardmethoden basierend auf Hochaufgelösten Gitterebenenabbildungen und Extrapolation von Fresnelsaumabständen und den in dieser Arbeit eingeführten Analysemethoden wurde gemacht, um deren Vorzüge und Nutzen aufzuzeigen. Unter Einbeziehung möglicher experimenteller Probleme ist diese Arbeit als praktische „Wergzeugkiste" für die Mikroskopie an IGF gedacht.

Da IGF grundlegenden Einfluss auf die Eigenschaften von Keramiken haben, ist das Verständnis der Abhängigkeit der Ausdehnung und Zusammensetzung intergranularer Filme von der Temperatur von Bedeutung. Dies trifft insbesondere bei erhöhter Temperatur, bei der diese Materialien zum Einsatz kommen, zu. Anhand von in-situ Heizexperimenten lässt sich das das Verhalten von IGF als Funktion der Temperatur direkt beobachten. In-situ Heizexperimente sind in den zur Verfügung stehenden TEM auf unter 1000ºC beschränkt, was weit unter den Sintertemperaturen von Si_3N_4 Keramiken (~ 1800ºC) liegt. Die Aussagekraft der Ergebnisse ist damit erheblich limitiert. In Kapitel 3 wird über in-situ Heizexperimente von Raumtemperatur (RT~24ºC) bis 950ºC an Lu-Mg dotiertem Si_3N_4 in einem 400 kV und einem 120 kV TEM berichtet. Die zwei verschiedenen Beschleunigungsspannungen wurden gewählt, um eventuelle, durch den Elektronenstrahl verursachte Effekte (abhängig von der

Beschleunigungsspannung des Mikroskops) auf das Hochtemperaturverhalten der IGF zu untersuchen. Im 400kV Mikroskop wurden Gitterebenenabbildung und im 120kV Mikroskop Fresnelsaum-methoden verwendet, um die Breite der IGF zu messen. Die Fresnelsaummethoden beinhalten: die Extrapolation der Saumabstände, Fourier gefilterte fokussierte Bilder und die Rekonstruktion des Absorptionspotentialprofils aus fokussierten Bildern. Verschiedene Fresnelmethoden wurden für das Bestimmen der Breite der IGF verwendet. Grund dafür sind Fehler in der herkömmlichen Fresnelsaumextrapolationsmethode.

Ein Anwachsen der IGF Breite bei hohen Temperaturen wurde währen der Experimente in beiden Mikroskopen beobachtet. Ein signifikanter Unterschied zwischen den Experimenten wurde allerdings in der gemessenen Breite nach Abkühlung auf Raumtemperatur im Vergleich zur ursprünglichen Breite beobachtet, wenn auch qualitativ das selbe Ergebnis erreicht wird. Ein wichtiger Unterschied zwischen den Experimenten in den beiden verschiedenen Mikroskopen war die Verweildauer, bevor Bilder bei der erhöhten Temperatur (HT) aufgenommen werden konnten. Im Hochauflösungsmikroskop wurden HRTEM-Bilder erst 70 Minuten nach Erreichen der Temperatur von 950ºC aufgenommen (um ein Ausklingen der thermischen Drift zu ermöglichen), während im 120kV Mikroskop die Aufnahme bereits nach 15 Minuten gemacht wurde. Daher ist es denkbar, dass das Gleichgewicht bei hoher Temperatur im 120kV Instrument noch nicht erreicht war, was sich dann in den verschiedenen gemessenen Dickemessungen mittels Fresnelsaummethoden widerspiegelte. Die TEM Ergebnisse dieses Kapitels sind in Abbildung 3.9 zusammengefasst. Die Fresnelmethoden scheinen die FWHM Breite des Potentialprofils zu messen, während die HRTEM-Bilder repräsentativ für den Kern der IGF sind, was durch frühere Arbeiten bestätigt wird. Es lässt sich klar erkennen, dass Änderungen in der IGF Breite (in Lu-Mg dotiertem Si_3N_4) bei vergleichsweise geringer Temperatur (<1000ºC) und unter geringer Elektronenstrahldosis bei Elektronenenergien von nur 120keV auftreten können. Auch die Tendenz der IGF, ihre ursprüngliche Breite von vor dem Anlassen wiederzuerlangen, wurde in dem Experiment im 400kV Mikroskop beobachtet, obwohl die Wartezeit (bei RT) nicht ausreichte, um komplette Reversibilität zu beobachten. Die Geometrie des in-situ Heizexperiments bewirkt die Existenz von Temperaturgradienten in der Probe, derentwegen das Erhitzen und Abkühlen einem Zyklus von Zug- und Druckspannung entspricht, was als Hauptgrund für die zu beobachtenden Veränderungen in der Breite der IGF denkbar ist. Obwohl örtliche Spannungen, die durch Temperaturgradienten verursacht werden, in die Summe der Kräfte, die die Gleichgewichtsbreite der IGF beeinflussen, mit einbezogen werden müssen, könnten zeitaufgelöste Experimente (zB. Videoaufnahmen) Einblick in die Details von Diffusionsprozess und Viskosität in der intergranularen amorphen Phase geben.

In Kapitel 4 wird ein iterativer Algorithmus zur Rekonstruktion der Austrittswellenfunktion aus einer Fokusserie von TEM Bild Linienprofilen über eine Grenzfläche hinweg vorgestellt. Die Anwendbarkeit dieses Algorithmus erstreckt sich, nicht nur auf HRTEM Bilder, die mit vergleichsweise kleinen Fokusänderungen aufgenommen werden, sondern auch auf den Bereich großer Fokusänderungen, wie sie in der Fresnelabbildung zum Einsatz kommen. Eine neu entwickelte Bildjustierprozedur erlaubte aus den aufgenommenen Bildern, trotz der großen Fokusänderungen, miteinander korrespondierende Bildausschnitte exakt auszuwählen. Die Robustheit dieser Methode gegen Rauschen und Defokusunsicherheit wurde anhand von simulierten Daten gestestet. In der vorliegenden Arbeit konnte mit dieser Methode die beste Bildjustage im Vergleich zu den bereits existierenden Methoden aus der Literatur erreicht werden. Abbildung 4.1 gibt einen Überblick über den Algorithmus. Unter Verwendung der Phasenobjektnäherung wurde das projizierte Potential über die Grenzfläche hinweg aus der rekonstruierten Austrittswellenfunktion bestimmt. Dieses wurde wiederum in elektrostatische und absorbierende Komponente unterteilt, wobei die elektrostatische Komponente die elastische Beugung der Elektronen in der Probe beschreibt und die absorbierende Komponente den Verlust von Elektronen durch inelastische Streuvorgänge, die die Anregung elektronischer Zustände in der Probe bewirken, und Beugung zu hohen Winkeln außerhalb der Objektivblende (inklusive thermisch diffuser Streuung) beinhaltet. Diese Rekonstruktionsmethode wurde an simulierten und experimentellen Daten angewendet.

Für Oberflächen, zum Beispiel die Vakuum-Präparat Grenzfläche, repräsentiert das elektrostatische Potential das mittlere innere Potential des Materials. Für innere Grenzflächen können nur relative Änderungen im Potential gemessen werden. Mit der hier vorgestellten Methode liessen sich Werte für das mittlere innere Potential ermitteln, die gut mit Literaturwerten übereinstimmen. Die Auflösung dieser Rekonstruktionsmethode ist durch die Größe der Objektivblende bestimmt und wurde durch Tests an einer scharfen Grenzfläche getestet. Die Rekonstruktion von Fokusserien verschiedener Stellen entlang einer Grenzfläche hat gezeigt, daß das rekonstruierte elektrostatische Potential unabhängig von der örtlichen Probenorientierung gemessen werden kann, während die absorbierende Komponente wegen der Verwendung einer Objektivblende sehr stark von der lokalen Orientierung abhängt.

Profile des mittleren inneren Potentials über Grenzflächen hinweg liefern nützliche Informationen über Variationen der chemischen Zusammensetzung, der Dichte aber auch der Raumladungswolken. In Kapitel 5 wurde die in Kapitel 4 beschriebene Methode auf die Rekonstruktion von IGF Potentialprofilen und Grenzflächen zwischen Körnern und amorphen Taschen in Si_3N_4 Keramiken angewandt, die mit Seltenen Erden und MgO dotiert waren, einem Material mit vielfältigen industriellen Anwendungen. Die elektrostatische und absorbierende Komponente des projizierten Potentials wurden relativ zum Vakuum skaliert. Diese absolute Skalierung macht die Ergebnisse vergleichbar zur off-axis Elektronenholographie. Ein neues Maß der IGF Breite, die „potential well width“, wurde eingeführt und entspricht der FWHM des Potentialtopfes. Für La_2O_3-MgO dotiertes Si_3N_4 wurden Potentialprofile über die Grenzfläche zwischen Korn und amorpher Taschen untersucht. Diese sind Potentialprofilen über IGF sehr ähnlich und geben auch Hinweise auf die Existenz einer Raumladungsschicht an der Grenzfläche. Die Kenntnis der Existenz von Raumladungsschichten an IGF und Grenzflächen zwischen Glass und kristallinen Körnern ist erforderlich, um exakte MD und „first-principles Calculations“ für diese Materialklasse durchzuführen.

Curriculum Vitae

Name	Somnath Bhattacharyya
Date of birth	August 2, 1976
Place of birth	Serampore, India
Nationality	Indian
Marital Status	Married

Education

1996-2000	**Bachelor of Engineering (B.E)** Department of Metallurgical Engineering, Visvesvaraya Regional College of Engineering, Nagpur Nagpur university, India.
2001-2003	**Master of Engineering (M.E)** Department of Metallurgy Indian Institute of Science , Bangalore, India
since March, 2003	**PhD** student Max-Planck-Institut für Metallforschung, Stuttgart and Universität Stuttgart, Germany under supervision of Prof. Dr. Dr. h.c. M. Rühle

Publications:

1. "The evolution of amorphous grain boundaries during In-situ heating experiments in Lu doped Si_3N_4"
   S. Bhattacharyya, Anandh Subramaniam, C.T. Koch R. M. Cannon and M. Rühle
   *Materials Science and Engineering A, **accepted**.*

2. "Aspects regarding measurement of thickness of Intergranular Glassy Films"
   S. Bhattacharyya, Anandh Subramaniam, C.T. Koch and M. Rühle
   *Journal of Microscopy, **accepted**.*

3. "Measuring electrostatic potential profiles across amorphous intergranulaur films by electron diffraction"
   C.T. Koch, S. Bhattacharyya, M. Rühle, R.L.Satet and M.J. Hoffmann
   *Microscopy and Microanalysis, **in press**.*

4. "Projected potential profiles across interfaces obtained by reconstructing the exit face wave function from through focal series"
   S. Bhattacharyya, C.T. Koch and M. Rühle
   *Ultramicroscopy, **submitted**.*

5. "Projected potential profiles across the intergranulaur glassy films "
   S. Bhattacharyya, C.T. Koch and M. Rühle
   J. Am. Ceram. Soc., ***submitted***.

6. "Assessing thermodynamic properties of amorphous nanostructures by energy filtered electron diffraction"
   C.T. Koch, S. Bhattacharyya, Anandh Subramaniam, and M. Rühle,
   *Microscopy and Microanalysis, **10, Suppl. 2, p.254, 2004.***

7. "Liquid Holdup in Non-wetting Packing with Lateral Gas Injection"
   G.S. Gupta and S. Bhattacharyya
   *ISIJ International, **Vol. 43, p1927, 2003.***

Acknowledgements

I feel great pleasure to express my heartfelt gratitude and respect to Prof. Dr. Dr. h.c. M. Rühle for giving me the opportunity to work as a Ph.D. student in his department. I have immensely benefited from his stimulating discussions, valuable inputs and continuous encouragement. His enthusiasm and integral view on research has made a deep impression on me.

I would also like to thank Prof. Dr. F. Aldinger and Prof. Dr. Ir. E.J. Mittemeijer for accepting my request of being examiners for this work.

I am greatly indebted to Dr. Christoph T. Koch for being such a wonderful advisor and friend. Working with him was a great learning experience – both academically and personally. This thesis would not have been what it is now but for his invaluable guidance, support, discussions and critical evaluation at each and every stage of my progress. I express my deep sense of gratitude to him for taking the pain to write the German version of the summary at a very short notice.

I am thankful to Dr. Anandh Subramaniam for his supports in many aspects of research, fruitful discussions and continuous encouragement. I would like to thank Dr. R. M. Cannon of LBL, Berkley and Dr. Wilfred Sigle for helpful discussions. I would also like to thank Dr. Gunther Richter and Ms. Limei Cha for providing the TEM sample containing the Al-Al2O3 interface and useful information about it.

Heartfelt thanks are expressed for Kersten Hahn, Peter Kopold, Marion Kelsch, Ute Salzberger, Mariya Sycha and Ute Bäder for their consistent support.

I thank all the colleagues in the ‘Department Rühle’ and in the Institute for providing pleasant working atmosphere and the help rendered by them in various stages of this work. I also take this opportunity to thank all of my friends who made my stay at Stuttgart pleasant and enjoyable.

As much as my studies, if no more, has my life been blessed by my beloved parents, my wife, my sister and my best friend Hiru. I want to specially thank my mother and my wife for their moral support during hard days.